MULTI-SCALE EXAMINATION OF PANCREATIC CANCER CELL BIOPHYSICS

by
Daniel J. Shea

A dissertation submitted to Johns Hopkins University in conformity with the requirements for the degree of Doctor of Philosophy

Baltimore, Maryland
March 2017

ABSTRACT

Pancreatic cancer resulted in nearly 42,000 deaths in 2016 making it the third leading cause of cancer-related death in the United States (1). The high mortality rate stems from that fact that treatment options are limited as less than 20% of patients are candidates for surgical tumor removal because pancreatic cancer is usually detected after it has metastasized to other organs. Cancer metastasis is a multistep process where tumor cells migrate from a primary tumor into the vasculature, where the circulating tumor cell can then roll on and bind to the vascular epithelial wall before extravasating to a secondary location. If this cascade is interrupted at any point, metastasis is abrogated. Therefore given its severity, understanding and treating pancreatic cancer metastasis is critically important in reducing the high mortality rate associated with the disease.

In this dissertation, the metastatic cascade is first discussed in detail to outline the various areas where treatments can be implemented to disrupt the process and halt metastasis. Next, the biophysics of selectin-mediated cell adhesion is addressed before exploring the relevant function of selectin ligands present on pancreatic cancer cells, mainly PODXL, MUC16 and CD44. Finally giant obscurins, giant tumor suppressing proteins which play a role in cancer migration, and monobodies, an antibody alternative which can be engineered to treat metastatic cancer, are discussed (Chapter 1).

Having established a background in several key players involved in pancreatic cancer metastasis we explore the critical parameters of selectin-mediated pancreatic tumor cell tethering and rolling. First the equations and models vital to understanding selectin-mediated binding and tethering are overviewed (Chapter 2). Next using force

spectroscopy, we characterized the binding interactions of MUC16 and PODXL to E- and L-selectin at the single-molecule level. To further analyze the response of these molecular interactions under physiologically relevant regimes, we used a microfluidic assay in conjunction with a mathematical model to study the biophysics of selectin-ligand binding as a function of fluid shear stress. We demonstrate that both MUC16 and PODXL-E-selectin-mediated interactions are mechanically stronger than like L-selectin interactions at the single-molecule level, and that these interactions display a higher binding frequency at all contact times. Finally we determined that several key kinetic parameters regulate the average velocity of ligand-coated microspheres rolling on selectin-coated surfaces in shear flow (Chapter 3).

We then sought to evaluate the critical parameters of the pancreatic tumor adhesion to hyaluronic acid (HA) mediated by rolling on E-selectin in physiologically relevant flow. We show that tumor cells rolling on E-selectin were significantly more likely to bind to HA than non-rolling cells at both low and high shear stresses. Further, the ligand-E-selectin interaction initiates adhesion to HA in a twofold manner, both physically slowing cells and allowing cells to orient close to the surface and increasing the on rate of adhesion. Understanding the biophysics of selectin-ligand bonds and their responses to physiologically relevant shear stresses is vital for developing diagnostic assays and/or preventing the metastatic spread of tumor cells by interfering with selectin-mediated adhesion (Chapter 4).

We next looked to characterize the presence and absence of giant obscurins in pancreatic cells and assess their effect on cell migration and cytoskeletal dynamics. Here we establish that giant obscurin are depleted in PDAC tissue and metastatic pancreatic cancer cell lines, but are expressed at high levels in normal pancreatic tissue and non-tumorigenic human pancreatic ductal epithelial cells (HPDE). Stable clones of HPDE cells lacking giant obscurins have decreased RhoA activity and increased PI3K/AKT activity which in turn leads to major cytoskeletal alterations including increased actin dynamics at cell-cell junctions, faster microtubule growth and decreased focal adhesion density. Additionally, the loss of obscurin in HPDE cells leads to faster and more dynamic cell migration and treating these cells with a PI3K inhibitor decreases migration speeds in both confined and unconfined microchannels. This work is important because identifying biomarkers that increase cell migration and cytoskeletal dynamics such as giant obscurins is critically important to the prevention and treatment of pancreatic cancer metastasis (Chapter 5).

Next we explore the binding mechanics of the monobody YS1, an antibody alternative derived from the fibronectin scaffold. Using alanine-scanning mutagenesis simulations, we identified two residues (R33 and E47) in the conserved monobody scaffold that are critical to the binding interaction between the monobody YS1 and its ligand, maltose-binding protein (MBP). Using steered molecular dynamics simulations we predicted that mutations to these residues in the YS1 scaffold would substantially destabilize the YS1-MBP interface and that the R33A mutation has a greater destabilization effect, weakening hydrogen binding between all scaffold residues and MBP and not just between R33 and MBP. We validated the simulation using two biophysical tools, single-molecule force spectroscopy and surface plasmon resonance. This integrated approach to monobody scaffold evaluation improves our understanding of

the monobody interactions with a target, providing guidance for the improved engineering of monobodies (Chapter 6).

Finally we conclude by summarizing the results of this work and discussing future work including planned in vivo experiments, which will assess pancreatic cell tumorigenicity and metastasis in multiple mouse models (Chapter 7). In summary, this dissertation reviews and utilizes current biophysical measurements to evaluate multiple pancreatic cancer cell biomarkers that affect various stages along the metastatic cascade and highlights improvements in potential treatments.

Advisor:

Dr. Konstantinos Konstantopoulos

Thesis committee:

Dr. Sharon Gerecht

Dr. Honggang Cui

Dr. Stuart Martin

Dr. Michael Goggins

ACKNOWLEDGMENTS

I have many people to thank, who worked with me throughout this dissertation, all of whom have impacted me positively and helped me tremendously. First I would like to thank my advisor, Dr. Konstantinos Konstantopoulos. It has been a pleasure to work in your laboratory, and it is a direct result of your leadership, determination and expertise that has gotten me to this point in my career. You have established a collaborative and fast paced lab, which helped me thrive, and I am very appreciative for that.

Next I would like to thank my collaborators including Dr. Lei Zheng and the late Dr. Huso at the Johns Hopkins School of Medicine and Dr. Denis Wirtz at Johns Hopkins. Your dedication and exuberance for this work was vital to its success. Also Dr. Aikaterini Kontrogianni-Konstantopoulos at the University of Maryland School of Medicine, your passion for obscurins and your willingness to talk and collaborate is very much appreciated. I would also like to thank my committee members including professors Konstantinos Konstantopoulos, Sharon Gerecht, Honggang Cui, Michael Goggins and Stuart Martin as well as the alternates, professors Zachary Gagnon and Aikaterini Kontrogianni-Konstantopoulos.

Thank you to all the members of the Konstantopoulos lab: Alexandros Afthinos, Kaustav Bera, Dr. Jack Chen, Dr. Luthur Cheung, Dr. Matthew Dallas, Dr. Bryan Grabias, Dr. Zhizhan Gu, Dr. Wei-Chien Hung, Robert Law, Dr. Panagiotis Mistriotis, Elizabeth Orth, Dr. Colin Paul, Dr. Phrabha Raman, Dr. Kimberly Stroka, Soontorn Tuntithavornway, Emily Wiseniewski, Bin Sheng Wong, Chris Yankaskas, Yuqi Zhang and Runchen Zhao.

Among my colleagues, I would like to extend my gratitude specifically to Colin Paul, who I worked with on the contact guidance project. Colin has taught me so much about proper experimental design and statistical analysis and his level of dedication and meticulousness is something I can only hope to achieve. Special thanks to Luthur Cheung, who taught me everything I know about cell rolling in the minimal time that he was here and who was a coauthor of the monobody paper with me. I would also like to thank Bin Sheng Wong, your dedication and high spirits really helped me push through these projects and your hard work has served as an inspiration to me. I also had the pleasure of working with and learning from Wei-Chien Hung, Jack Chen, and Kimberly Stroka who showed me how perseverance can lead to great achievements. Finally I would like to thank Alexandros Afthinos and Chris Yankaskas who were always willing to help and offer advice.

Next I would like to thank my friends in other labs here at Hopkins, including Quinton Smith. He was always there when I needed someone to complain to or hang out with, for both the positive and stressful times, his enthusiasm for research is contagious and I am a better man for having known him. Jake Sarnecki, for providing some much needed balance in my life and always being there with the answer to my questions. To the many members of out intramural sports teams including but not limited to Brad Rupp, Michael Blatchley, Tiana Warren, Tina Xiong and Jude Phillip. We won five championships in five different sports, so I guess we were pretty good.

Finally I would like to thank my family and friends, especially my parents, James and Loraine Shea. From a young age you have instilled in me the desire to strive to be the best. It is from you that I got my grittiness and perseverance and your love and support throughout this process means the world to me. To Erin Thompson, your support have made this process easier, and thank you for always letting me go to lab on the weekends. I cannot thank you all enough.

DEDICATION

To my friends and family,

who pretended to understand what I was doing.

TABLE OF CONTENTS

LIST OF TABLES

LIST OF FIGURES

Chapter 1

INTRODUCTION

Despite the effort put into the research and treatment of cancer, it remains the second leading cause of death worldwide, behind heart disease. In 2016, it was estimated that almost 1.7 million new cases of cancer will be reported and nearly 700,000 cancer related deaths will occur in the United States alone (1). Interestingly, the overall incidence of death from cancer has decreased from 2003-2013; however, this is likely attributed to decreases in the rates of specific cancers, rather than broad improvements in treatment. Lung cancer and colorectal cancer deaths have decreased substantially since the 1990's as smoking numbers declined and prevalence of colonoscopies increased (2, 3). Despite the falling rates of several cancers and the numerous treatments options, which are developed every year, the rates of certain cancers including pancreatic, liver, and uterine corpus cancers have continued to increase (1).

While cancer death rates have decreased 21% since 1991, cancer deaths continue to rise for two of the most deadly forms of cancer: liver and pancreatic. Specifically pancreatic cancer resulted in nearly 42,000 deaths in 2016 making it the third leading cause of cancer related death in the United States (1). Pancreatic cancer incidences and death rates have increased 1.2% and .4% respectively since 2000 (1). Currently no reliable methods exist for the early detection of pancreatic cancer. This coupled with the fact that the symptoms of pancreatic cancer usually go unnoticed until the disease has progressed has led to the poor prognosis usually associated with pancreatic cancer. As a result the average 1-year and 5-year survival rates are only 29% and 7% respectively (4). This largely stems from that fact that treatment options are limited. In fact less than 20% of patients are candidates for surgical tumor removal because the cancer is usually detected after it has metastasized to other organs. The average life expectancy after diagnosis with the metastatic disease is only 3-6 months (4). Therefore, understanding and treating pancreatic cancer metastasis is critically important in reducing the high mortality rate associated with the disease.

Cancer metastasis is a highly coordinated process by which tumor cells spread from a primary tumor to a secondary distal tissue, and metastasis is responsible for about 90% of deaths from solid tumors (5). The metastatic cascade is a complex multistep process, in which cancer cells migrate from the primary tumor to the circulatory system where they extensively interact with the endothelial wall before eventually extravasating and colonizing a distal organ, forming a secondary tumor. Throughout this process, cell migration and the protein-protein interactions mediated by adhesive proteins known as selectins are critically important. This work will focus on treating several steps of the metastatic cascade including pancreatic tumor cell rolling and attachment to ligands found on the vessel walls as well as the identification of a pancreatic tumor suppressor, which alters the mechanics of pancreatic cell migration.

1.1 The metastatic cascade

Although metastasis is the major cause of death from cancer, despite studying the process for over 200 years, cancer metastasis remains controversial (6). In 1889 the “seed and soil” model of cancer metastasis was suggested by Stephen Paget. It suggests that cancer metastasis relies on both the cancer cell and the nature of the distal tissue environment much like “When a plant goes to seed, its seeds are carried in all directions, but they can only live and grow if they fall on congenial soil” (7). This theory has been developed more recently as studies have shown that although tumor cells pass through the vasculature of many organs, metastatic tumor cells can only develop in favorable or congenial organs (8). Currently this hypothesis is generally accepted although it has been expanded upon, where the “seed” refers to not only the metastatic cell but also a cancer stem cell or initiating cell and the “soil” refers to the stroma or organ microenvironment (9).

Once a primary tumor has formed, it is the combination several factors including continued tumor proliferation, vascularization, accumulated genetic changes and the activation of intricate signaling pathways which can prompt cells to enter the metastatic cascade. Throughout each step of the cascade, tumor cells must migrate, attach to, and navigate considerably different microenvironments including tissue at the primary and distal sites as well as blood vessel endothelium (6). To successfully form a secondary tumor, cells acquire the necessary genetic modifications to allow for the navigation of each of these diverse and sequential steps, each of which can be rate limiting as a failure at any step would stop the metastatic process (10).

1.1.1 Primary tumor formation

Tumors result from the abnormal proliferation of cells, where normally healthy cells gradually become malignant through a progressive sequence of genetic mutations.

These genetic alterations select for cells with an increased propensity for survival, proliferation, and migration. The act of tumor initiation, progression and eventual metastasis is not fast. The growth rates of tumors are generally slow with doubling times on average of 160 days but varying from 44 days to over 1,800 days (11, 12). As a result tumors growing to 1 cm, take an average of 12 years to form.

Although metastasis can occur when the tumor is small most metastases are thought to occur when the tumor is large at the later stages of tumor development (10). However, all cells in a malignant tumor are not equally metastatic due to genetic alterations, which can activate the metastatic genetic program in these progenitor cells (13). Metastatic clones result from divergent gene expression from the primary tumor, and as a result the tumor itself is a heterogeneous environment consisting of both metastatic and non-metastatic tumor cells (14, 15).

1.1.2 Tumor vascularization

Because of the extensive metabolic demand and growth of tumor cells, they require access to oxygen and nutrients. Therefore, vascularization of the tumor is necessary for tumors to exceed 1-2 mm in diameter (16). Cancer cell secretion of angiogenesis factors is a critical step in establishing the vascular system necessary for tumor survival (16). Interestingly, many tumor types including pancreatic neuroendocrine carcinoma are extremely angiogenic an as a result are highly vascularized (17).

1.1.3 Mechanisms of cell invasion

Following vascularized tumor formation the ability of cells to invade the surrounding tissue is critically important to initiating the metastatic process. Cancer cells can invade the surrounding stroma and adjacent tissue by migrating either as detached single cells or collectively as cell sheets or clusters (18). In the tumor, neighboring cells are connected through cell-cell contacts, which are stabilized through the E-cadherin connections by adjacent cells. Intracellularly, E-cadherin links adherence junctions to the actin cytoskeleton through interactions with b-catenin, a-catenin and p120 catenin (19).

During the progression of cancer, genetic mutations affect cell plasticity and result in distinct phenotypical changes including the collective to amoeboid transition (CAT), the epithelial to mesenchymal transition (EMT), and the mesenchymal to amoeboid transition (MAT) (20, 21). EMT is a primary indication of cancer progression to an aggressive form and is present in pancreatic cancer progression (22). EMT is defined loss of epithelial characteristics and the gain of mesenchymal gene expression. Specifically, cells undergoing EMT develop the loss of E-cadherin, the subsequent disruption of adherence junctions, and increased production of mesenchymal markers such as vimentin and of N-cadherin. The switch from E- to N-cadherin enhances cell motility allowing cells to migrate away from the primary tumor in a mesenchymal fashion. Additionally, the migration of cells away from a primary tumor requires the remodeling of the extracellular matrix (ECM). Cells degrade the matrix to form migrational tracks through the excretion of matrix metalloproteinases, which are unregulated for nearly every type of cancer (23).

1.1.4 Circulating tumor cells

Tumor cells, migrating away from the primary tumor, must navigate to and through the vascular endothelium in a process known as intravesation. This critical step is necessary to gain access to the circulatory system. Once in the circulatory system, cancer cells are now referred to as circulating tumor cells (CTCs). Here they face a series of hydrodynamic forces, interactions with immune cells, and collisions with both blood cells the endothelial cells of the vessel wall (5). Since only the CTCs that can overcome these pressures can seed tumors at a distal location, only a small fraction of CTCs survive and successfully generate metastasis. In fact, using mouse tail-vein injections as a model, this number is estimated at only 0.01% (24).

Once in the circulatory system, the path that a CTC travels is influenced by a number of parameters including the blood flow patterns, the size of the vessels and the interplay between disruptive shear forces and cell-cell adhesion, which leads to the arrest of cells in the blood vessels. As cells circulate they experience shear stress, which results from the differing velocities of the fluid (blood) throughout the cross-section of the vessel. In a cylindrical vessel, the blood velocity is the highest at the center and zero at the vessel walls. This change in fluid velocity leads to the shear force felt by CTCs, which is a force per unit area and commonly has units of Newtons per square meter (N/m^2) or dynes per square centimeter (dyn/cm^2). The average shear stress levels vary between 1-4 dyn/cm^2 in the venous system to 4-30 dyn/cm^2 in arterial circulation (25).

1.1.5 Adhesion to the vessel wall and extravasation

In order for a tumor cell to extravasate from the vasculature to a secondary location, the cell must first adhere to the vessel wall. This process can occur through physical occlusion or through cell-cell adhesion. Physical occlusion occurs if a cell enters a vessel that has a diameter less than the radius of the cell. Since CTC diameters are generally larger than 10 um, occlusion occurs primarily in small blood vessels or in capillaries (5). Adhesion occurs in larger blood vessels and is dependent on specific interactions between CTC ligands and receptors on the endothelial wall.

Circulating tumor cells in the vasculature interact with selectins on the endothelial wall and it is these selectin-ligand interactions that mediate cell rolling and lead to firm adhesion. The probability of cellular arrest in the vasculature relies on the frequency of contact between membrane bound ligands expressed by CTCs and receptors expressed on endothelial cells, as well as the time or extent of these interactions. The interacting time (residence time) is dependent on the interplay between the adhesive forces of the receptor-ligand bonds formed between the endothelial wall and the CTC and the shear forces exerted on the CTC as it flows through the vasculature. At higher shear stresses, cells are expected to increase their contact frequency with the endothelial wall but decrease their adhesion time as CTCs spend less time in contact with the vascular wall (5).

Interestingly the probability of cellular arrest is expected to be highest at intermediate shear stress levels. This is a direct function of the kinetic (k_{off} and k_{on}) and micromechanical properties (reactive compliance and tensile strength) of the single ligand-receptor bond, which will be expanded on in Chapter 2. The strength of these bonds and their ability to quickly form will dictate both the cell's ability to bind to the endothelium at a designated shear stress and the type of binding interaction (i.e. cell tethering, transient rolling, stable rolling, firm adhesion). Several key characteristics are required for the formation of ligand-receptor bonds necessary to mediate cell binding in shear flow. These bonds require a relatively fast on-rate (k_{on}), which allows for bonds to form at short interaction times. Next, they must have a high tensile strength to overcome hydrodynamic forces, which will disrupt bond formation and retention. Finally ligand-receptor bonds must have slow off-rates, (k_{off}) which allow for a prolonged bond lifetime and ensure the formation of new bonds.

Selectin-ligand bonds, which will be discussed in detail in Chapter 1.2 have high on-rates, high tensile strengths and fast off-rates and therefore can facilitate transient, faster rolling interactions and in some instances slower cell rolling. Integrin-ligand and HA-ligand interactions have slower on-rates and low off-rates. These interactions occur only after selectin-mediated rolling has occurred or at low shear stresses and result in stable or firm adhesion due to the low off-rate of these interactions. Following tumor cells arrest in the vasculature, cells will release soluble factors and then can extravasate or migrate from the vasculature to a secondary location.

1.1.6 Formation of secondary tumor

If the tumor cell has navigated this cascade and successfully migrated to a distal location, the secondary tumor can then grow if the microenvironment is suitable for growth. However, because the new environment may be unsuitable for growth, tumors cells will often rest in a dormant state until they can adapt and grow (26). Once the metastases begin growing the process starts again, with the requirement for tumor vascularization and the ability to form new metastases.

If the metastatic cascade is disrupted at any point tumor cells cannot seed new tumors at a secondary location. For instance, by disrupting a cancer cell's ability to migrate, the cascade is broken at either the invasion/intravastation/extravasation step in the cascade, while blocking a cell's ability to adhere to the vessel wall will again disrupt this process. This work will herein focus on these two facets of the metastatic cascade, [1] exploring how pancreatic cancer cells bind and firmly adhere to the vascular endothelium in shear flow and [2] how tumor suppressors, which when lost from pancreatic epithelial cells increase cell migration and tumorigenicity.

1.2 Biophysics of selectin-mediated adhesion

Cell adhesion is vital to several biological processes ranging from inflammation to cancer metastasis. As discussed in Chapter 1.1.5 cell adhesion as it pertains to metastasis relies on the formation of bonds primarily between tumor cell surface ligands and selectins or integrins expressed by endothelial cells. E-, P-, and L-selectins are a family of three physically similar adhesion proteins. At the animo end, all three selectins have a lectin domain with a similar sequence to c-type lectins, a calcium dependent animal. This domain is followed by an epidermal growth factor like domain, a variable number of short consensus repeats, the transmembrane domain and finally the short carboxyl terminal tail (27). While E-, P-, and L-selectins share a similar structure, the binding kinetics and distribution differ considerably leading to their distinct roles in cancer metastasis.

E-selectin (CD62E) is expressed on activated vascular endothelial cells. It must be activated at the transcription level and protein levels peak after 4-6 hours once exposed to an inflammatory stimuli (27). P-selectin (CD62P) is expressed on platelets and can also be induced on vascular endothelium through exposure to the cytokines interlukin-4 or oncostatin M (28). L-selectin (CD62L) is constitutively expressed on the surface of leukocytes.

At the lectin domain, selectins bind to glycosylated ligands in the presence of calcium. Binding occurs on a shallow region that overlaps a calcium coordination site opposite of the EGF domain (29). While the lectin domains are conserved in all three selectins, the length of the repeated consensus sequence regions result in differing binding mechanics. All three selectins recognize sialofucosylated oligosaccharides such as sialyl-Lewis x (sLe^{x}) and its isomer sialyl-Lewis a (sLe^{a}) which are the terminal components of glycoproteins and glycolipids expressed on interacting cells (30-33). Notably, sLe^{x} is absent from normal tissue in the pancreas (34, 35), but present in pancreatic ductal adenocarcinoma and high-grade pancreatic intraepithelial neoplasia lesions (34). However, the binding affinity of selectins for monocovalent sLe$^{x/a}$ is low, and therefore it is vital to distinguish between structures that only interact with selectins *in vitro* and the *functional* selectin ligands (36) that interact with selectins selectively and with high affinity *in vivo* and whose depletion suppresses selectin-dependent binding.

1.2.1 2D receptor-ligand kinetic – the micropipette assay

Numerous techniques exist to study receptor-ligand binding mechanics. These techniques, like surface plasmon resonance rely on one protein (either the receptor or ligand) to be in solution. This limits their measurement to 3D binding constants; however, the receptor-ligand binding relevant to cancer metastasis occurs in 2D, leading to differing binding mechanisms and kinetics (37). Recently assays were developed to measure 2D binding mechanics in the absence and presence of shear flow.

The micropipette aspiration technique uses a receptor coated red blood cell (RBC), which is brought into contact with a ligand coated bead or a polymorphonuclear leukocyte. The RBC and bead/leukocyte are stabilized via a micropipette and piezo-displacement respectively (38). They are then brought in contact for prescribed periods of time and the micropipette is retracted at a set velocity. The rector-ligand interaction is monitored using video-microscopy and the rupture force is calculated by multiplying the stiffness of the RBC membrane with the extension of the RBC at the moment of bond rupture (38). This technique can be used to determine 2D dissociation constants as well as the 2D binding affinity per contact area ($A_cK_a^o$) (39).

1.2.2 Single molecule force spectroscopy

In addition to the micropipette aspiration technique two ultrasensitive probes are used in force spectroscopy studies to measure binding interactions: BPF and MFP. In BPF the force is measured by the displacement of a glass microsphere, which has been immobilized on a RBC. In MFP the force is measure by the deflection of a cantilever. While both of these techniques measure forces in a physiologically relevant range from 5 pN to 1 nN (27) the remainder of this section will focus on MFP as it is directly relevant to the present work.

MFP utilized atomic force microscopy (AFM) where a flexible receptor-coated cantilever can deflect in response to forces generated when it is brought in contact with a ligand-coated surface. The cantilever deflection is measured via a laser and can be transformed into forces by multiplying the deflection by the spring constant of the cantilever. MFP experiment can be preformed using a functionalized cantilever contacting a ligand coated glass substrate, a functionalized cantilever contacting a cell immobilized on a glass surface or a cantilever with an immobilized cell contacting a cell on a glass surface (40, 41). Using intact cells has two benefits as it ensures that the membrane receptors and ligand are in their physiological orientation and that they are intact with the cytoskeleton. However, with this method, cell deformability and interactions with non-specific targets can complicate the results. Recently ligands supported in lipid bilayers (ligand-receptor system) have produced similar kinetic constants to the cell-receptor system (40, 42).

By plotting the distance traveled by cantilever against the force both the loading rate and rupture force of the receptor-ligand bond can be determined (41, 42). Furthermore, by plotting the natural log of the loading rate against the rupture force the Bell model kinetic parameters, unstressed dissociation constant (k_{off}) and the reactive compliance of the bond (x_β) can be determined. These parameters rely on the contact duration of the binding interaction and the retraction velocity of the cantilever (42). Details on this calculation are explored in Chapter 2.1. Further, for these measurements to be accurate it is vital that only one bond form per retraction. To ensure this receptor and/or ligand densities are selected to allow for 10-35% bond formation. In this binding range, greater that 80% on the interactions will involve a single bond based on Poisson statistics (27). Other controls involve treating the sample with the calcium chelator EDTA or a functional anti-selectin antibody to abrogate binding and ensure the accuracy of the measurements.

1.2.3 Slip bonds and catch bonds

Numerous receptor-ligand pairs have been studied using either BPF or MFP. These binding interactions include integrin-VCAM-1, cadherin-cadherin, and ligand-E-/L-/P-selectin binding. The rupture of these bonds can exhibit two behaviors, which are identified as catch and slip bonds. Catch bond lifetimes increase with the application of an external force while the lifetime of a slip bond decreases with the application of an external force (43). Catch bonds are often pictured as the common child’s toy, the finger trap, where pulling your fingers apart (applying force) decreases the chance that the trap will successfully be removed.

The kinetic and micromechanical properties of selectin-meditated interactions were originally estimated by monitoring leukocyte interactions with selectins in shear flow however, this methodology could not exclude the formation of multiple bonds and relies on assumptions to determine the force applied to the bond (44). Utilizing BPF or MFP has been adopted to accurately measure the properties of the slip bond at the single molecule level. Using single molecule force spectroscopy the rupture of E-, P- and L-selectin to P-selectin glycoprotein-1 (PSGL-1), the primary selectin ligand presented on neutrophils was studied over a physiologically relevant level of loading rates (41, 45).

The PSGL-1-L-selectin bond was found to have a higher k_{off}, a higher x_β and a lower tensile strength than either the PSGL-1 bond with E- or P-selectin, thus indicating a weaker bond strength (with E-/L-selectin) and explaining the faster rolling of neutrophils on L-selectin (41, 46). The PSGL-1-E-selectin bond has a higher k_{off} and lower x_β than the PSGL-1-P-selectin bond indicating that the E-selectin mediated interaction has a shorter bond lifetime in the absence of force, but increased resistance to rupture in presence of force which may decrease neutrophil rolling velocities on E-selectin in shear flow (27, 41). It is worth noting that single molecule force spectroscopy typically yields lower k_{off} and higher x_β when compared to flow chamber assays likely due to the increased ability to measure single bonds via BPF and MFP.

Selectin-ligand binding can exhibit both slip and catch bond behavior. To account for this behavior the two-pathway model was developed. Here the selectin-ligand bond is considered to be most stable under some nominal applied force. Consequently at low and high force regimes the bond is unstable and will rupture. Therefore the graph of bond lifetime plotted against rupture force increases with applied force in the catch regime and decreases with applied force in the slip regime. The presence of catch bonds in selectin binding has been observed through both single molecule force spectroscopy and flow chamber assays (43). In these experiments immobilized PSGL-1 was brought in contact with P-selectin at a constant force and the bond lifetimes were recorded. As a result the biphasic pattern of bond lifetime versus rupture force was observed indicating the switch from catch to slip bond (47). The existence of catch/slips bonds is thought to regulate the binding of leukocytes in shear flow (48).

1.2.4 Adhesion mechanics in shear flow

Increasing evidence suggests that receptor-ligand interactions mediate tumor cell arrest in microvasculature. While the single molecule kinetic and micromechanical properties of these binding events affect the binding characteristics of cells in the presence of flow, they are properties that are measured in the absence of an applied force and therefore it is important to explore these interactions in physiologically relevant conditions. The flow chamber assay has such been utilized to recapitulate binding in the presence of hydrodynamic flow (31, 49).

In this assay, a cell or ligand coated bead passes through the flow chamber and is thought to be in "free motion" when it is traveling at or near the hydrodynamic velocity of the fluid. If the cell initiates bonds with the receptor coated surface its velocity is depressed and the formation of bonds will tether the cell to the surface. If a cell continues to travel significantly slower than the hydrodynamic velocity it is said to be rolling on the surface, mediated through the repeated formation and dissociation of receptor-ligand bonds. If a cell is stationary on the surface for several seconds to minutes, it is considered to be firmly adhered or arrested.

The mechanics of cell rolling on selectins is a complex process that relies on many factors including the strength of receptor-ligand bonds, cell deformability, microvilli extension, and surface receptor and ligand densities. However, this system can be simplified by a series of assumptions that will be detailed in Chapter 2.2. From the flow chamber assay, the bond lifetime can be determined from the tethering time of the cell on the substrate at low receptor and ligand densities. Dissociation kinetics can be calculated by plotting the bond lifetime against the fraction of bound cells at a given shear stress. In selectin-ligand binding the stressed dissociation rate (k_r) was found to increase with increasing shear stresses. From this data unstressed dissociation constant and reactive compliance can be estimated.

Receptor-ligand binding interactions in flow conditions are found to fall into four categories based on the values of the unstressed dissociation constant and reactive compliance. As either the reactive compliance or unstressed dissociation constant of binding interactions decrease for specific binding pairs expressed on the cell surfaces, cell-cell interactions transition from displaying no adhesion, to transient adhesion, to rolling and eventually firm adhesion at a given shear stress (49). This state diagram explains why selectin-mediated adhesion typically results in cell rolling, as the single bond kinetic properties are in the range necessary to facilitate this interaction.

However, as mentioned previously, these experiments are performed at low receptor densities to encourage the formation of single bonds. While this increases the analytical power of these assays it is not physiologically relevant, because multiple bonds can form in shear flow. Recently a comprehensive model has been developed that incorporates multiple bond formation into the calculation of 2D receptor-ligand kinetics in shear flow (50, 51). This model will be discussed in greater detail in Chapter 2.2.

1.2.5 Functional selectin ligands – PODXL, MUC16 and CD44

It is vital to distinguish between structures that only interact with selectins in vitro and the functional selectin ligands that interact with selectins selectively and with high affinity in vivo and whose depletion suppresses selectin-mediated binding. Our lab has recently identified podocalyxin (PODXL), mucin 16 (MUC16) and CD44 as functional selectin ligands in pancreatic and colon carcinoma (42, 52, 53).

PODXL is a transmembrane glycoprotein that belongs to the CD34 family of proteins. It was originally found in the kidney where it is an integral component of glomerural podocytes (54). It is a transmembrane protein with a molecular weight of 49 kDa, however due to extensive O-linked glycosylation the observed molecular weight is approximately 140 kDa (55). The PODXL molecule possesses a short cytoplasmic tail on the C-terminal, a single pass transmembrane domain, a short juxtamembrane stalk and cysteine-containing globular domain, and a longer extracellular mucin-like domain, which is heavily glycosylated.

While PODXL is expressed in kidney cells, recently it has been found to be present in the developing embryo and highly expressed in some tumor types. Clinically, PODXL expression is associated with highly aggressive tumors and poor prognosis in several cancers (56) including invasive colorectal cancer (57); it has also been identified as a diagnostic marker for pancreatic ductal adenocarcinomas originating in gastrointestinal and bile ducts (58). Increased levels of PODXL in tumor cells have also been associated with increased invasion and migration (5) which is thought to result from the activation of RhoA though direct binding with erzin (59). However, work in our lab has found this relationship to be more complicated in pancreatic cancer cells with endogenously express PODXL. PODXL has also been identified as a major functional ligand of E-selectin that is expressed on pancreatic tumor cells (52, 53).

MUC16, also known as cancer antigen 125 or CA-125 is a component of cells in the respiratory track and epithelia in the female reproductive track. Since MUC16 is a heavily glycosylated protein it acts as a hydrophilic protective barrier on the apical side of epithelial cells (60). MUC16 has also been identified as tumor biomarker for certain types of cancer (61). The MUC16 molecule has a cytoplasmic tail, a transmembrane region, extracellular SEA modules and a repeated amino acid sequence, which is high in serine, threonine, and proline. The extracellular region is heavily O-glycosylated and therefore has an observed molecular weight between 3000-5000 kDa (62).

MUC16 is a heavily glycosylated transmembrane protein, which is expressed in epithelial ovarian cancer (61, 63) and metastatic pancreatic cancer cells but not in normal pancreatic cells (53, 64). MUC16 binds to mesothelin which may allow tumor cells to more easily bind to themselves, and thus increase tumor mass at metastatic sites, and can increase cell migration and invasion in pancreatic cancer (62, 65). MUC16 expression strongly correlates with poor survival for both ovarian and pancreatic cancer (62, 66). Furthermore MUC16 binds to both E- and L-selectins in shear flow. While both MUC16 and PODXL serve as functional E-/L-selectin ligands (52, 53), little is known about the mechanical properties of these interactions.

CD44 is expressed on multiple human cell types, and is critical in several cellular functions including lymopcyte homing, inflammation and tumor metastasis. CD44 is the major cell ligand for hyaluronic acid (HA), fibrin(ogen) and P-selectin (67-69). It is a single pass transmembrane protein that undergoes alternate slicing of 20 exons to produce several different isoforms. Exons 1-5, 16-18 and 20 are spliced together to from the smallest isoform of CD44 known as CD44s (68). Exons 6-15 can be alternately spliced together and inserted in the extracellular domain to form CD44 variant isoforms (CD44v). As a result the unglycosylated form of CD44s has a molecular weight of 37 kDa while CD44v has a molecular weight ranging from 100-250 kDa (70). CD44 has a short cytoplasmic tail on the C-terminal, a single pass transmembrane domain, a short stalk region, which the variants are inserted, and extracellular hyalauronan-binding domain, which can be glycosylated.

While CD44 has been extensively studied it remains unclear where CD44 enhances or limits cancer metastasis (71-73). However, what is known is that CD44 is a functional P-selectin ligand and HA ligand (67-69). HA is a major component of the extracellular matrix in most tissue, and is upregulated on the surface of endothelial cells activated with an inflammatory stimuli (74, 75). HA binding to CD44 has been indicated to increase cancer metastasis and invasion (76, 77) and the HA-CD44 bond has been found to enable the slow cell rolling and firm adhesion of cells (67, 78, 79).

1.3 Giant obscurins and cancer

While it is clear that selectin ligands like PODXL and MUC16 are involved in pancreatic cancer metastasis, numerous other tumor suppressors and oncogenes play a pivotal role in cancer progression and metastasis. Interestingly, an analysis of over 13 thousand genes in breast and colorectal cancer found that out of 189 highly mutated genes only TP53 and OBSCN were commonly mutated in both tumor types (80). In a separate study involving pancreatic cancer, the oncogenes KRAS and TP53 were found to be commonly mutated as expected, however mutations in the *OBSCN* gene were also observed in pancreatic intraepithelial neoplasia and pancreatic ductal adenocarcinoma (81, 82).

Obscurins are giant cytoskeletal proteins with structural and regulatory roles. At first, obscurins were found to play a role in the structural organization and contractile activity of striated muscles (83). Obscurins are encoded by the *OBSCN* gene*,* which spans 150 kb on chromosome 1q42 (84, 85). The gene can undergo alternate splicing which results in at least 4 isoforms (84, 85). Obscurin A is ~720 kDa and contains various signaling and adhesion domains, including repetitive immunoglobulin (Ig) and fibronectin-III (Fn-III) domains on the amino-terminus and IQ motif, src-homology 3 and Rho-guanine nucleotide exchange factor (Rho-GEF) and pleckstrin homology (PH) motif interspersed by nonmodular sequences on the carboxyl-terminus (86, 87). Obscurin B, has a mass of ~870 kDa and contains two serine/threonine kinase domains in place of the nonmodular sequences (84, 85). Smaller isoforms, which contain the serine/threonine kinase domains may also be expressed independently (~55 kDa) or in tandem (~145 kDa) (88).

Most of what is known about obscurins pertains to what is known about their function in skeletal and cardiac muscle. However recently, studies have shown that obscurins are present in many cell types and affect several cellular functions. Obscurin isoforms are present in breast, colon, and skin epithelial cells lines, primarily at the cell-cell junctions, the golgi, the nucleus, and the plasma membrane (89). Mutant forms of the obscurin protein were found in solid tumors, indicating that the loss of obscurin may play a role in cancer formation and progression (80, 90).

Recent studies show that in normal breast epithelial cells, obscurins were highly expressed and distributed at cell-cell junctions, (89), however obscurins are markedly decreased in breast cancer cell lines and late stage breast cancer biopsies (89, 91).

Further, the depletion of giant obscurins from breast epithelial cells is correlated with increased apoptotic resistance (89), adherence junctions disruption leading to epithelial-to-mesenchymal transition (EMT), increased tumorigenicity, microtentacle formation, and metastasis (91, 92).

Interestingly because giant obscurins A and B contain several critical binding domains they were found to affect multiple cellular processes resulting in increased cell migration and tumor formation in vivo. The PH domain of obscurin binds to the p85 regulatory subunit of PI3K in breast epithelial cells leading to increased cell migration and EMT (93). Further, the loss of obscurin, and consequently the loss of the obscurin-rhoGEF domain has been found to reduce levels of active RhoA in breast epithelial cell lines. Decreases in RhoA activity can affect many cellular processes including cell migration, actin contractility and microtubule dynamics (94-96) as well as drive tumor cell migration and invasion (97). Further, because myosin II is a downstream effector of the RhoA/ROCK pathway and myosin II activity promotes tyrosine-phosphorylation of paxillin, alterations to RhoA activity can affect formation of focal adhesions (98, 99).

While these studies have been explored in breast epithelial cell lines, the role of giant obscurins in pancreatic cancer has gone unexplored. While mutations in the *OBSCN* gene have been associated with pancreatic ductal adenocarcinoma (81, 82) little is known about how giant obscurins affect the growth and migration of pancreatic cells in ways that are relevant to the metastatic process. However, given that giant obscurin has numerous binding domains, the effect of obscurin depletion in other cancers, and its implications in pancreatic cancer we look to comprehensively evaluate the loss of obscurin from pancreatic cell lines in this work (Chapter 5).

1.4 Cancer metastasis treatments and hurtles

As mentioned previously 90% of deaths related to cancer are from the resulting metastasis and not the primary tumor; however, little attention has been paid to developing antimetastasis drugs due to several significant hurtles. Most chemotherapy treatments focus on primary tumors and currently only several antimetastatic drugs have been developed and licensed (100). However most do not show clinically beneficial results and therefore any breakthrough in cancer metastasis treatment will lead to considerable improvements in therapy and patient outcome (101).

Currently there are two types of FDA licensed or internationally available types of drugs that have been developed to treat cancer metastasis (102-104). They are anti-vascular/anti-angiogenesis drugs and matrix metalloproteinase (MMP) inhibitors (103, 104). Unfortunately, due to minimal survival benefits for patients and indiscriminant molecular inhibitions that result in side effects, these drugs are not succeeding clinically (100). As a result, these drugs, with the exception of some antibodies offer no therapeutic benefits. As we established earlier the metastatic process is complicated and long, and targeting angiogenesis or MMPs (cell invasion) targets only a small portion of this process. Finding new targets and delivery methods are critically important to developing new drugs, which can decrease metastasis and increase patient survival in a clinical setting (101).

One such potential target is sialic acid, which composes the binding interface between PODXL and MUC16 and the lectin domain of selectins. Sialic acid plays a role in the cell binding pertinent to cancer metastasis and can act as a potential target because metastatic cell lines express higher levels of sialyl glycoproteins and glycolipids (100). In fact, patient tumors with higher levels sialyl Lewis x or a antigens are linked with poor prognosis. Other potential targets are cell-signal inhibitors, TGF-β inhibitors, cell adhesion molecules and cell motility inhibitors (105, 106). While these targets and/or inhibitors have potential, they have not yet been licensed.

Both small molecules and antibodies are currently being developed to treat the various components of cancer metastasis. Small molecule drugs can be designed to restore the function or expression of a metastasis suppressor protein. Drugs affecting NM23, E-cadherin, TGF-β and NDRG1 are undergoing clinical trials (105). Monoclonal antibodies are also an attractive option. Antibodies can be targeted to the sialic acid antigen, to block the rolling and adhesion of cancer cells in circulation. Furthermore antibodies binding to c-Met, TGF-β, MKK4 have already developed and are in preclinical trials. Interestingly preclinical results have shown that antibodies against TGF-β have a weak effect on primary tumor growth but strongly suppress cancer metastasis (107). In general if the target is considered specific, then antibodies are thought to be a very effective treatment option although questions about stability and delivery still need to be addressed (105).

1.5 Monobodies an antibody alternative

One possible alternative to antibodies are antibody mimetic scaffold proteins like monobodies. While monoclonal antibodies have typically been explored as therapeutic biomolecules, they are large in size, require eukaryotic expression for production (108), and offer poor thermal stability (109). As a result of these downfalls, synthetically designed antibody mimetic proteins based on molecular scaffolds have recently gained popularity. While engineering these proteins a conserved protein scaffold acts as a base and combinatorial engineering techniques are utilized to select for high affinity binding, conformational stability or any relevant parameter (110, 111). As a result, engineered protein scaffolds have been used as both therapeutics (112) and diagnostics (113).

One such antibody mimetic protein is the monobody which is derived from the tenth fibronectin III domain (FNfn10) scaffold (114, 115). Similar to the immunoglobulin complementarity determining region, this ~94 amino acid peptide contains a β-sheet backbone or scaffold and three commonly modified loop domains (114, 115). The three loops are diversified using phage or yeast display combinatorial libraries in order to produce proteins known as monobodies, with high binding affinities (116-118) and the capability to bind to numerous targets such as small ubiquitin-related modifiers (SUMO) (119), maltose-binding protein (MBP) (116, 117), and fyn kinase (120). Monobodies offer similar binding affinity to antibodies with several advantages including the absence of disulfide bonds, ease of production in bacterial systems (114, 121), and high thermal stability (122). These are just some of the reasons why monobodies have become attractive alternatives to antibodies as therapeutic biomolecules.

Recently, monobodies have been designed to act as potential cancer treatments. Monobody NS1 was engineered to bind to RAS proteins and inactivate the RAF dimer, which in turn was indicated to lead to changes in cell cycle progression (123). Additionally, monobodies have been designed to bind to the Src homology 2 domain at the phosphotyosine-binding site effectively inhibiting Bcr-Abl kinase activity resulting in the cell death of chronic leukemia cell lines in vitro (124). Because of their thermal stability and small size, monobodies have considerable potential as a cancer therapy.

However, to this day monobodies have not been engineered as a treatment for cancer metastasis. Therefore, a better understanding of monobody interactions with their ligands will allow for improved monobody design and hopefully the design of monobodies to target metastatic antigens such as PODXL and MUC16. Furthermore, with the growth of structural databases and increased computing speeds structure-based design of therapeutic molecules is becoming increasingly viable and important (125, 126). With an increased interest in the development of scaffold based mimetic proteins, an understanding of monobody-ligand interaction will lead to the creation of better-targeted and affective therapeutics (40).

Chapter 2

CALCULATIONS AND MODELS

The following section will detail some of the calculations, models and assumptions used to complete this work, specifically the calculations and flow-based adhesion models utilized in Chapters 3 and 4.

2.1 Bell model for determining single molecule force spectroscopy kinetic parameters

The first expression on force dependence on bond lifetime was proposed by GI Bell is seminal 1978 paper (127).

$$k_r(f) = k_r^0 \exp\left(\frac{r_0 f}{k_B T}\right) \qquad \text{Equation 2.1.1}$$

In this equation $k_r(f)$ is the reverse reaction rate or dissociation constant as a function of force. k_r^0 is the dissociation constant in the absence of an applied force. f is the applied force per bond. r_0 is a parameter that describes how strongly the reaction rate changes with force, having units of length. Finally $k_B T$ is the Boltzmann constant times the absolute temperature (127, 128).

When using the AFM to measure single bond unbinding the cantilever is retracted at a constant velocity and therefore $\Delta x/\Delta t$ is constant. Neglecting the deformability of the surface the load on the bond increases $\frac{\Delta f}{\Delta t} = k_f \frac{\Delta x}{\Delta t}$ where k_f is the spring constant of the cantilever. Because the mechanical loading is slow compared to thermal impulses the probability of bond rupture is represented by a first order kinetic process, with a dissociation rate that is time dependent (129). Therefore for a small time interval (t, t + dt) the probability of bond rupture is expressed by the following equation:

$$p(t, f) = k_r(f) \exp\left(- \int_0^t k_r(f(t'))d\,t'\right) \qquad \text{Equation 2.1.2}$$

The first term is the probability of bond rupture for a short time interval (dt), while the second term represents the probability of the bond to survive until time t. When the time is such that the $f = f_{crit}$, and the bond is about to rupture. This corresponds to a peak in the probability distribution where $\frac{\partial p}{\partial f} = 0$. If we assume a linear ramping force then $f(t) = r_f$t then:

$$k_r(f_{crit}) = r_f \frac{\partial}{\partial f} \ln k_r(f) \Big| f = f_{crit} \qquad \text{Equation 2.1.3}$$

By substituting the Bell model (Equation 2.1.1) into the above equation and rearranging you get:

$$f_{crit} = \frac{kT}{r_o} \ln\left(\frac{r_o}{k_r^0 kT}\right) + \frac{kT}{r_o} \ln r_f \qquad \text{Equation 2.1.4}$$

Therefore the relationship between the log of the loading rate and the rupture force is linear, and the slope, y-intercept can be determined:

$$slope = \frac{kT}{r_o}; intercept = \frac{kT}{r_o} \ln\left(\frac{r_o}{k_r^0 kT}\right) \qquad \text{Equation 2.1.5}$$

By plotting the natural log of the loading rate (r_f) against the rupture force f_{crit} the slope and y-intercept are as seen above. Therefore the reactive compliance (x_β) and unstressed dissociation constant (k_{off}^0) can easily be found. These parameters will be utilized for calculations in Chapter 3. Note $x_\beta = r_o$ and $k_{off}^0 = k_r^0$.

$$x_\beta = \frac{kT}{slope};\ k_{off}^0 = \frac{x_\beta}{kT} e^{\frac{kT}{intercept\, x_\beta}} \qquad \text{Equation 2.1.6}$$

2.2 Flow based determination of bond number and $A_cM_rM_lK_{on}$ – The multibond model

To determine the 2D binding affinity ($A_cM_rM_lK_{on}$) and the number of bonds needed to facilitate cell or ligand coated microsphere binding we must first determine the dissociation constant in the presence of shear flow for a slip bond (k_{off}). The following equation is based on the bell model and is used to determine the k_{off} in the presence of shear flow for a single bond interaction (50).

$$k_{off} = k_{off}^0 \exp\left(\frac{x_\beta f}{k_B T}\right) \qquad \text{Equation 2.2.1}$$

In the above equation, k^0_{off} is the dissociation constant in the absence of force as determined above, x_β is the reactive compliance as determined above, f is the force on the cell, and k_BT is the Boltzmann constant times the absolute temperature. However, cell binding/unbinding may be facilitated by additional bonds, especially in selectin-mediated binding and therefore the equation is modified to incorporate multiple bonds, which break either at once (Equation 2.2.2) or in a stepwise fashion (Equation 2.2.3).

$$k_{off,n} = k^0_{off} \exp\left(\frac{x_\beta f}{n k_B T}\right) \qquad \text{Equation 2.2.2}$$

The dissociation constant in the presence of force for multiple breaking bonds is ($k_{off,n}$) is the same as what we established in Equation 2.2.1 with the applied force on the cell divided by the number of bonds (n) that are formed. In the second case, bonds break in a stepwise fashion such that the force is distributed amongst the remaining bonds. The cell will dissociate from the surface when the last bond has broken. Therefore the bond lifetime is:

$$t_{total} = t_n + t_{n-1} + t_{n-2} \ldots t_1 = \sum_{i=1}^{n} \frac{1}{k_{off,i}} \qquad \text{Equation 2.2.3}$$

The apparent off-rate for n-bonds breaking is a stepwise fashion is:

$$k_{off,n} = \frac{1}{\sum_{i=1}^{n} \frac{1}{k_{off,i}}} = \frac{1}{\sum_{i=1}^{n} \frac{1}{k^0_{off} \exp\left(\frac{x_\beta f}{i k_B T}\right)}} \qquad \text{Equation 2.2.4}$$

Now that we have determined the dissociation constant in the presence of hydrodynamic force we can use these values in conjunction with an analytical model developed by Cheung and Konstantopoulos to determine the 2D kinetics of cell binding in shear flow (50). First the probability of the cell forming i-number bonds to a substrate mediated through a constant number of receptor and ligand bonds is determined. The probability vector is:

$$P_o,\ P_1, P_2, P_3, \dots\ P_i\ \dots\ P_{A_c M_{min}}, \qquad \text{Equation 2.2.5}$$

Here M_{min} is defined as the minimal site density of either receptor molecules (M_r) or ligand molecules (M_l) as this number will dictate the maximum number of bonds that can be formed between the cell and the substrate. P_i is the probability of i-bonds forming with i ranging from 0 to $A_c M_{min}$ with A_c being the area of contact between the cell and substrate. Assuming a one-step kinetic system with a receptor (R) binding to its ligand (L) to form a bond (B) the interaction will take the form of the following equation.

$$R + L \underset{k_{off}}{\overset{k_{on}}{\leftrightarrow}} B \qquad \text{Equation 2.2.6}$$

Here k_{on} is the on-rate and is k_{off} is the dissociation constant of the unstressed bond. The rate of change of the probability of bonds forming is governed by the following equation (39, 130):

$$\frac{dP_i}{dt} = k_{off}P_{i+1}(i+1) - \left\{\frac{k_{on}}{A_c}(A_c m_r - i)(A_c m_l - i) + ik_{off}\right\}P_i$$

$$+ \frac{k_{on}}{A_c}\{A_c m_r - (i-1)\}\{A_c m_l - (i-1)\}P_{i-1} \qquad \text{Equation 2.2.7}$$

This equation represents the change in the probability of forming *i* number bonds over some time t. Therefore, P_i is the probability of having *i* number bonds. The first left hand term is the probability of (i+1) bonds losing a bonding in the span of time t. The second term is the probability of *i* bonds losing or gaining a bond in time t while the third term is the probability of (i-1) gaining a bond in time t. If we assume the small number of bonds formed will have no affect on the available number of receptors and ligands available for binding we can make several simplifying assumptions. In this regard, we can neglect the *i* and (i-1) in the terms $(A_c m_r - i)$ and $(A_c m_r - (i-1))$. Solving for P_i, the equation takes the form of the Poisson distribution.

$$P_i(x) = \frac{\langle i\rangle^i}{i!}\exp\left(-\langle i\rangle\right) \qquad \text{Equation 2.2.8}$$

Where $\langle i\rangle$ is the average number of bonds and is represented by the following equation:

$$\langle i\rangle = A_c m_r m_l \frac{k_{on}}{k_{off,n}}\left(1 - \exp\left(-k_{off,n}t\right)\right) \qquad \text{Equation 2.2.9}$$

Here, t is the contact time between the ligand and receptors. For the experiments discussed in Chapters 3 and 4, this time can be approximated to be the time the cell or microsphere spends as it passes over the ligand coated glass surface. This approximation is valid given the height of the flow chamber ~22.5 microns, which allows flowing cells to easily contact the ligand-coated surface (50). Given this we can define the contact time as x/U_d, or the length of each ligand coated patch divided by the hydrodynamic cell velocity. Therefore we can approximate the probability of cells binding (N_B/N_T) to the ligand-coated surface as a function of ligand patch length (x).

$$\frac{N_B(x)}{N_T} = \sum_{i=n}^{A_c m_{min}} P_i(x) = 1 - \sum_{i=0}^{n-1} P_i(x) \qquad \text{Equation 2.2.10}$$

By knowing the off-rate, which can be determined through single molecule for spectroscopy, the force on the cell which has been reported in literature for cells and microspheres (131) and the experimentally observed fraction of binding cells for each ligand patch length, the number of bonds needed to facilitate binding (i) and the 2D binding on rate ($A_c m_r m_l k_{on}$) can be calculated. These parameters are calculated by minimizing the sum of the squares of the residual for (N_B/N_T) at each patch length and optimizing these two variables to accurately represent the experimental data.

2.3 Shear stress calculation

Determining the shear stress at the binding interface is critically important to ensure that shear stresses are maintained in a range that is physiologically relevant. To determine the wall shear stress several assumptions must be made and they are as follows: The flow in the chamber is laminar. The system is at steady state and the density and viscosity remain constant. The flow is only in one dimension and the flowchamber width and length are much greater than the height.

The dimensions of the flow chamber are 2 cm × 500 µm × 20 µm or 2 cm × 1000 µm × 22.5 µm (length × width × height) and therefore the Reynolds number of flow Re<<1. Given that Re<2000, the flow can be considered laminar. The system is operated with a syringe pump and no changes in cell velocity were noted as they passed through the field of view. The buffer is largely composed of water, because water is a non-compressible Newtonian fluid we can assume it is at density and viscosity are constant. Next measurements were recorded at the interior of the device where fluid flow is one-dimensional. Finally both the chamber width and length are much greater than the chamber height.

Given that our assumptions are justified we can set up our system and solve for the shear stress of the binding interface. To solve this classic transport problem, the boundary must be established. The system can be approximated as parallel plate flow system, the fluid velocity is established in the x direction (v_x), and the velocity the bottom wall (y=0) and the top wall (y=h) is equal to zero because of the no slip condition. Also we establish that the pressure at both the inlet and outlet are equal to P_o and P_L. We can then start with the equation of continuity.

$$\frac{\partial p}{\partial \mathrm{t}} + \nabla \cdot (pv) = 0 \qquad \text{Equation 2.3.1}$$

Here, the velocity of the fluid is v and the fluid density is p. Expanding the equation and considering that the fluid is at steady state and incompressible ($\frac{\partial p}{\partial \mathrm{t}} = 0$) and that flow is only in the x direction ($\frac{\partial \mathrm{v}}{\partial \mathrm{y}} = 0, \frac{\partial \mathrm{v}}{\partial \mathrm{z}} = 0$) that gives us the equation:

$$\frac{\partial \mathrm{v}_x}{\partial \mathrm{x}} = 0 \qquad \text{Equation 2.3.2}$$

Using the Naviar-Stokes equation we can then solve for the velocity and shear stress profiles. Looking at the x component of flow the Naviar-Stokes equation takes the following form.

$$p\left(\frac{\partial v_x}{\partial t} + v_x\frac{\partial v_x}{\partial x} + v_y\frac{\partial v_x}{\partial y} + v_z\frac{\partial v_x}{\partial z}\right) = -\frac{\partial P}{\partial x} + \mu\left(\frac{\partial^2 v_x}{\partial x^2} + \frac{\partial^2 v_x}{\partial y^2} + \frac{\partial^2 v_x}{\partial z^2}\right) - pg_x$$

Equation 2.3.3

Here, g_x is gravity in the x direction. If we acknowledge the assumption that flow is only in the x direction, the system is at steady state and apply the result found in Equation 2.3.2 then the left side of the equation reduces to zero and the right side reduces to the following:

$$0 = -\frac{\partial P}{\partial x} + \mu\frac{\partial^2 v_x}{\partial y^2} - pg_x \qquad \text{Equation 2.3.4}$$

Grouping terms and defining a new pressure term P* which incorporates the pressure and gravity terms yields the equation:

$$-P^* = \mu \frac{\partial^2 v_x}{\partial y^2}$$ Equation 2.3.5

Solving for v_x and applying the boundary conditions that $v_x = 0$ at $x = 0$ and h results in the following equation:

$$v_x = \frac{P^*}{2\mu}(hy - y^2)$$ Equation 2.3.6

To cancel out the pressure term we solve for the volumetric flow rate by integrating the average velocity by the cross sectional area of the flow chamber. This calculation results in the following equation.

$$P^* = \frac{12\mu Q}{h^3 w}$$ Equation 2.3.7

In the preceding equation Q is the volumetric flow rate, h is the height of the flow chamber and w is the width of the flow chamber. We can then solve for the shear stress at the wall and substitute in Equation 2.3.7 in for P*. This allows us to calculate shear stress as a function of either flow rate or the average cell velocity.

$$\tau_{wall} = \frac{6\mu Q}{h^2 w}$$ Equation 2.3.8

$$\tau_{wall} = \frac{6\mu v_{avg}}{h}$$ Equation 2.3.9

Therefore we can calculate the shear stress at the wall if either the flow rate is controlled via a syringe pump or if the average velocity of flow is known.

Chapter 3

DISTINCT KINETIC AND MECHANICAL PROPERTIES GOVERN MUCIN 16- AND PODOCALYXIN-MEDIATED TUMOR CELL ADHESION TO E- AND L-SELECTIN IN SHEAR FLOW

Selectin-mediated tumor cell tethering to host cells, such as vascular endothelial cells, is a critical step in the process of cancer metastasis. We recently identified sialofucosylated mucin16 (MUC16) and podocalyxin (PODXL) as the major functional E- and L-selectin ligands expressed on the surface of metastatic pancreatic cancer cells. While the biophysics of leukocyte binding to selectins has been well studied, little is known about the mechanics of selectin-mediated adhesion pertinent to cancer metastasis. We thus sought to evaluate the critical parameters of selectin-mediated pancreatic tumor cell tethering and rolling. Using force spectroscopy, we characterized the binding interactions of MUC16 and PODXL to E- and L-selectin at the single-molecule level. To further analyze the response of these molecular interactions under physiologically relevant regimes, we used a microfluidic assay in conjunction with a mathematical model to study the biophysics of selectin-ligand binding as a function of fluid shear stress. We demonstrate that both MUC16 and PODXL-E-selectin-mediated interactions are mechanically stronger than like L-selectin interactions at the single-molecule level, and display a higher binding frequency at all contact times. The single-molecule kinetic and micromechanical properties of selectin-ligand bonds, along with the number of receptor-ligand bonds needed to initiate tethering, regulate the average velocity of ligand-coated microspheres rolling on selectin-coated surfaces in shear flow. Understanding the biophysics of selectin-ligand bonds and their responses to physiologically relevant shear stresses is vital for developing diagnostic assays and/or preventing the metastatic spread of tumor cells by interfering with selectin-mediated adhesion.

3.1. Introduction

E- and L-selectins play a vital role in cell-cell interactions pertinent to cancer metastasis. E-selectin (CD62E) is expressed on activated vascular endothelial cells and is thought to promote the tethering and rolling of malignant cells, acting as a critical step for their extravasation to the interstitial space and eventual seeding of new metastatic foci (31, 132, 133). L-selectin (CD62L) is constitutively expressed on the surface of leukocytes, and promotes the recruitment of leukocytes to the metastasizing tumor microenvironment; deficiencies in L-selectin lessen metastatic spread in mice (36, 134). Although E- and L-selectins share a similar structure, their binding kinetics and distribution differ considerably leading to distinct roles in cancer metastasis. At the lectin domain, selectins recognize sialofucosylated oligosaccharides such as sialyl-Lewis x (sLe^x) and its isomer sialyl-Lewis a (sLe^a) on interacting cells (30-33). Notably, sLe^x is absent from normal pancreas tissue (34, 35), but its expression is observed in pancreatic ductal adenocarcinoma and high-grade pancreatic intraepithelial neoplasia lesions (34). Because the binding affinity of selectins for monocovalent $sLe^{x/a}$ is low, it is vital to distinguish between structures that only interact with selectins *in vitro* and the *functional* selectin ligands (36) that interact with selectins selectively and with high affinity *in vivo* and whose depletion suppresses selectin-dependent binding. We recently identified sialofucosylated mucin 16 (MUC16) and podocalyxin (PODXL) as the major functional E- and L-selectin ligands expressed on the surface of metastatic pancreatic cancer cells (52, 53).

PODXL is a transmembrane glycoprotein that belongs to the CD34 family of proteins. Clinically, PODXL expression is associated with highly aggressive tumors and poor prognosis in several cancers (56) including invasive colorectal cancer (57); it has also been identified as a diagnostic marker for pancreatic ductal adenocarcinomas originating in gastrointestinal and bile ducts (58). MUC16 is a heavily glycosylated transmembrane protein, which is expressed in epithelial ovarian cancer (61, 63) and metastatic pancreatic cancer cells but not in normal pancreatic cells (53, 64). Although both MUC16 and PODXL serve as functional E-/L-selectin ligands (52, 53), little is known about the mechanical properties of these interactions.

To determine the mechanical properties of the PODXL/MUC16-E-/L-selectin interactions, we utilized single-molecule force spectroscopy and microfluidic adhesion assays coupled with a mathematical model. Using force spectroscopy, we determined the kinetic (k_{off}°) and micromechanical (x_{β} and tensile strength) properties of receptor-ligand interactions at the single-molecule level. By combining these measurements with microfluidic adhesion assays and mathematical modeling, we determined that the k_{off}° and tensile strength of these selectin-ligand bonds, along with the number of bonds needed to mediate tethering, regulate the velocity of ligand-coated microspheres rolling on selectin-coated surfaces in shear flow. This integrated approach contributes to the understanding of how two major pancreatic cancer surface glycoproteins bind to E-/L-selectins in the presence of hydrodynamic shear, which can lead to the improved diagnosis and prevention the metastatic spread of pancreatic cells.

3.2. Materials and Methods

3.2.1 Reagents and monoclonal antibodies

Anti-human PODXL monoclonal antibody (3D3) was from Santa Cruz Biotechnology (Santa Cruz, CA) while the anti-human MUC16 monoclonal antibody (M11) was from Dako (Carpinteria, CA). PEI was from Polysciences (Warrington, PA). DMPC was from Avanti Polar Lipids (Alabastar, AL).

3.2.2 Cell culture, whole cell lysis and immunoprecipitation

Human pancreatic adenocarcinoma SW1990 cells were obtained from the American Type Culture Collection (Manassas, VA). SW1990-PODXL KD and SW1990-MUC16 KD cells were generated as previously described (52, 53). All SW1990 cells were cultured in DMEM with 10% FBS with 700 μg/ml G418 and 0.5 μg/ml puromycin added to the PODXL-KD and Mucin16-KD media, respectively (Life Technologies, Carlsbad, CA). SW1990 whole-cell lysate was prepared through treatment with 2% Nonidet P-40 followed by centrifugation (52, 53). PODXL and MUC16 were immunopurified using anti-PODXL mAb (3D3) or anti-MUC16 mAb (M11), respectively, using protein G agarose beads (Invitrogen) (135-138).

3.2.3 Lipid bilayer preparation

To prepare the solutions used for the lipid bilayer, 8 mg of DMPC (1,2-dimyristoyl-sn-glycero-3-phosphocholine) was added to 8 mL of lipid buffer B (Tris-HCl, 50 mM NaCl, 1 mM $CaCl_2$, 0.1% (w/v) Triton X-100) (40, 42, 67, 139). 130 µL of either MUC16 or PODXL (concentration 80 µg/ml) was added to 370 µl of the lipid solution and resulting solution was incubated at 37°C for 2h. Following incubation, the solution was transferred to 10 kDa MWCO dialysis cassette and dialyzed against 1 L of lipid buffer A (20 mM Tris-HCl, 50 mM NaCl, 1 mM CaCl2). Buffer A was changed three times every 12 h. After 48 h the dialyzed solution was stored at 4°C under nitrogen. Glass slides were plasma cleaned for 5 min and then incubated with 100 ppm PEI in 0.5 mM KNO_3 for 20 min. Following cleaning with DI water and air, slides were placed in a vacuum desiccator for at least 2 h before use. 4 µL protein-lipid solution was added to the slide for 2 h and the droplet was maintained using a moist towel. Slides were washed 3X using Hank's Balanced Salt Solution (HBSS) before being submerged in HBSS for use in experiments. In select experiments, 10 mM EDTA was added to the HBSS and slides were submerged in the EDTA/HBSS solution.

3.2.4 Cantilever functionalization

Molecular force probe cantilevers from Bruker nano (Camarillo, CA) were silanized with 2% (v/v) 3-amino-propyltriethoxysilane in acetone (67, 140). Cantilevers were incubated for 1 h in 30 µg/ml anti-human IgG-Fc mAb (Abcam, Cambridge, MA) in D-PBS containing a 50-fold molar excess of the bis(sulfosuccinimidyl) croslinker (BS^3; Peirce, Rockford, IL) before quenching with Tris buffer. Cantilevers were then incubated in either 10 μg/ml E-selectin Fc chimera or 10 μg/ml L-selectin Fc chimera (R&D systems, Minneapolis, MN) in D-PBS for 2 h at room temperature and blocked with 1% BSA in D-PBS to limit nonspecific interactions. The concentrations of selectins were optimized to ensure for a low proportion of binding events in force spectroscopy experiments (~20 per 100 contacts).

3.2.5 Single Molecule Force Spectroscopy and Data Acquisition

Experiments were conducted using a MFP (Asylum Research, Santa Barbara, CA). A triangular cantilever tip with spring constant of 10 pN/nm was calibrated using thermal noise amplitude. The deflection was measured by laser reflection on a split photodetector. The petri-dish containing the lipid bilayer or SW1990 cells was positioned directly under the cantilever and adjusted so that each approach generated a slight depression force (~5 nN) on the sample before reproach. The dwell time was set to 20 msec and the reproach velocity was varied from 5-25 μm/sec. Rupture forces and loading rates were determined from force-distance traces using Igor Pro 4.09 software (Wavemetrics, Lake Oswego, OR). For each receptor-ligand pair the successful rupture events were sorted based on the magnitude of the loading rate and ensemble-averaged every 50 rupture events. For each set of binned data the average rupture force and loading rate was calculated and fit to the Bell model (67). Using a least-squares fit to the linear region of a graph of rupture force against the logarithm of the loading rate the Bell model parameters including the unstressed of- rate k_{off}° and the reactive compliance x_{β} were tabulated (67).

3.2.6 Western blot analysis

Immunopurified MUC16 or PODXL were separated using a 3-8% Tris-acetate SDS-PAGE gel (Bio-Rad, Hercules, CA) under reducing conditions. Proteins were transferred to an Immuno-blot PVDF membrane and blocked for 30 min using StartingBlock blocking buffer (Thermo Scientific, Waltham, MA). Membranes were stained with either anti-PODXL mAb (3D3) or anti-MUC16 mAb (M11) and rinsed with TBS/0.1% Tween 20, before being incubated with the appropriate horseradish peroxidase (HRP)-conjugated secondary antibody. SuperSignal West Pico chemiluminescent substrate (Life Technologies) was used to develop the immunoblots (52, 53).

3.2.7 Preparation of MUC16 and PODXL coated microspheres

10μm polystyrene microspheres (2.5×10^7 microspheres/ml; Polysciences, Warrington, PA, USA) were incubated for overnight at 4°C (constant rotation) with either PODXL or MUC16 immunopurified from SW1990 cell lysate, diluted to a predetermined concentration with binding buffer (0.2M carbonate/bicarbonate buffer 9.2 pH) as described previously (135-138). Protein coated microspheres were washed 2X with D-PBS and blocked with D-PBS/1% BSA for 60 min at room temperature. Microspheres were re-suspended to a concentration of 2×10^6 microspheres/ml in D-PBS/0.1% BSA for use in flow-based assays. MUC16 and PODXL expression on the surface of microspheres was determined by flow cytometry (Becton, Dickinson, Franklin Lakes, NJ) (135-138).

3.2.8 Quantification of MUC16 and PODXL site densities on microspheres and SW1990 cells

The site densities of MUC16 and PODXL on microspheres and SW1990 cells were determined by quantitative flow cytometry using a primary anti-MUC16 or anti-PODXL mAb along with an appropriate FITC-conjugated secondary antibody. Background levels were determined by incubating microspheres or cells with properly matched isotype controls (53). To correlate fluorescent intensity values with Molecules of Equivalent Soluble Fluorochrome (MESF) units, we used the Quantum FITC-5 MESF Kit (Bangs Laboratories, Fisher, IN) and established a calibration curve according to the manufacturer's instructions. The MESF values of MUC16- or PODXL-bearing microspheres or cells were determined using calibration curve. Next, Simply Cellular anti-mouse IgG microspheres (Bangs Laboratories, Fisher, IN) with a known antibody binding capacity (ABC) were utilized to determine the fluorescence to protein (F/P) ratio of the antibody staining process. The F/P ratios for PODXL and MUC16 staining were 2.4 and 1.7 FITC to IgG, respectively. The site densities of MUC16 and PODXL on the microsphere or cell surface were determined by multiplying the net MESF values (anti-MUC16 or anti-PODXL mAb minus the matched isotype control) of MUC16 and PODXL by the inverse of their respective F/P ratios and dividing by the surface area. The surface area of microspheres (10 μm in diameter) is 314 μm^2. The surface area of SW1990 was estimated to be 1940 μm^2 as determined by tracing suspended circular cells and using image J for analysis. Flow cytometry assays were performed using a BD FACSCalibur ,and data analysis was performed using BD CellQuest Pro software (BD Biosciences, San Jose, CA).

3.2.9 Selectin patterning via photoligography

A pre-cleaned glass slide was spin coated with micropostit photoresist (S1805, Rohm and Haas, Philadelphia, PA) and exposed to UV through a patterned chrome mask using a previously developed method (51). To render the patterned slide hydrophobic it was sonicated in 0.1% (v/v) octadecyltrichlorosilane (OTS) for 30 min. The slide was then incubated in FITC-conjugated goat anti-human IgG Fc fragment specific antibody (Sigma, St. Louis, MO) before being immobilized with either recombinant E- or L-selectin Fc chimera at concentrations of 5, 10 and 20 μg/ml. As the goat anti-human IgG Fc antibody recognizes and binds the Fc epitope of chimeric selectins, it was selected to ensure the correct orientation of the E-/L-selectin molecules (51, 140). The photoresist was removed using 5% photoresist remover (Rohm and Haas) in acetone before the slide was blocked in 1% BSA in D-PBS for at least 1h prior to the running of experiments. For rolling velocity experiments, the pre-cleaned glass slide was not patterned.

3.2.10 Quantification of E- and L-selectin site densities

E- and L-selectin site densities were determined using a modified Dissociation-Enhanced Lanthanide Fluorescent Immunoassay (DELFIA) method (51). First, E- and L-selectin were labeled with europium (Eu^{+3}) using the DELFIA Eu-Labelling Kit (PerkinElmer, Waltham, MA) according to the manufacturer's instructions. Labeled proteins were isolated using gel filtration chromatography through a column packed with Sephadex G50 (1x10 cm) packed on top of Sepharose 6B (1x9 cm) (both from Sigma). 50 mM Tris-HCl (pH 7.8) supplemented with 0.9% sodium chloride and 0.05% sodium azide served as the elution buffer. 1 ml elution fractions were collected from the columns and assayed for protein content using the BCA assay (Thermo Fisher Scientific, Rockford, IL) and Eu^{+3}-chelate fluorescence (Figure 3.8). Fractions testing positive for both protein and Eu^{+3} were pooled and concentrated by centrifugal filtration through 30,000 MWCO centrifugal filter units (EMD Millipore, Billerica, MA). Concentrated proteins were resuspended in DI water. The final protein concentration was measured using the BCA assay via NanoDrop (Thermo Fisher).

Eu3+ conjugated E- or L-selectin was patterned on glass slides using the identical methodology as was used in the flow-based adhesion or rolling assays. Site densities of E- and L-selectin immobilized on glass surface were assessed by the DELFIA as previously described (51).

3.2.11 Microfluidic flow based adhesion device fabrication

The microfluidic device was fabricated using standard practices using a previously established methodology (51). The dimensions of the device channel used in this experiment were 2 cm × 500 μm × 20 μm (length × width × height).

3.2.12 Microfluidic flow-based adhesion and rolling assays

The microfluidic device was cleaned in ethanol and dried with air before assembly on top of the patterned glass slide. Via a syringe, 0.1% BSA in PBS was introduced into the channel and allowed to flow for 3 min until flow equilibrated. The device was placed on a microscope stage and connected with a syringe pump to control flow. The patches were identified via fluorescence visualization using a Nikon TE300 (Tokyo, Japan). 50 μl of coated microspheres suspended in 0.1% BSA in PBS ($2x10^6$ microspheres/ml) were added to the inlet channel. The percent binding was determined by dividing the number of interacting microspheres by the total number that passed over each patch. A 20x field of view was used and each perfusion lasted 3 min. For rolling experiments, the microchannel device was assembled to a non-patterned selectin coated glass slide, with all other conditions remaining the same. Rolling velocities were determined by dividing the distance the microsphere center of mass traveled by the time taken to travel that distance for each condition tested (67, 138).

3.2.13 Mathematical model of 2-D selectin-mediated cell adhesion on micropatches

The model for selectin binding to 2-D micropatches utilized here was discussed in detail previously (51). All calculations are similar with the exception of k_{off}, which was calculated based on the one-pathway model for step-wise bond rupture (50). The step-wise model was chosen as binding was found to be mediated by a larger number bonds (>5) and simultaneous bond rupture was unlikely. The kinetic constants used were determined via single molecule force spectroscopy.

3.2.14 Statistical analysis

Data are expressed as means ± S.E.M. or S.D. of at least 3 independent experiments. Statistical significance of differences between means was determined by Student's t test or one-way analysis of variance followed by the either the Tukey or Sidak test for multiple comparisons, where appropriate.

3.3. Results

3.3.1 Comparison of the kinetic and micromechanical properties of PODXL/MUC16- E-/L-selectin via single-molecule force spectroscopy

Single-molecule force spectroscopy has been utilized to determine the kinetic properties of selectin-ligand bonds in both purified protein-protein and protein-cell systems (42, 45, 67). Incorporation of the purified protein (e.g., MUC16 or PODXL) into a lipid bilayer allows for its physiologically relevant orientation and provides a consistent binding interface, while eliminating the potential contribution of other selectin ligands present on the tumor cell surface (42, 67, 139). Here, we utilize single-molecule force spectroscopy to evaluate the binding strength of MUC16 and PODXL interactions with both E- and L-selectin. In this assay, E- or L- selectin-coated cantilevers were brought in contact with immunopurified MUC16 or PODXL inserted in a lipid bilayer for a constant dwell time and retracted at designated retraction speeds. The bond rupture force (tensile strength) and loading rates of single binding events were measured over a range of retraction velocities (Figure 3.1A) (42, 139). Dilute E-/L-selectin and ligand concentrations on the cantilever tips and lipid bilayer, respectively, were selected to ensure single bond formation (42, 139). To validate the measurements obtained using immunopurified MUC16 and PODXL (Figure 3.1B), we also tested E-/L-selectin binding to MUC16-expressing (PODXL-knockdown) and PODXL-expressing (MUC16-knockdown) SW1990 pancreatic cancer cells (52, 53).

For all interactions tested, the rupture force varied linearly with the natural log of the bond-loading rate for nearly the entire loading rate regime (Figure 3.2A, B). The rupture force-loading plots were similar for both immunopurified ligand-selectin pairs

(Figure 3.2A, B) and their respective knockdown cell-selectin counter parts. Mean rupture force and rupture force distribution were similar for both protein-protein and cell-protein systems (e.g., 71 pN for MUC16-E-selectin and 74 pN for MUC16-expressing (PODXL-knockdown) SW1990-E-selectin at 1000 pN/s). Using the least-squares fit to the plot of mean rupture force versus the natural log of the loading rate the Bell models parameters, unstressed off-rate k_{off}° (s^{-1}) and reactive compliance x_{β} (nm) were determined for all E-/L-selectin interactions. Both protein-protein and cell-protein systems displayed similar kinetic constants for each pair of interactions (Figure 3.3). Specifically, the k_{off}° was nearly identical for all respective pairs, while x_{β} was moderately lower for the cell-L-selectin system compared to the immunopurified MUC16/PODXL-L-selectin system (Figure 3.3), likely due to the minor differences in protein glycosylation (136, 137). This is in line with prior observations showing that knockdown of a sialofucosylated protein (e.g., CD44v) increases the extent of glycosylation (HECA-452 reactivity) in other glycoproteins (e.g., PODXL) (136, 137). Overall, given the similarities in the mechanical properties of both systems, we conclude that immunopurified MUC16 and PODXL incorporated bilayers represent a reliable system for measuring the interactions between these ligands and E-/L-selectin on the single-molecule level.

The binding frequency for immunopurified MUC16 with E-/L-selectin was 13.6% and 17.3%, respectively (Figure 3.2D,E). While the binding frequency of PODXL-L-selectin interaction was in the same range at 16.3%, it was notably higher at 23.3% for the PODXL-E-selectin pair (Figure 3.2D,E), suggesting a higher on-rate. The addition of EDTA (10 mM) suppressed the binding of all interacting pairs down to basal level

(~5%), which is in accordance with the Ca^{2+} dependence of E- and L-selectin-dependent binding (138). These findings, in conjunction with the minimal binding found with a selectin-blank bilayer interaction (data not shown), help verify the specificity of the selectin-ligand interactions studied here.

The MUC16-E-selectin bond displayed a higher rupture force (tensile strength) at all loading rates when compared to the MUC16–L-selectin bond (71 pN to 56 pN, respectively, at a loading rate of 1000 pN/s) (Figure 3.2A). The k_{off}° was found to be markedly lower for the MUC16-E-selectin bond (0.26 s^{-1}) than for the MUC16-L-selectin bond (0.82 s^{-1}), whereas no significant differences were observed for x_β (Table 3.1). Similarly, the PODXL-E-selectin bond displayed a higher rupture force at all loading rates than the PODXL-L-selectin bond (e.g., 69 pN to 62 pN, respectively, at a loading rate of 1000 pN/s) (Figure 3.2B). The k_{off}° was lower for the PODXL-E-selectin bond (0.33 s^{-1}) when compared to the PODXL-L-selectin dissociation (0.49 s^{-1}), while no significant difference was found for x_β. Bell model parameters for all binding pairs were validated using Monte Carlo simulations (Figure 3.2C). Taken together, both MUC16 and PODXL-E-selectin bonds were determined to be mechanically stronger than the like ligand-L-selectin bonds, as evident by the higher tensile strength, lower bond off-rate and thus lower susceptibility to rupture. Although MUC16- and PODXL- E-selectin bonds have similar kinetic properties and tensile strengths, the PODXL-L-selectin bond is mechanically stronger than the MUC16-L-selectin bond.

3.3.2 Single-molecule kinetic and micromechanical properties along with contact time and site density dictate MUC16 and PODXL binding to E-/L-selectins under flow

To study the biophysics of MUC16/PODXL-selectin binding under flow, we quantified the extent of MUC16- and PODXL- coated microspheres binding to selectins as a function of contact time and selectin site density. Receptor-ligand contact time is regulated by the shear stress and length of the selectin-coated surface in the direction of flow. Using photolithography, E- and L-selectin- coated patches with lengths varying from 10-160 μm and a width of 10 μm were micropatterned onto a glass slide (51). The patterns were spaced 100 μm apart in the direction of flow and selectin-free regions were coated with inert bovine serum albumin (BSA). Over the course of the 3-min experiment, polystyrene microspheres ($2\text{x}10^6$/ml) coated with either MUC16 or PODXL at equivalent site densities (~20 sites/μm^2, Figure 3.7) were perfused over the micropatches at prescribed wall shear stresses. Of note, this site density is in the same range of site densities reported in literature (141-143). The number of ligand-coated microspheres interacting on each patch for each experiment was recorded (N_b). The fraction of microspheres binding to each patch (N_b/N_T) was determined by dividing the interacting microspheres (N_b) by the total number of microspheres to flow over the patch (N_T).

Longer selectin patch lengths increased the fraction of interacting microspheres as ligand-selectin contact time increases with increasing patch lengths (Figure 3.4). Along these lines, we also observed a consistent increase in the fraction of interacting microspheres with decreasing shear stresses and thus correspondingly increasing contact times for all tested interactions (e.g., 4.6%, 6.6% and 12.1% capture efficiency for PODXL-E-selectin interaction using 160 μm long patches coated with E-selectin (3000 sites/μm^2) at 2, 1 and 0.5 dyn/cm^2, respectively) (Figure 3.4H). This monotonic relationship between capture efficiency and shear stress indicates that the shear threshold effect, which is observed in leukocyte tethering (144), does not occur for MUC16- or PODXL- selectin interactions in the shear stress regime studied here.

To investigate the effect of selectin density on capture efficiency, the slides were incubated with three concentrations of E- or L-selectin. Using a modified europium assay (51), we determined the surface site densities of E- and L-selectin plated at concentrations of 5, 10 and 20 μg/ml to be approximately 1800, 3000, and 4800 sites/μm^2, respectively (Figure 3.8). These site densities are in a range similar to those reported in literature (51, 145, 146). Decreasing selectin densities decrease binding for all selectin-ligand pairs (e.g., 7.9%, 6.5% and 5.5% for MUC16-E-selectin interaction at 1 dyn/cm^2 using 160 μm long patches) (Figure 3.4A-C). Ligand-L-selectin binding followed a similar trend; however, the fraction of interacting microspheres was considerably lower than that for ligand-E-selectin interactions (e.g., 3.3%, 1.9% and 0.9% for MUC16-L-selectin interaction at 1 dyn/cm^2 using 160 μm patches) (Figure 3.4D-F). Taken together, the higher tensile strength and lower k_{off}° measured by single-molecule force spectroscopy predict the enhanced capacity of MUC16 and PODXL to bind to E-selectin over L-selectin.

The critical patch length (CPL), defined as the minimum patch length to achieve at least 2% binding, increases with increasing shear stress and decreases with increasing selectin density for both the MUC16 and PODXL-E-selectin interactions (Table 3.2). In line with the force spectroscopy data, the critical patch length was longer for ligand-L-selectin interactions when compared to E-selectin interactions at all shear stresses and selectin site densities studied indicating that the weaker L-selectin-mediated binding requires lower shear stresses and higher selectin site densities to achieve similar binding.

3.3.3 Multiple bonds are needed for tethering to selectins under flow

As shear stress increases, multiple selectin-ligand bonds are often needed to mediate cell tethering to a surface (50, 51). To determine the number of MUC16/PODXL-selectin bonds required to mediate microsphere tethering in shear flow, we fitted the experimental binding data with an analytical multiple bond model (51). This model estimates not only the minimum number of bonds needed for tethering but also the lumped binding affinity ($A_cM_rM_lK_{on}$) by simultaneously optimizing the two parameters (Figure 3.9). The model successfully captured the binding profile for all selectin-ligand pairs examined (Figure 3.5). For all cases, the bond number increased with increasing shear stress. However, the minimum bond number varied for the each interaction based on their binding profiles.

According to the model, the minimum bond number for MUC16-coated microspheres tethering to E-selectin ranges from 4 to 10 when the shear stress increases from 0.5 to 2 dyn/cm^2 (Figure 3.5A). In comparison, the PODXL-E-selectin interaction requires one less bond to mediate binding (3-9 bonds) in shear flow (0.5-2 dyn/cm^2) (Figure 3.5B). When fewer bonds are required for tethering, such receptor-ligand interactions can be initiated at lower contact times, and thus shorter patches, as is the case for PODXL-E-selectin relative to MUC16-E-selectin (Figure 3.5A,B). For both

MUC16/PODXL-E-selectin interactions, bonds increase in a shear dependent manner (Figure 3.5A,B). A similar shear-dependent trend was noted for the MUC16/PODXL-L-selectin interaction (Figure 3.5C,D). While both MUC16/PODXL-L-selectin interactions are mediated by 5 bonds at 0.5 dyn/cm^2, fewer bonds are required for PODXL-L-selectin than MUC16-L-selectin binding at higher shear stresses (Figure 3.5C,D).

The lumped affinity term $A_cM_rM_lK_{on}$ considers the interacting contact area (A_c), the receptor site density (M_r), the ligand site density (M_l) and the binding affinity (K_{on}) calculated for each interaction. Given the equivalent values of M_r and M_l for all samples, the lumped binding affinity is a direct measure of 2-D binding affinity (A_cK_{on}). The model predicts that the PODXL tethering to E-selectin has a ~2 fold higher $A_cM_rM_lK_{on}$ than MUC16-E-selectin at shear stresses ranging from 0.5-2 dyn/cm^2 (Table 3.3). This result is in line with the increased binding frequency measured for the PODXL-E-selectin pair by single-molecule force spectroscopy (Figure 3.2D). In contrast, the lumped affinity is modestly higher for the MUC16-L-selectin than the PODXL-L-selectin pair (Table 3.3).

3.3.4 Single-molecule kinetic and micromechanical properties along with bond number regulate MUC16 and PODXL-dependent rolling on selectins in shear flow

Microspheres (2x10^6/ml) coated with MUC16 or PODXL at equivalent site densities (~20 sites/µm^2) were perfused over glass slides coated with either E-selectin (700 and 1500 sites/µm^2) or L-selectin (4800 sites/µm^2). These selectin site densities were chosen as the perfused microspheres displayed clear rolling behavior. Slower rolling of ligand-coated microspheres was observed on E-selectin as compared to L-selectin substrates (Figure 3.6). As expected, microspheres rolled more slowly on surfaces coated with higher E-selectin density (1500 versus 700 sites/μm^2) (Figure 3.6A,B), as this increases the number of receptors available for binding. On E-selectin substrates, MUC16-coated microspheres rolled significantly slower than PODXL-coated microspheres at the higher E-selectin density and at all shear stress tested (Figure 3.6B) even though the single-molecule kinetic and micromechanical properties are similar for MUC16 and PODXL interactions with E-selectin. This difference in rolling velocity is attributed to the higher number of MUC16 versus PODXL bonds with E-selectin needed to support tethering (Figure 3.5A,B). As such, the same loading rate is distributed among more MUC16-E-selectin than PODXL-E-selectin bonds of similar tensile strength for individual bonds, thereby supporting slower MUC16-dependent rolling at each prescribed shear stress level (Figure 3.6B). On L-selectin surfaces, both ligands displayed a rather transient rolling behavior, with PODXL-coated microspheres rolling significantly slower than MUC16-coated microspheres at lower (0.5 and 1 dyn/cm^2) but not at the higher shear stress of 2 dyn/cm^2 (Figure 3.6C). In the low shear regime (0.5 dyn/cm^2), both MUC16- and PODXL- coated microspheres tether to L-selectin with an identical bond number (Figure 3.5C, D). Thus, the slower rolling velocity mediated by PODXL is attributed to lower k_{off}° and higher tensile strength of PODXL-L-selectin interaction (Table 3.4). At the higher shear stress level of 2 dyn/cm^2, the difference in rolling velocity is no longer statistically significant because the differences in the kinetic and micromechanical properties of single bonds between PODXL versus MUC16 with E-selectin are masked by the higher number of MUC16-L-selectin bonds (Figure 3.5C,D) required to support tethering.

3.4. Discussion

The adhesive interactions between selectins on host cells and their respective ligands expressed on tumor cells are known to facilitate tumor cell arrest in the microvasculature and promote cancer metastasis (31, 133). While the biophysics of leukocyte binding to selectins has been well studied (43, 131, 147), little is known about the mechanics of selectin-mediated tumor cell adhesion. As circulating tumor cells contact the blood vessel wall, selectin-mediated interactions support rolling and facilitate subsequent firm adhesion, making them a vital part of the metastatic cascade. Cell adhesion relies on the balance between the adhesive forces of receptor-ligand pairs and disruptive hydrodynamic forces (148). We herein employed force spectroscopy and a microfluidic assay in conjunction with a mathematical model to delineate the contributions of the single-molecule kinetic and micromechanical properties of selectin-ligand bonds as well as the number of selectin-ligand bonds to pancreatic cancer cell tethering and rolling in shear flow. A quantitative analysis of receptor-ligand binding kinetics of *functional* selectin ligands expressed by metastatic tumor cells, such as MUC16 and PODXL, in the presence of shear flow will further the understanding of the metastatic process.

P-selectin glycoprotein-1 (PSGL-1) expressed by leukocytes is a known ligand of P-, E- and L-selectin. PSGL-1-selectin interactions have been extensively studied using diverse biophysical assays (43, 45, 144, 147, 149-152). Although the unstressed off-rate, k_{off}°, is similar for PSGL-1, MUC16 and PODXL binding to E-selectin, the PSGL1-E-selectin bond is markedly stronger than MUC16-, PODXL- E-selectin bonds, as evidenced by its lower reactive compliance, x_β, and higher tensile strength (Table 3.4) (140). Similarly, the PSGL-1-L-selectin bond displays a lower reactive compliance and higher rupture force than MUC16-, PODXL- L-selectin bonds (Table 3.4). As expected, the single-molecule bond of E- or L-selectin with monovalent sLe^x is markedly weaker than all aforementioned respective ligand-selectin pairs (Table 3.4) (153).

Cell binding to a substrate occurs when an individual bond or a cluster of bonds are formed under flow that are capable of withstanding the dispersive hydrodynamic forces, thereby tethering the cell to the surface. Because the single bonds between MUC16 or PODXL with E-selectin are stronger than the respective ones with L-selectin (Table 3.1), fewer bonds are required to mediate microsphere tethering to E-selectin than L-selectin in shear flow. As such, the binding frequency of MUC16- or PODXL- coated microspheres is higher for E-selectin than L-selectin at equivalent site densities and shear stresses. Along these lines, the critical patch length is lower for E-selectin than L-selectin. It is noteworthy that while MUC16 and PODXL bonds with E-selectin have similar tensile strengths, a shorter critical patch length is required for the PODXL-E-selectin interaction. This is due to the lower number of bonds needed to tether PODXL- versus MUC16- coated microspheres to an E-selectin-coated surface (Figure 3.5A,B) coupled with its higher affinity (Table 3.3). Also, the lower number of bonds required to mediate tethering of PSGL-1-expressing cells to L-selectin coupled with its higher tensile strength relative to MUC16- or PODXL-L-selectin bond can help explain the markedly higher binding frequency of PSGL-1-expressing cells to L-selectin micropatches (51).

A plateau in the extent of PODXL- and MUC16- dependent tethering to E-selectin is observed for patch lengths longer than 40 and 80 μm, respectively, where a further increase in patch length no longer increases binding. The plateau initiation point was found to directly relate to the critical patch length and the apparent multiple bond off-rate in the presence of force ($k_{off,n}$), which considers the unstressed off-rate and reactive compliance of the single bond ($\overset{\circ}{k}_{off}$ and x_β) as well as the number of bonds formed (n), and the hydrodynamic force on the microsphere (f) (50). As shown in Eqn. 1, we assumed that at the initiation of microsphere tethering, the hydrodynamic force is distributed evenly among every bond, and when n-bonds break serially they do so in a stepwise fashion such that the force is redistributed among the remaining bond(s).

$$k_{off,n} = \frac{1}{\sum_{i=1}^{n} \frac{1}{k_{off,i}}} = \frac{1}{\sum_{i=1}^{n} \frac{1}{k_{off}^{o} \exp\left(\frac{x_\beta f}{i k_B T}\right)}} \qquad \text{Equation 3.4.1}$$

The microsphere is assumed to dissociate when all bonds have ruptured, and interaction time is calculated by summing the total time needed to dissociate all bonds. Here, higher values for the apparent $k_{off,n}$ can result from either decreased bond strength or the formation of fewer bonds. In the case of E-selectin binding, single-bond tensile strength is similar for both PODXL and MUC16, and the faster plateauing of the PODXL-E-selectin interaction results from the lower bond number required for tethering.

Several studies have reported slower rolling on E-selectin versus L-selectin due to the lower unstressed off-rate $\overset{\circ}{k}_{off}$ associated with E-selectin binding (150, 154). We also see this trend; however, it appears that the number of bonds needed for adhesion in shear flow also plays an important role in regulating the rolling velocities of MUC16- and PODXL- coated microspheres on E- and L-selectin. Although the $\overset{\circ}{k}_{off}$ of single bonds between MUC16 and PODXL with E-selectin are similar, we observed significant differences in their respective rolling velocities. As determined by fitting the multi-bond model to the experimental data, an additional bond is needed to initiate MUC16-E-selectin compared to PODXL-E-selectin binding (Figure 3.5A, B). As such, the apparent $k_{off,n}$ is lower for MUC16-E-selectin at all shear stress levels. If we consider microsphere rolling to consist of two steps: (i) the microsphere moving either at the hydrodynamic velocity ($V=U_d$) or (ii) it is bound (with $V=0$), this result makes sense. A larger number of bonds must be broken to release the microsphere from the surface; the presence of more bonds allows the microsphere to spend more time in the bound state, thereby slowing the rolling velocity provided that the on-rate is significantly fast. This behavior is also noted for L-selectin binding where at 0.5 dyn/cm^2 both MUC16- and PODXL-coated microspheres require 5 bonds for binding, and rolling is k_{off}° dependent. At the shear stress level of 2 dyn/cm^2, the increased number of bonds needed for MUC16-L-selectin tethering acts as a natural break, slowing its rolling to similar levels to those of PODXL-L-selectin indicating that bond clusters may play a critical role in cell rolling stability (155, 156). Differences in rolling velocities between E- and L-selectin pairs likely also result from differences in bond tensile strength that has been reported to influence rolling (45, 140). Therefore, the interplay of the tensile strength, k_{off}°, and bond number regulates the rolling velocities of MUC16- and PODXL- coated microspheres on E- and L-selectins. In addition to these parameters, cell deformation affects rolling in shear flow (157).

MUC16 and PODXL have been identified as *functional* E- and L-selectins ligands that are overexpressed in metastatic pancreatic cancer cells (52, 53). In this study, we utilized the combination of single- molecule bond characterization and microfluidic assays coupled to mathematical model to characterize ligand-dependent tethering and rolling in physiologically relevant flow conditions. We found that the single-molecule kinetic and micromechanical properties and the number of bonds needed for tethering predict the binding interactions and rolling of MUC16- and PODXL-coated microspheres on E-/L- selectin coated surfaces. This integrated approach contributes to a better understanding of how MUC16 and PODXL bind to E-/L-selectins in the presence of hydrodynamic shear, which can lead to improved diagnostic assays and to the prevention of the metastatic spread of pancreatic tumor cells.

3.5 Tables and Figures

Interaction	$k_{off}^{\circ}\ (s^{-1})$	x_{β} (nm)
MUC16–E-selectin	0.26 ± 0.08	0.34 ± 0.02
MUC16–L-selectin	0.82 ± 0.04	0.36 ± 0.01
PODXL–E-selectin	0.33 ± 0.05	0.33 ± 0.01
PODXL–L-selectin	0.49 ± 0.04	0.35 ± 0.02

Table 3. 1 Bell model parameters for PODXL and MUC16–E/L-selectin interactions.

Bell model parameters were determined using a least-squares fit to the plot of linear region of rupture force against the logarithm of loading rate. Data are shown as the mean ± S.D.

	MUC16-E-selectin and (L-selectin)			PODXL-E-selectin and (L-selectin)		
	Selectin density (sites/μm^2)					
Shear tress (dyn cm^{-2})	1800	3000	4800	1800	3000	4800
2	120 (NB)	80 (NB)	80 (NB)	160 (NB)	40 (NB)	40 (NB)
1	40 (NB)	40 (NB)	20 (80)	40 (NB)	20 (NB)	20 (80)
0.5	40 (80)	20 (80)	10 (40)	10 (80)	10 (80)	10 (40)

Table 3. 2 Critical patch length of PODXL and MUC16–E/L-selectin interactions.

NB indicates no binding. The critical patch length of selectin is defined as the minimum patch length required for MUC16 or PODXL coated microshperes to initiate 2% binding at a given shear stress and selectin site density. The numbers inside the parentheses indicate the critical patch length for L-selectin.

Binding pair	$A_cM_rM_lK_{on}$ (s^{-1})		
	Shear stress (dyn/cm^2)		
	0.5	1	2
MUC16-E-selectin	10.1	42.6	151.7
MUC16-L-selectin	16.1	47.1	124.8
PODXL-E-selectin	26.3	105.1	300.2
PODXL-L-selectin	8.6	38.1	115.7

Table 3. 3 $A_cM_rM_lK_{on}$ for MUC16- and PODXL- coated microspheres tethering on E-/L-selectin coated surface as predicted by the multi-bond model.

The multi-bond model was fitted to the experimental data and optimized for both the number of bonds needed to achieve tethering and lumped affinity ($A_cM_rM_lK_{on}$) for MUC16- and PODXL-coated microspheres tethering to 3000 sites/μm^2 E- or L-selectin coated patches.

Binding pair	k_{off}° (s^{-1})	x_{β} (nm)	Rupture force @1000 pN/s (pN)
MUC16–E-selectin	0.26 ± 0.08	0.34 ± 0.02	71
PODXL–E-selectin	0.33 ± 0.05	0.33 ± 0.01	69
PMN (PSGL-1)–E-selectin*	0.31 ± 0.06	0.12 ± 0.01	156
sLeX–E-selectin§	0.30	0.5	48
MUC16–L-selectin	0.82 ± 0.04	0.36 ± 0.01	56
PODXL–L-selectin	0.49 ± 0.04	0.35 ± 0.02	62
PMN (PSGL-1)–L-selectin*	0.85 ± 0.10	0.17 ± 0.01	93
sLeX–L-selectin§	6	0.45	29

Table 3. 4 Comparison of the binding parameters for ligand - E/L-selectin pairs.

*Data presented from Hanley *et al.* [42] with Bell model kinetic constants for linear region (100-10,000 pN/s) and rupture forces estimated from provided figures. §Data presented from Zhang *et al.* [43] with Bell model kinetic constants for linear region (100-10,000 pN/s) and rupture forces estimated from provided figures. Where appropriate, data shown as the mean ± S.D.

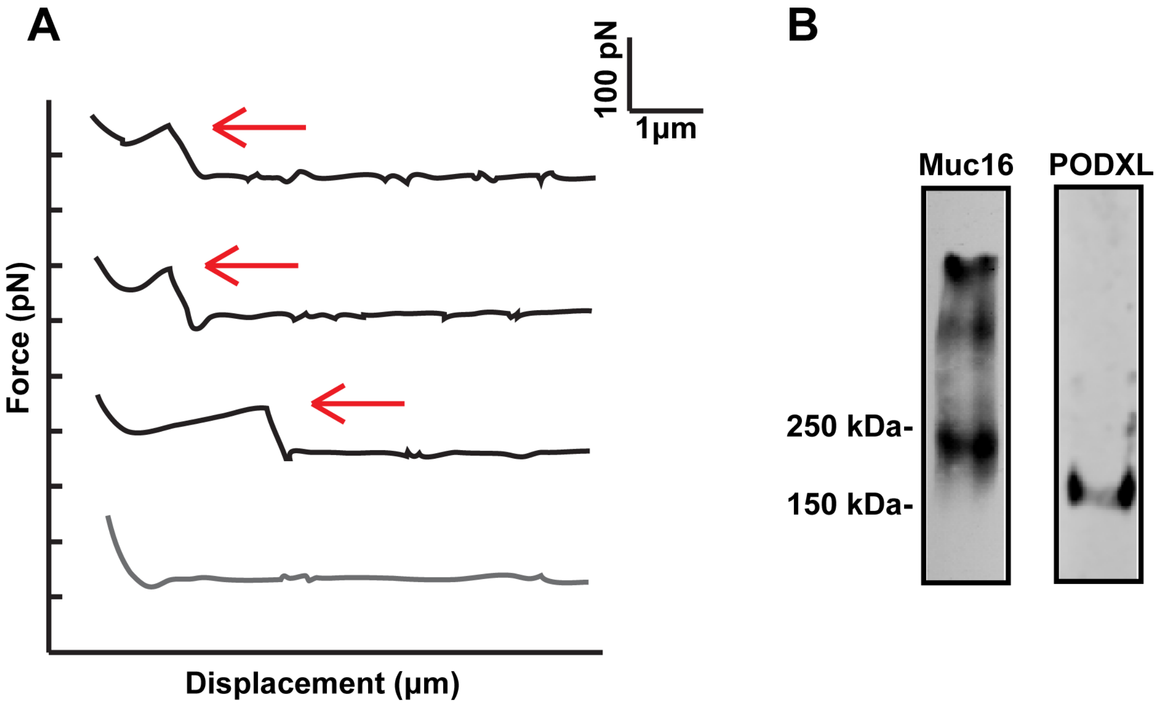

Figure 3. 1 Single molecule force spectroscopy Force Displacement traces and western blots image.

(A) Typical force-displacement traces acquired from force spectroscopy experiments where an E/L-selectin fuctionalized cantilever was brought in contact hundreds of times with either immunopurified PODXL or MUC16 incorporated in a lipid vesicle deposited on a PEI-cushioned glass slide. Red arrows indicate rupture events with the loading rate estimated based on the slope of the linear ramping in force immediately before bond rupture. **(B)** MUC16 and PODXL were immunopurified from SW1990 cells and were subjected to SDS-PAGE under reducing conditions followed by immunoblotting with an anti-PODXL mAb (3D3) or anti-Muc16 mAb (M11).

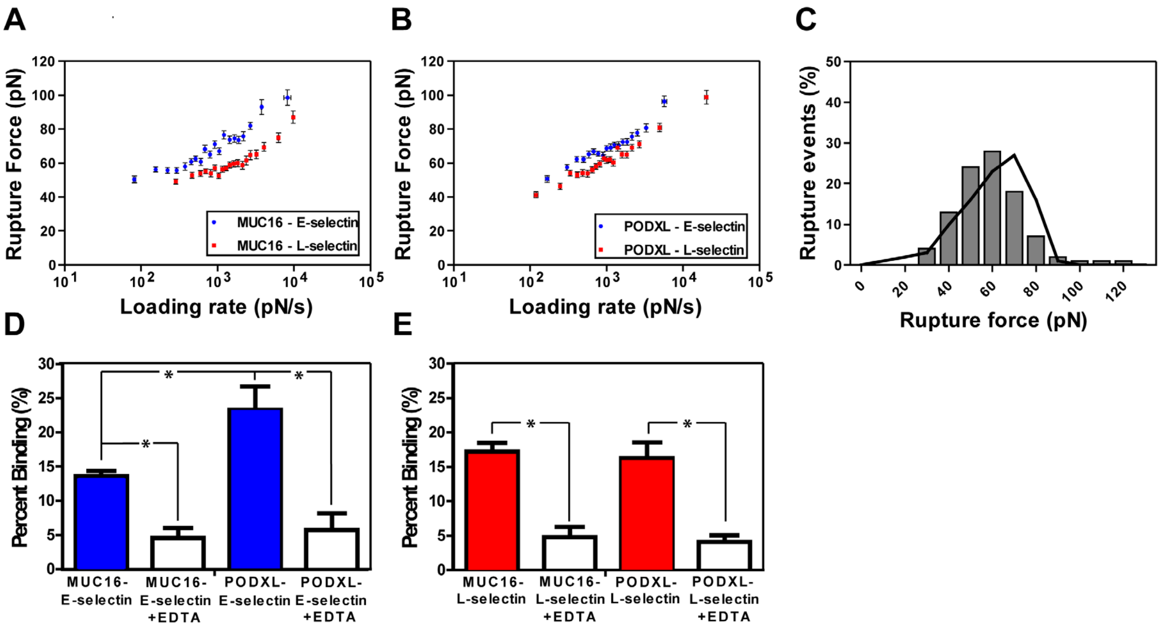

Figure 3. 2 Micromechanical properties of immunopurified MUC16/PODXL binding to E/L-selectin using single molecule force spectroscopy.

Rupture force as a function of loading rate for immunopurified **(A)** MUC16-E/L-selectin and **(B)** PODXL-E/L-selectin interaction. Data represent the mean ± S.E.M. of 3-4 experiments run for each binding pair. Least-squares fitting of the Bell model were used to determine kinetic parameters. **(C)** Rupture force distribution was obtained both experimentally (bars) and computationally through Monte-Carlo simulations (line) based on Bell model kinetic parameters for immunopurified PODXL-E-selectin binding. **(D-E)** Frequency of binding between immunopurified MUC16 and PODXL with E-selectin and L-selectin in the absence and presence of the divalent cation chelator EDTA. Tips coated with 10 μg/ml E-/L-selectin were brought in contact with either MUC16 or PODXL incorporated lipid bilayers. The frequency of binding was measured in with and without the presence of 10 mM EDTA. Data represent the mean ± S.E.M. of 3-4 independent experiments. *P< 0.05.

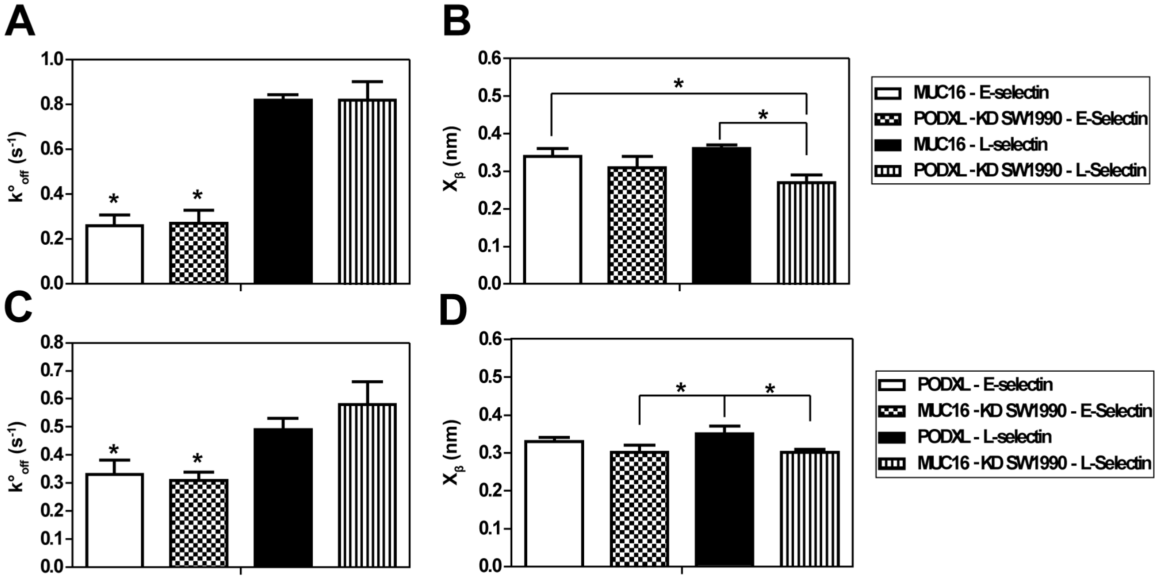

Figure 3. 3 Bell Model kinetic properties of protein-protein and cell-protein interactions.

(A, C) Unstressed off-rate (s^{-1}) and **(B, D)** reactive compliance (nm) for MUC16 and PODXL interactions with E/L-selectin using a range of retraction velocities (5-25μm/s). Data represent mean ± S.D. of 3-5 independent experiments which each had at least 1,250 approach/retract cycles. Cantilever tips coated with E/L-selectin were brought in contact with immunopurified MUC16 or PODXL incorporated lipid bilayers or MUC16-expressing (PODXL-KD) or PODXL-expressing (MUC16-KD) SW1990 cells. *P< 0.05 with respect to both MUC16-L-selectin and PODXL-KD SW1990-L-selectin in (A). *P< 0.05 with respect to both PODXL-L-selectin and MUC16-KD SW1990-L-selectin interactions in (C). *P< 0.05 with respect to the indicated interactions (B, D).

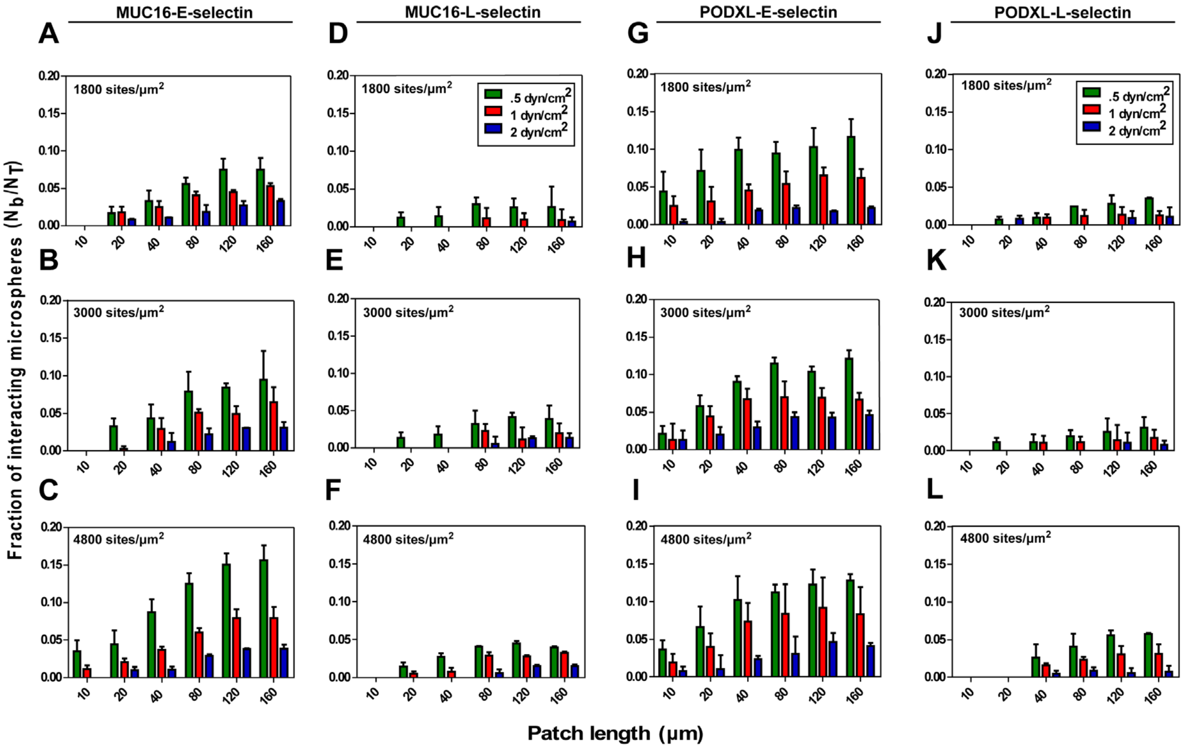

Figure 3. 4 Fraction of interacting microspheres with E/L-selectin coated patches at designated shear stresses.

Microspheres ($2x10^6$/ml) coated with either MUC16 or PODXL at equivalent site densities flowed at prescribed shear stresses over glass surfaces containing patches coated with three site densities of either E- or L-selectin. The number of MUC16 **(A-F)** or PODXL **(G-L)** coated microspheres interacting with each patch was counted and normalized based on the microsphere flux over each patch. Data represent the fraction of interacting microspheres (N_b/N_T) mean ± S.E.M. of at least three experiments.

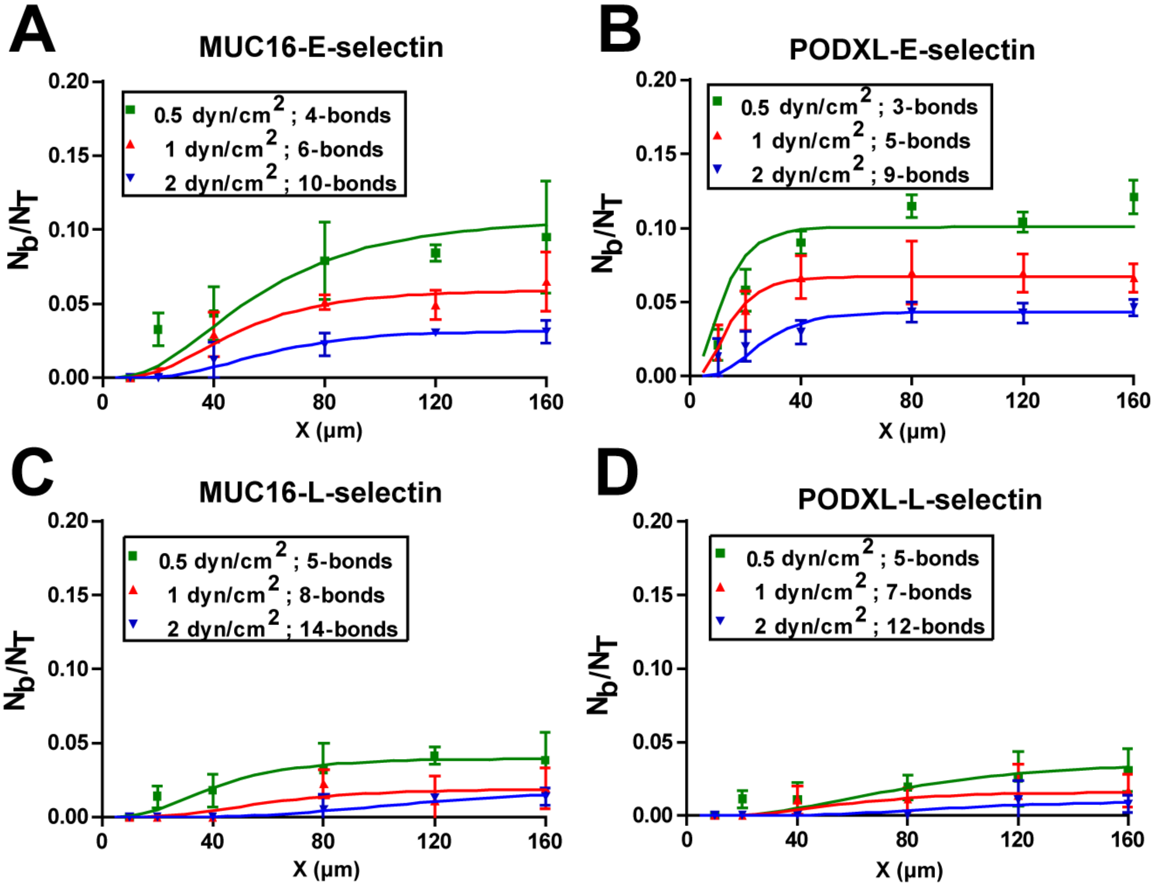

Figure 3. 5 Fitting of the multi-bond model to the experimental data.

Immunopurified MUC16 **(A, C)** or PODXL **(B, D)** coated microspheres flowed over glass surfaces patterned with 3000 sites/μm^2 E-selectin **(A, B)** or L-selectin **(C, D)** coated patches of varying lengths. The multi-bond model was fitted to the experimental data (points) and optimized for both $A_cM_rM_lK_{on}$ and n-bonds, with the solid lines representing the model prediction.

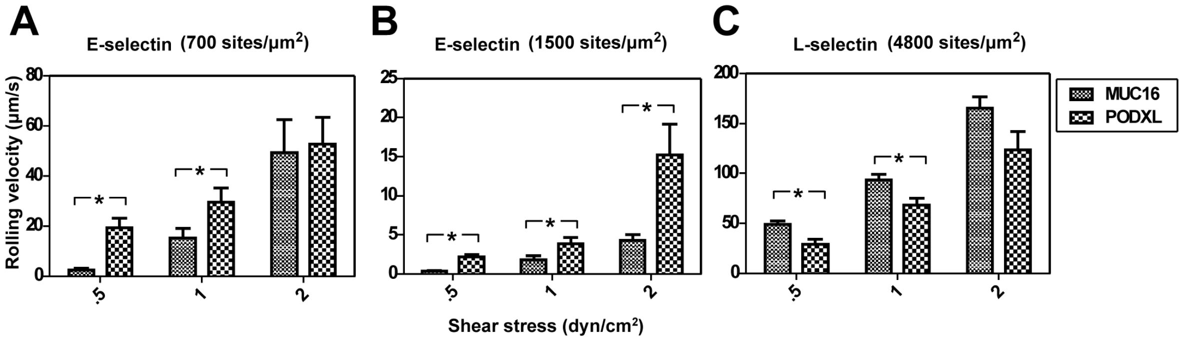

Figure 3.6 Average rolling velocities of MUC16- and PODXL- coated microspheres on E/L-selectin.

Average rolling velocities (µm/s) of microspheres (2x10^6/ml) coated with either MUC16 or PODXL at equivalent site densities on immobilized E-selectin **(A, B)** or L-selectin **(C)**. Data were recorded at prescribed wall shear stresses and represent the mean ± S.E.M. of at least 3 independent experiments. *$P < 0.05$.

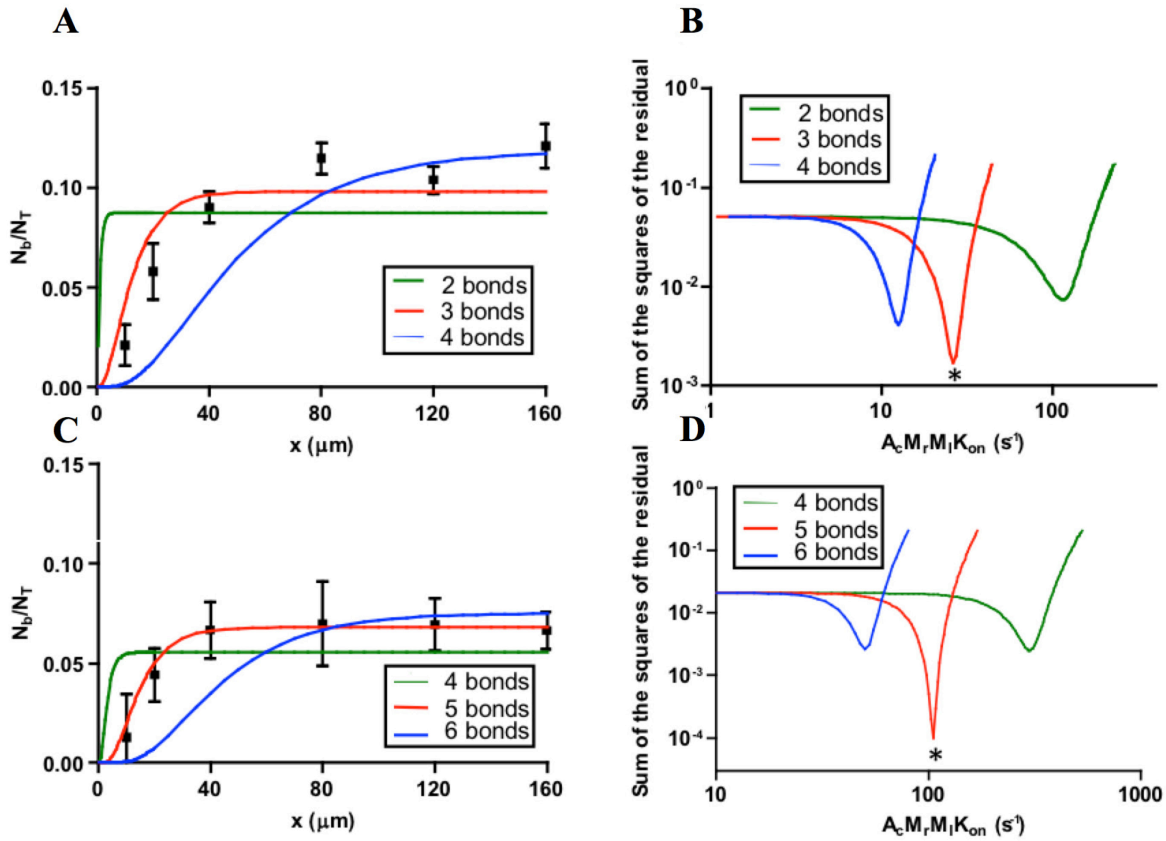

Figure 3.7 The multi-bond model determines the number of bonds and lumped affinity ($A_c m_r m_l k_{on}$) needed to mediate PODXL-coated microsphere tethering on E-selectin in shear flow.

Fitting of the multi-bond model to experimental data for PODXL-coated microspheres interacting with 3000 sites/μm^2 E-selectin at 0.5 dyn/cm^2 **(A)** and at 1 dyn/cm^2 **(C)**. The sum of squares of residual **(B)** and **(D)** was calculated by fitting the model to the experimental data shown in **(A)** and **(C)**, respectively. The lumped binding affinity ($A_c m_r m_l k_{on}$) for the optimal fit is marked by (*) on **(B)** and **(D)**.

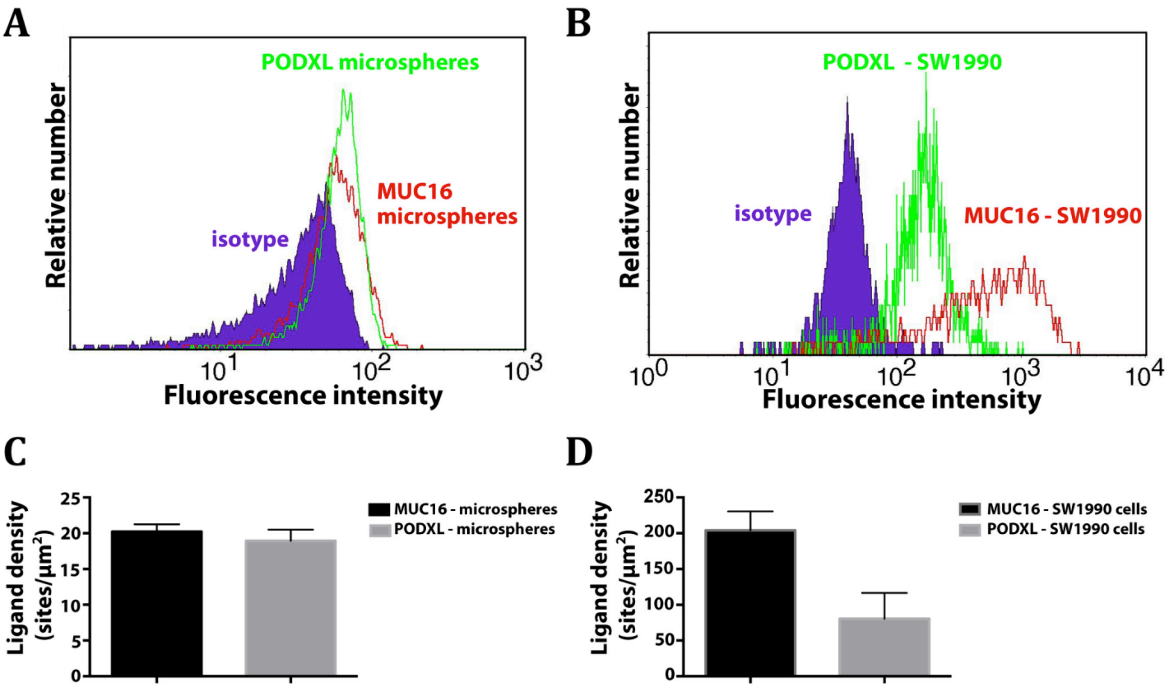

Figure 3.8 PODXL and MUC16 site density on microspheres and SW1990 cells as determined by quantitative flow cytometry.

Representative flow cytometric histograms of MUC16 and PODXL on **(A)** protein-coated microspheres and **(B)** SW1990 pancreatic cancer cells. Microspheres and SW1990 cells were stained by indirect single-color immunofluorescence using anti-PODXL or anti-MUC16 mAbs or their respective isotype control antibodies (purple). Using the Quantum FITC-5 MESF Kit in conjunction with Simply Cellular anti-mouse IgG microspheres (Bangs Laboratories, Fisher, IN), the site density of MUC16 and PODXL on **(C)** protein-coated microspheres and **(D)** SW1990 cells were calculated. Data represent the mean ± S.E.M. of at least four independent experiments.

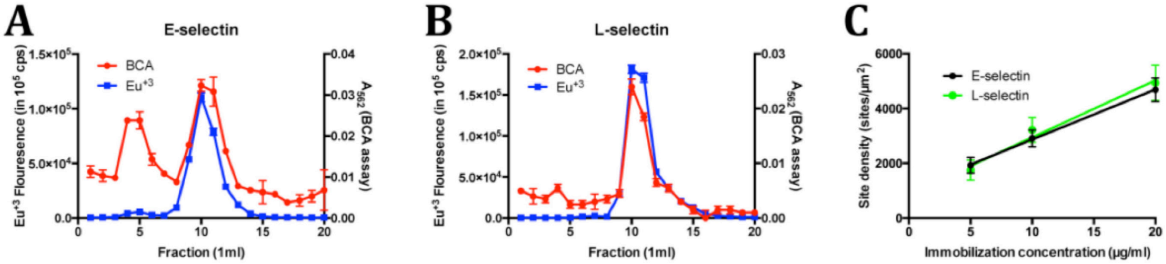

Figure 3.9 Determination of E- and L- selectin surface site density.

(A) E-selectin or **(B)** L-selectin was conjugated with europium (Eu^{+3}) using the DELFIA Eu-Labelling Kit and purified via gel filtration chromatography. Elution fractions positive for both protein (absorbance at 562 nm following BCA assay) and Eu^{+3} content (high time-resolved fluorescence in RFU) were pooled and concentrated. **(C)** The purified europium-conjugated E- or L-selectin was used to determine the surface site density. Data represent the mean ± S.E.M. of at least four independent experiments.

Chapter 4

E-SELECTIN MEDIATED ROLLING INCREASES PANCREATIC TUMOR CELL ADHESION TO HYALURONIC ACID

Tumor cell extravasation is a complex process, initiated when cells roll and arrest on the vessel wall through the formation of specific bonds. The strength, availability, and number of receptor-ligand bonds regulate the rate which tumor cells tether, roll and adhere to host cells. While we have recently explored the mechanics of selectin-mediated rolling pertinent to cancer metastasis, little is known regarding how cell rolling on selectins affects adhesion to a second protein with differing kinetic properties. In this regard we sought to evaluate the critical parameters of the pancreatic tumor adhesion to hyaluronic acid mediated by rolling on E-selectin in physiologically relevant flow. We utilized a microfluidic assay and multicomponent protein patterning to evaluate E-selectin and HA binding as a function of fluid shear stress, contact time and protein distance. We show that tumor cells rolling on E-selectin were ~40X more likely to bind to HA than non-rolling cells at both low and high shear stresses. Further, the ligand-E-selectin interaction initiates adhesion to HA in a twofold manner, both physically slowing cells and allowing cells to orient close to the surface and increasing the on rate of adhesion. Understanding the critical parameters tumor cell adhesion in physiologically relevant shear stresses is vital for production of improved diagnostic assays and to better understand the metastatic spread of pancreatic tumor cells.

4.1. Introduction

Metastasis is a multistep process, in which cancer cells migrate from the primary tumor to the circulatory system where they extensively interact with the endothelial wall before extravasating and colonizing a distal organ. Tumor cell extravasation from the vasculature requires cells to first to roll and then arrest on the vessel wall through the formation of specific bonds. The probability of cell binding depends on the frequency of collision between membrane-bound receptors and endothelial ligands, the strength of these bonds and the length of time the cell interacts with the ligand presenting region (51, 158).

E-selectin and hyaluronic acid (HA) play a pivotal role in the cell-cell interactions that are pertinent to cancer cell rolling and arrest. E-selectin is expressed on activated vascular endothelial cells and promotes the tethering and rolling of malignant cells (31, 132, 133). PODXL and MUC16 are the major functional ligands of E-selectin that are expressed on pancreatic tumor cells (52, 53) and both MUC16-, PODXL-E-selectin bonds have been demonstrated to facilitate rolling interactions with E-selectin at high shear stresses, and at low ligand and receptor site densities (158). HA is a major component of the extracellular matrix in most tissue, and is upregulated on the surface of endothelial cells activated with an inflammatory stimuli (74, 75). CD44 is expressed on Pa03c pancreatic cancer cells (Figure 4.7), is the major cell ligand for hyaluronic acid (HA), (67-69) and has been implicated in pancreatic cancer metastasis (159). HA binding to CD44 has been indicated to increase cancer metastasis and invasion (76, 77) and the HA-CD44 bond has been found to enable slow cell rolling (under 5 μm/s) (67, 78, 79) and in some instances firm adhesion at low shear stresses (78, 79).

To explore how rolling on E-selectin facilitates pancreatic cell adhesion to HA we utilized multicomponent micropatterning, to deliver two proteins in geometrically defined patterns on a glass substrate. Multicomponent micropatterning has been utilized to measure cell adhesion (160), cell binding in shear flow (161, 162) and to separate circulating tumor cells from leukocytes and other cells types (161, 162). However limitations exist, typically only simple geometries can be patterned with a multicomponent system (161, 162), or they rely on chemistry to achieve the desired pattern (161). Our system uses a simple flow based coating method (163) to achieve geometrically complex patterns in close proximity to one another. This allowed us to pattern both E-selectin and HA, 30 μm apart in complex geometric patterns and observe how rolling on E-selectin pancreatic tumor cell adhesion with HA.

Here we show that rolling on E-selectin promotes pancreatic tumor cell adhesion to HA. Rolling cells were ~40X more likely to bind to HA than non-rolling cells and where more likely to adhere to HA at higher shear stresses that non-rolling cells. Rolling on E-selectin facilitates binding with HA even at E-selectin patch lengths under 40 μm and on HA patches as low as 10 μm. Knockdown of the major E-selectin receptor PODXL attenuates rolling on E-selectin but does not decrease the rate of adhesion on HA once cells have rolled. This approach uncovers the physical interdependence of these bonds and indicates how selectin mediated tumor cell rolling can initiate adhesion with a secondary ligand, which can be utilized to improved diagnostic assays and better understand the metastatic spread of pancreatic tumor cells.

4.2. Materials and Methods

4.2.1. Cell culture

Human pancreatic adenocarcinoma Pa03c cells were obtained from the American Type Culture Collection (Manassas, VA). Pa03c PODXL-KD cells were generated as previously described (52, 53). All Pa03c cells were cultured in DMEM with 10% FBS with 700 µg/ml G418 and 0.5 µg/ml puromycin added to the PODXL-KD and control media, respectively (Life Technologies, Carlsbad, CA).

4.2.2 Cell lysate and western blot analysis

Whole cell lysate of Pa03c cells was generated as previously described (52, 53). Lysates were separated by a 3–8% Tris-acetate SDS-PAGE gel. Proteins were then transferred to an Immuno-blot PVDF membrane and blocked for 30 min in blocking buffer. Membranes were stained with anti-CD44 mAb (2C5) and rinsed with TBS/0.1% Tween 20, before incubation with horseradish peroxidase-conjugated secondary antibody. SuperSignal West Pico chemiluminescent substrate was then used to develop the immunoblot.

4.2.3 Pattern device fabrication

The microfluidic device used for patterning glass slides with E-selectin and HA was fabricated using standard practices and our previously established methodology (51). The PDMS pattern features channels with height 10 µm that open to the triangular (bottom) or rectangular (top) regions used to pattern E-selectin and HA respectively

(Figure 4.1A). The triangular (E-selectin) regions have a 200 μm base and 160 μm width while the four rectangular regions (HA) have a 10, 40, 80 and 160 μm width and 200 μm base. The triangular and rectangular regions align such that a cell passing over one region will pass over the second region in succession. 3mm diameter inlet and outlet holes were punched in both the top and bottom channels. The gap between the two regions was set to 30, 60 and 120 μm.

4.2.4 E-selectin and HA patterning

A pre-cleaned glass slide and the PDMS pattern device were plasma treated for 2 minutes. Following cleaning the two were adhered together. HA at 50 μg/ml was added to the inlet of the top channel and PBS was added to the inlet of the bottom channel. The devices were incubated overnight at 4°C. Next, the HA was removed and replaced with PBS. Concurrently the PBS in the bottom channel was removed and FITC-conjugated goat anti-human IgG Fc fragment specific antibody (Sigma, St. Louis, MO) was added to the inlet of the bottom channel. The antibody was removed and washed with PBS before adding recombinant E-selectin Fc chimera at a concentration of 10 μg/ml. Following E-selectin incubation, the PDMS device was then removed, the slide was washed and blocked in 1% BSA in D-PBS for at least 1 hour prior to the running of experiments

4.2.5 Microfluidic flow based adhesion device fabrication

The microfluidic device was fabricated using standard practices using a previously established methodology (51). The dimensions of the device channel used in this experiment were 2 cm × 1000 μm × 22.5 μm (length × width × height).

4.2.6 Microfluidic flow-based adhesion and rolling assays

The microfluidic flowchamber was cleaned in ethanol and dried with air before assembly on top of the patterned glass slide. Via a pipette, 0.1% BSA in PBS was introduced into the channel and allowed to flow to equilibrate the device. The device was placed on a microscope stage and 100 µl of Pa03c-SC or PODXL-KD cells suspended in 0.1% BSA in PBS ($1\text{x}10^6$ cells/ml) were added to the inlet channel and allowed to flow via gravity. A 10x field of view was used and each perfusion lasted at least 3 min.

4.2.7 Data analysis

To track the cells over the course of the 3 minute video, we utilized the existing code package produced by Eric M. Furst from the University of Delaware for cell tracking. We set the maximum cell radii to a value of 21 µm, and the size of a pixel in the x and y dimensions to 1.32 and 1.51 µm/pixel, respectively. The output is a matrix of cell position and time data which was further processed. We then excluded incomplete tracks, which were not bright enough to pass entirely through the frame and clumped cells, which enter the frame within 2 radii of one another. By hand we excluded regions of the video which incoming cells contact previously bound cells on the device.

4.2.8 Data processing

Using Matlab we then analyzed the fluorescent images of the patterned surface to identify the boundaries of both the E-selectin and HA regions. The E-selectin region was then separated into ten sections of increasing patch length ranging from 10-160 μm. The program then analyzes each cell track with respect to these regions and indicates: the binned position of the cell, if the cell binds in either region (rolling or firm adhesion), the overall velocity of the cell, and the cell velocity in each region and the hydrodynamic velocity of all non-interacting cells. Interacting cells are identified if they are in a binding region (E-selectin or HA) and have an instantaneous velocity less than 50% of the bulk cell instantaneous hydrodynamic velocity for at least five frames (.17 seconds). Cells adhering to HA were also confirmed via a manual inspection. As a result of this process, data can be compiled easily for a large number of cells and different combinations of rolling and firm adhesion parameters can be easily analyzed.

4.2.9 Data acquisition validation

To validate the automated results, all the cells in three selected videos were both manually and automatically tracked. Both of the data sets were run through data processing and the results were compared. Matched cell tracks were then compared using the Bland Altman test to compare the two measurement methods.

4.2.10 Mathematical model of 2-D selectin-mediated cell adhesion on micropatches

The model for selectin binding to 2-D micropatches utilized here was discussed in detail previously (51, 158). The calculations consider all bonds to break simultaneously

(50). The f/τ was determined to be 689 pN/dyn-cm^2 assuming the cell is more like a neutrophil than a bead and considering the cell radius of 10um (131). The kinetic constants for the CD44v-HA bond used were k_{off}° = .005 s^{-1} and x_{β} = .59 nm, determined via single molecule force spectroscopy in a previous work (67).

4.2.11 Statistical analysis

Data are expressed as means ± S.E.M. or 95% confidence intervals of at least 3 independent experiments. Statistical significance of differences between means was determined by one-way analysis of variance followed by the either the Tukey or Sidak test for multiple comparisons, the student's T test, or the two-proportion Z test where appropriate.

4.3. Results

4.3.1 Microfluidic device design and cell tracking

Experiments were performed with Pa03c pancreatic cancer cells, tracking their binding as they encountered patches of E-selectin (rolling) and HA (slow rolling and firm adhesion). In brief using standard microfabrication principles (163-165) we patterned a glass slide with E-selectin patches of length 10-160 μm and hyaluronic acid (HA) patches with lengths of 10, 40, 80 and 160 μm in geometrically defined regions with a gap distance between the two regions of 30, 60 and 120 μm (Figure 4.1 A-C). Using a microfluidic chamber, MUC16/PODXL and CD44v expressing metastatic pancreatic cancer cells (Pa03c) were then perfused over the two regions and all cells were tracked using a modified code package produced by Eric M. Furst (University of Delaware). Using a custom Matlab program, we identified cells as they flowed over the E-selectin, gap, and HA regions. As cells enter the E-selectin region they are separated into ten bins corresponding to the average length of E-selectin patch the cells encounter (10-160 μm). Next, the gap distance and HA patch length that the cell encounters is also recorded. For example, a cell can pass over the 160 μm E-selectin region, the 30 μm gap and the 40 μm HA region. Each cell track is then analyzed with respect to these regions and the cell position, velocity, and binding in either the E-selectin and/or HA regions were identified.

To confirm the validity of this method used to track cells, our automated tracking system was compared against manually tracking cells and no differences cell position or cell speed was found for either the E-selectin, or HA regions (Figure 4.8A, C and E). Minor differences were found using the Bland-Altman analysis to compare the two analysis methodologies (Figure 4.8B, D and F). Overall given the minor differences of these measurements, the similarities of the bulk populations and the similar percent of rolling cells determined by both methodologies (Figure 4.8G) we have confidence that using the automated tracking is a reliable methodology to track cells in this system.

4.3.2 Cell rolling on E-selectin mediates adhesion to HA

Pa03c cells were tracked as they passed over the E-selectin region, the gap region and HA region respectively. Cells either interacted with E-selectin/HA or passed over these regions without binding. Four outcomes were possible, a cell could bind only to either the E-selectin or HA regions, to both the E-selectin and HA regions, or to neither of the regions. Non-binding cells passed over the patches at the hydrodynamic cell velocity. Cells interacting with E-selectin displayed a clear rolling behavior (Figure 4.1D). The fraction of interacting cells decreased with shear stress and increased with longer E-selectin patch lengths due to increased ligand-selectin contact times (Figure 4.2A). These trends are similar to that of MUC16 of PODXL coated microspheres interacting with E-selectin (10 μg/ml) as described in a recent study (158). Cells interacting with E-selectin increase their average speed once they entered the gap region and the HA region as they began to accelerate to the hydrodynamic velocity (Figure 4.9) (166).

After passing over the E-selectin region and the gap, cells encountered hyaluronic acid (HA) patches with lengths of 10, 40 and 160 μm. Binding to HA was prolonged and cells did not transiently roll but rather adhered for times ranging from a half a second to several minutes. In this region, non-rolling cells bind infrequently with hyaluronic acid although binding frequency increases with increasing HA patch lengths (Figure 4.2B). Moreover, HA binding frequency increases significantly when cells first roll on E-selectin (Figure 4.2B). Cells rolling first on E-selectin were ~40x times more likely to bind to HA (HA patch length 40 μm, for both the 30 and 60 μm gaps) and the increased binding was consistent over all HA patch lengths (Figure 4.2B). The 120 μm gap was large enough to disrupt binding of rolling cells as minimal binding to HA was observed.

4.3.3 Cell rolling and cell velocity influences Pa03c cell adhesion to HA

Given the number of cells measured, we were able to assess the binding and speeds of pancreatic tumor cells as they passed over and interacted with the E-selectin and HA regions. Clear trends are formed for the different binding categories when plotting the gap velocity vs. the hydrodynamic velocity for every cell (Figure 4.3 A and B). Non-interacting cells have a gap velocity equal to the hydrodynamic velocity, indicating these cells do not slow down in either pattered region as expected (Figure 4.3B). Non-E-selectin binding yet HA binding cells bind at lower hydrodynamic velocities and have a depressed gap velocity when compared to non-interacting cells (Figure 4.3B). E-selectin binding and non-HA binding cells were observed at lower hydrodynamic velocities and feature a decreased gap velocity compared to non-interacting cells (Figure 4.3B). Both E-selectin and HA binding cells have a gap velocity/hydrodynamic velocity that is significantly decreased when compared to all other binding categories, indicating that these cells slow considerably due to rolling before passing over the HA patches.

We next sought to explore the reasons for increased HA binding of rolling cells. For cells that first rolled on E-selectin, the percentage of HA binding increases with decreasing patch lengths (Figure 4.4A). This counterintuitive result makes sense when examining the gap velocity of rolling cells per E-selectin patch length. As the patch length increases the cell velocity in the gap region increases (Figure 4.4B) because rolling on smaller E-selectin patches must occur immediately before the gap while cells rolling on larger patches can break their rolling interaction before the gap and allow the cell to increase speed. Taken together cells which roll on shorter patch lengths of E-selectin (>40 μm) can facilitate adhesion to HA and cell speed is a critical determinant of cell binding to HA.

When binning all rolling and non-rolling cells by shear stress and plotting these values against the HA binding frequency, it is clear that rolling allows cells to bind to HA more frequently and at higher shear stresses when compared to non-rolling cells (Figure 4.4C). This is consistent even at higher shear stresses where the HA binding of non-rolling cells is minimal. Interestingly when plotting HA binding frequency vs. gap velocity, rolling cells are still more likely to bind to HA than non-rolling cells (Figure 4.4D). This indicates that that act of rolling increases the likelihood of firm adhesion compared to non-rolling cell regardless of cell speed in the gap before the HA region. Further both non-rolling and rolling cells bind more frequently to HA at lower gap velocities again indicating the importance of cell speed in HA binding.

4.3.4 PODXL-KD attenuates rolling on E-selectin but does not affect binding with HA once cells have rolled

We then looked to observe the effect of knocking down the major E-selectin cell receptor PODXL on cell rolling on E-selectin and adhesion to HA. In this regard we knocked down PODXL from the surface of Pa03c cells and perfused these cells over the E-selectin and HA patches. We found that PODXL-KD Pa03c cells interacting with E-selectin showed a clear rolling behavior, and that decreased shear stress and longer E-selectin patch lengths increased the fraction of interacting cells. However, PODXL-KD cells interact with E-selectin patches at a lower frequency than control cells at a shear stress of .5 dyn/cm^2 and E-selectin patch lengths longer than 40 μm (Figure 4.5A). Interestingly PODXL-KD cells that first roll on E-selectin, bind to HA at a similar frequency as control cells (Fig. B and C). This is consistent for both the 30 and 60 μm gap lengths and indicates that the depletion of PODXL in Pa03c cells primarily impacts cell rolling but once cells have rolled the frequency of firm adhesion remains unchanged.

4.4. Discussion

Determining the biophysics of pancreatic cancer cell membrane receptors and their ligands relevant to metastasis is critical as it not only improves the understanding of the cell adhesion process but also uncovers critical parameters needed for diagnostic tools and devices (167). In this regard we developed a platform to observe and measure the critical parameters in E-selectin mediated cell adhesion to HA in physiologically relevant flow conditions. Our work utilizes multicomponent protein patterning in geometrically defined patterns with microfluidic channels to profuse cells over ligand-coated patches and measure cell tracks using a custom made cell analysis program. This allows us to measure how cell-ligand interactions with E-selectin influence cell-ligand binding with HA using shear stress, ligand patch length and gap distance as input parameters. The analysis reveals that pancreatic tumor cell rolling on E-selectin increases the frequency of binding to HA ~40X when compared to non-rolling cells. Further, rolling Pa03c cells can facilitate binding to HA at higher shear stresses than non-rolling cells. Rolling on E-selectin facilitates binding with HA even at E-selectin patch lengths under 40 μm and once rolling occurs, cells bind to HA patches as low as 10 μm. The knockdown of the major E-selectin receptor PODXL attenuates rolling on E-selectin but does not decrease the rate of adhesion with HA once cells have rolled. Overall rolling on E-selectin increases cell adhesion with HA and is likely vital to cell-ligand binding observed in the metastatic process.

As we observed in this study and have seen in others, Pa03c cells facilitate rolling on E-selectin and the depletion of PODXL in these cells was found to decrease their binding frequency to E-selectin (52). The PODXL-E-selectin bond facilitates rolling as the bond is sufficiently strong while minimal bonds are required for rolling at low shear stresses (158). The unstressed dissociation constant (k_{off}°) of .33 s^{-1} and reactive compliance (x_{β}) of .33 nm places this interaction in the rolling regime (158). In contrast the CD44v-HA bond is mechanically stronger with a k_{off}° of .005 s^{-1} however this bond is more susceptible to rupture in the presence of force as the x_{β} is .59 nm (67). The lower k_{off}° value likely contributes to the stable slow rolling and firm adhesion observed for CD44 expressing cells binding to HA when compared to ligand-selectin interactions (49, 67, 78, 79, 158). We chose HA as a secondary binding protein because of the faster binding kinetics compared to the PODXL-E-selectin bond. Because of the high bond lifetime of the CD44v-HA bond we would expect Pa03c cells to be capable of firm adhesion if a sufficient number of bonds can form during the interaction time. Likewise, we observed that rolling on E-selectin increases the rate CD44-HA binding at higher shear stresses and that the binding interactions are more stable and long lasting (Figure 4.4C and Figure 4.6A and B). Applying the multi-bond model to the experimental data which solves simultaneously for both lumped binding affinity ($A_cM_rM_lK_{on}$) and the number of bonds to facilitate binding (n-bonds) for the CD44v-HA interaction reveals that both rolling and non-rolling cells bind to HA with 5 bonds, (Figure 4.6C) however cells which roll first on E-selectin have a higher ($A_cM_rM_lK_{on}$) (Figure 4.6D). Given that the receptor and ligand densities (M_rM_l) are the same for both populations this indicates that the 2D binding affinity (A_cK_{on}) is increased for rolling cells and this increase in affinity likely contributes to the increased frequency of binding and more stable adhesion observed by these cells on HA (Figure 4.6A and B).

Cells adhering to HA, which do not first roll on E-selectin, make up a specific subset of the total cell population where adhesion occurs primarily at low shear stresses (Figure 4.3). In fact ~80% of these events occur under .5dyn/cm^2 and it is likely that lower hydrodynamic shear is necessary to facilitate adhesion to HA (78). However, even at lower shear stress the percentage of HA binding cells is low compared to cells which first roll on E-selectin (Figure 4.4C). Cells which roll on E-selectin do so in a shear dependent manner, where increased binding is observed at lower shear stresses and binding decreases with increasing shear stress (Figure 4.10). Of the rolling population, cells bind to HA more frequently at lower shear stresses (4% and 3.8% at .15 and .36 dyn/cm^2 respectively) but also have increased binding at higher shear regimes (3.5% at .71 dyn/cm^2) (Figure 4.4C). This increase in cell adhesion at higher shear stresses, likely results in part, because of the slower speed of the cells immediately before reaching the HA region. We observe that slower cell speeds increase the adhesion frequency with HA of rolling cells (Figure 4.4A and B). However, the cell speed in the gap region is not the only determinant of cell adhesion with HA as the HA binding frequency for cells with similar gap velocities is increased for rolling cells compared to non-rolling cells. Interestingly because both PODXL-KD and PODXL expressing Pa03c cells which first roll on E-selectin bind to HA with similar frequencies we do not believe that this increase in binding is related to a selection of highly expressing PODXL and CD44v cells.

Likely the increase in HA binding of rolling cells is related to hydrodynamic forces that disrupt adhesive forces before the necessary bonds form to initiate firm adhesion. Non-rolling cells can orient anywhere in the 25 μm channel and can have a lower contact area (A_c) with HA as they pass over the ligand coated patches. As a result they bind infrequently to HA and have a lower 2D binding affinity (A_cK_{on}). Rolling cells orient at the ligand interface and therefore can more easily form the CD44v-HA bonds necessary for adhesion (higher A_cK_{on}) (Figure 4.6D). However, when cells pass from the E-selectin region not only does the cell speed increase but hydrodynamic forces can disrupt the cell from the binding interface. This likely results in the lower binding frequency observed with 120 μm gap. Cell rolling on E-selectin likely works to initiate adhesion to HA in a twofold manner, both physically slowing cells and allowing them to orient close to the surface to facilitate stronger adhesion with HA. This allows cells to bind to HA more frequently at higher shear stresses and form more stable interactions with HA, slowing the cell rolling velocity and initiating longer cell-ligand interactions with HA (Figure 4.6A and B).

Here we uncover the physical interdependence of MUC16/PODXL-E-selectin and CD44v-HA bonds and the critical parameters that lead to pancreatic tumor cell adhesion in physiologically relevant shear flow. This approach allows us to determine how tumor cell rolling on E-selectin can initiate adhesion with a secondary ligand, which can be utilized to improved diagnostic assays and better understand the metastatic spread of pancreatic tumor cells.

4.5 Figures

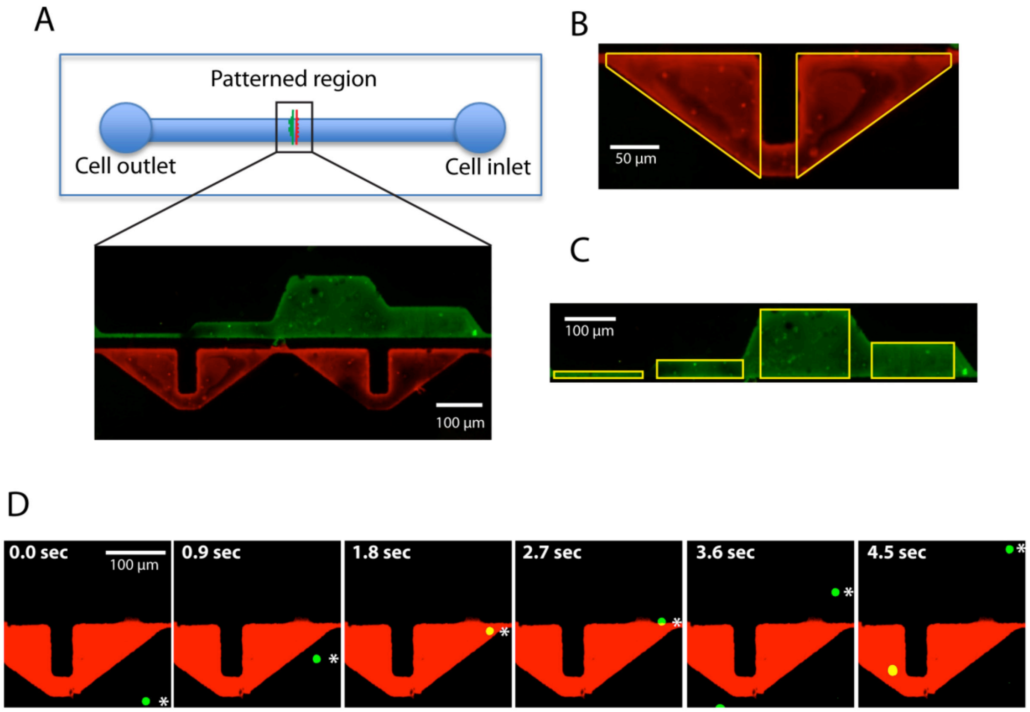

Figure 4. 1 Flowchamber device schematic with the two binding regions highlighted. **(A)** Device schematic of the multi-protein patterned device. (**B**) E-selectin region highlighted in yellow, this region is separated into ten sections for analysis. (**C**) HA region with the 10 µm, 40 µm, 160 µm and 80 µm regions highlighted in yellow. Both regions were imaged after following flowing either Alexa-488 or Alexa-568 to pattern the glass slide. (**D**) Pa03c cell (green) rolling on E-selectin region (red). Interacting cell is indicated by a star.

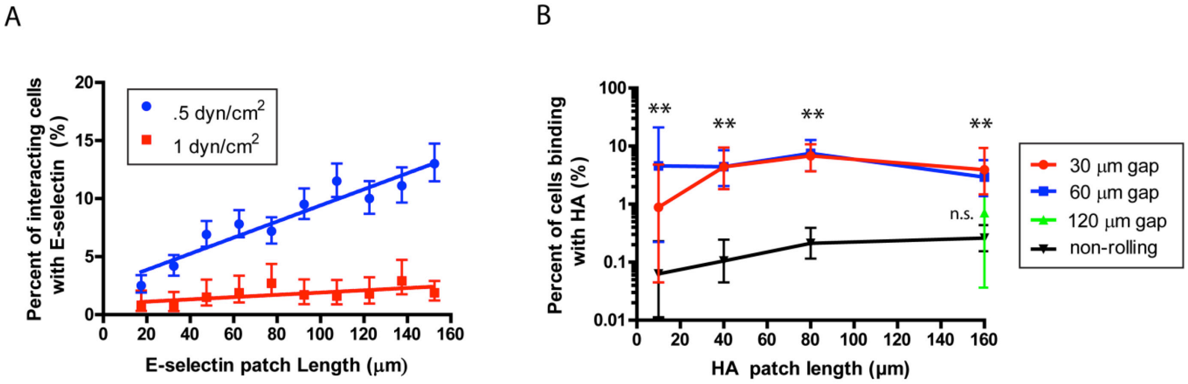

Figure 4. 2 E-selectin facilitates Pa03c cell rolling and rolling increases frequency of binding to HA.

(**A**) The fraction of interacting cells with E-selectin increases with increasing patch length. (**B**) Frequency of binding to HA for cells that roll (red and blue) or that do not roll on E-selectin (black) before binding to HA for the 30 μm, 60 μm and 120 μm gaps (shear stress of .5 dyn/cm^2). Data represents mean ± 95% confidence intervals, p** < .01 for both the 30 μm and 60 μm gaps (red and blue) compared to the non-rolling cells (black).

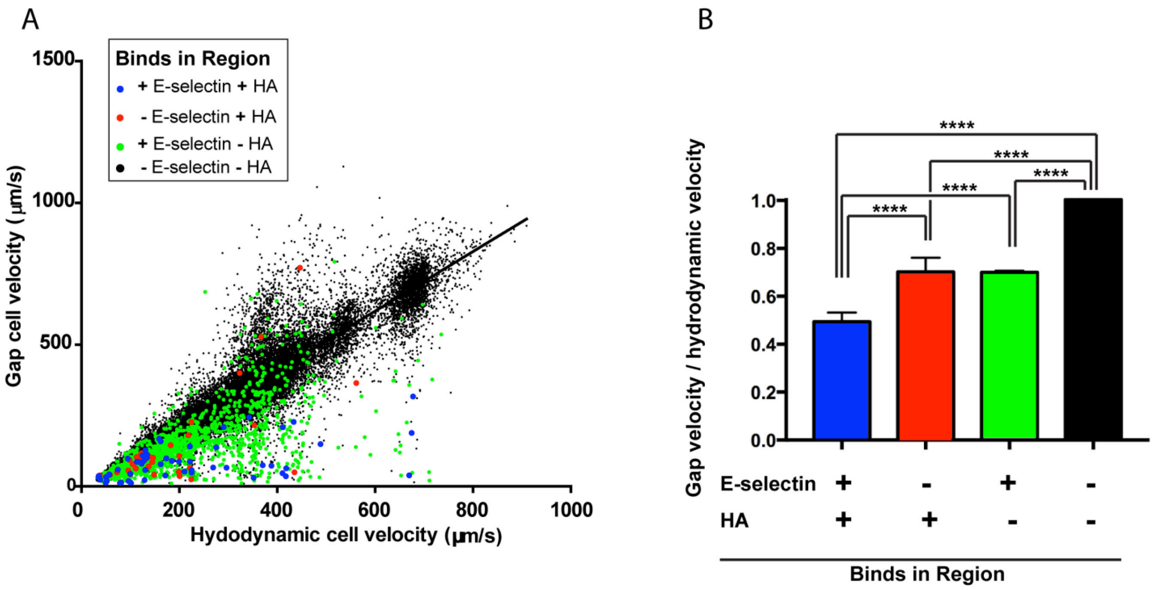

Figure 4. 3 Hydrodynamic cell velocity versus gap velocity for all cells.

(**A**) Cells binding to E-selectin and/or HA show a decreased gap velocity. Black line indicates slope of 1. (**B**) Normalized gap velocity (gap velocity/ hydrodynamic cell velocity) shows that cells, which bind to both E-selectin and HA show a depressed normalized gap velocity when compared to only E-selectin or HA binding cells and non-binding cells. Data represents mean ± S.E.M., p**** < .0001.

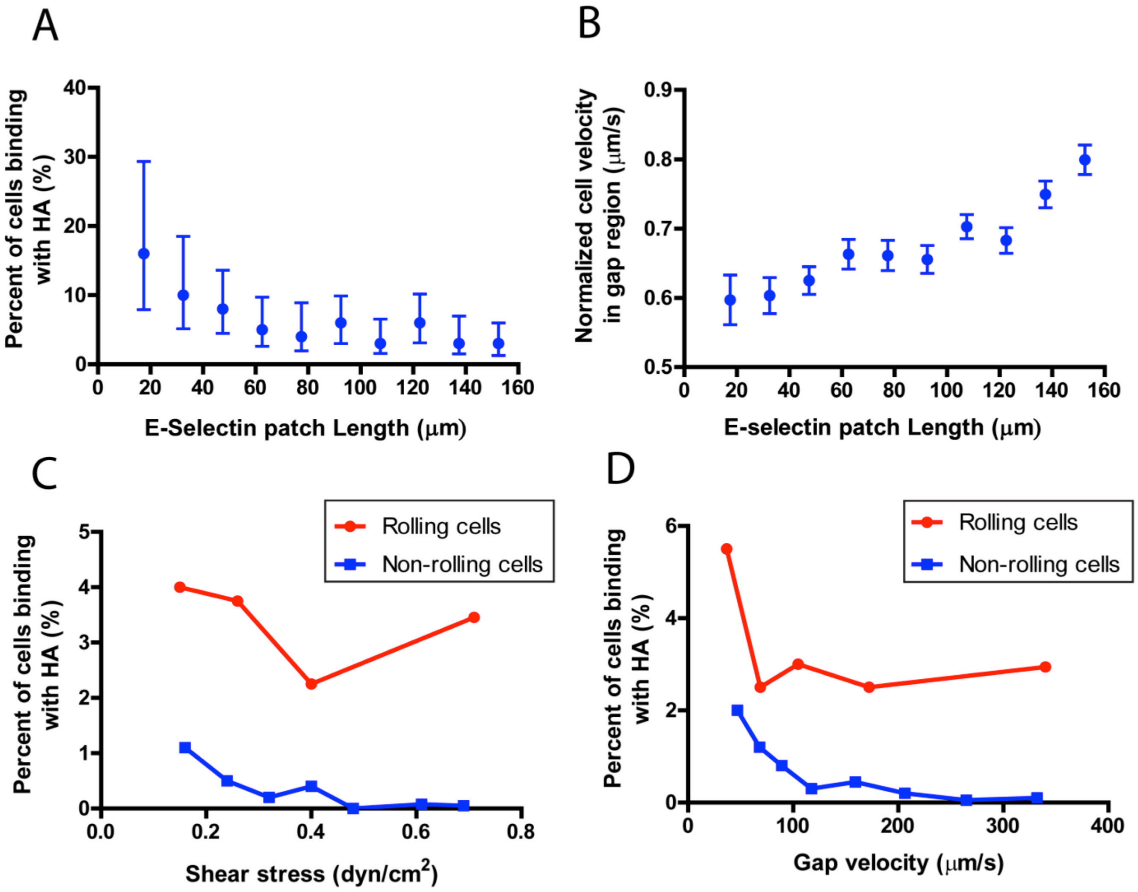

Figure 4. 4 Factors that influence Pa03c cell binding to HA.

(A) Percent of cells binding to HA which first roll on E-selectin binned by E-selectin patch length. Data represents mean ± 95% confidence intervals. **(B)** Normalized gap velocity (gap velocity/hydrodynamic velocity) of cells which roll on E-selectin binned by E-selectin patch length. Data represents mean ± S.E.M. **(C)** Percent of cells binding to HA for rolling and non-rolling cells with increasing shear stress **(D)** Percent of cells binding to HA for rolling and non-rolling cells with increasing gap velocity.

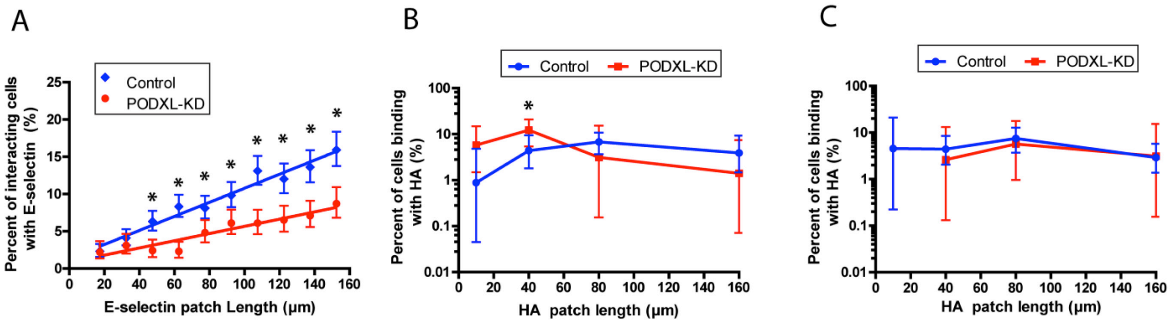

Figure 4. 5 PODXL-KD decreases cell rolling on E-selectin but has a minimal affect on cell binding to HA.

(A) The fraction of interacting cells on the E-selectin region with increasing patch lengths for control and PODXL-KD Pa03c cell at .5 dyn/cm^2. Frequency of binding to HA for cells that first roll on E-selectin for control and PODXL-KD Pa03c cells for the (**B**) 30 μm and (**C**) 60 μm gap distances (shear stress of .5 dyn/cm^2). Data represents mean ± 95% confidence intervals, for (**A**) p* < .01 and (**B**) p* < .05.

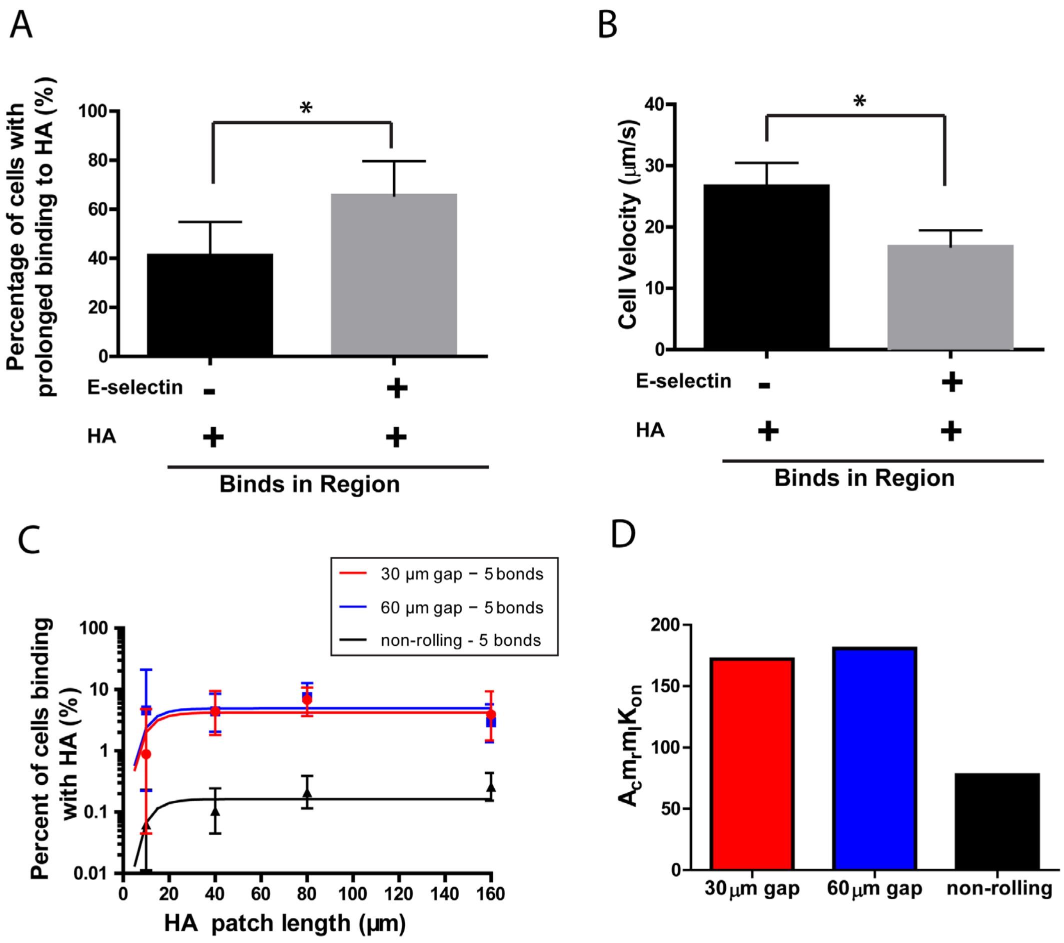

Figure 4. 6 Pa03c cells which adhere to HA and roll first on E-selectin bind longer and roll slower.

All cells interacting with HA were hand tracked once they initiated binding. **(A)** The percentage of cells that bind to HA for longer than 2 seconds. Data represents mean ± 95% confidence intervals. **(B)** The rolling velocities of all cells that interact with HA. Data represents mean ± S.E.M. **(C)** The multi-bond model was fitted to the experimental data (points) and optimized for both $A_cM_rM_lK_{on}$ and n-bonds, with the solid lines representing the model prediction for Pa03c cell binding to HA. Data represents mean ± 95% confidence intervals. **(D)** The $A_cM_rM_lK_{on}$ (lumped binding affinity) determined based on the experimental data.

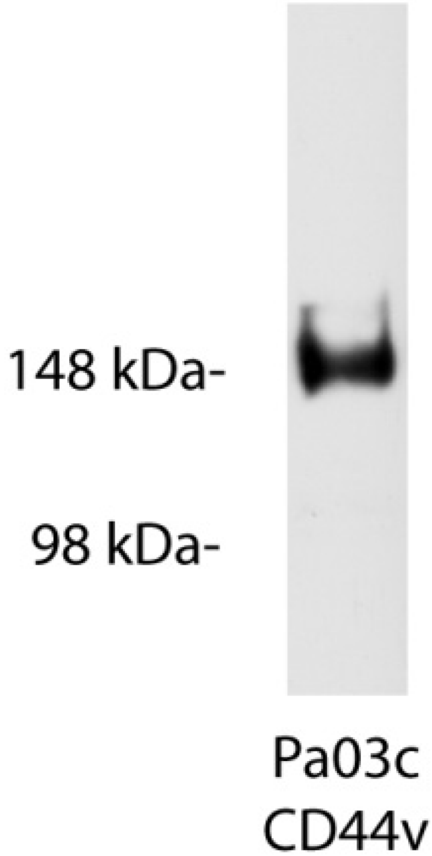

Figure 4. 7 Western blots image of Pa03c cells immune-blotted for CD44.

Pa03c cells and were subjected to SDS-PAGE under reducing conditions. This was followed by western blotting using an anti-CD44 mab. Pa03c cells express CD44v but not CD44s.

Figure 4. 8 Comparison between manually and automatically tracked cells.

Cells were tracked manually (by hand) and using the Matlab tracking program. Identical cells were identified and are compared. **(A and B)** Average X position of cells and the respective Bland-Altman analysis. **(C and D)** Cell velocity in the E-selectin region the respective Bland-Altman analysis. **(E and F)** Cell velocity in the HA region the respective Bland-Altman analysis. (**G**) Percentage of interacting cells in the E-selectin region for the period of time measured. For **A**, **C**, **E** data represents mean ± S.E.M and for **G** data represents mean ± 95% confidence intervals.

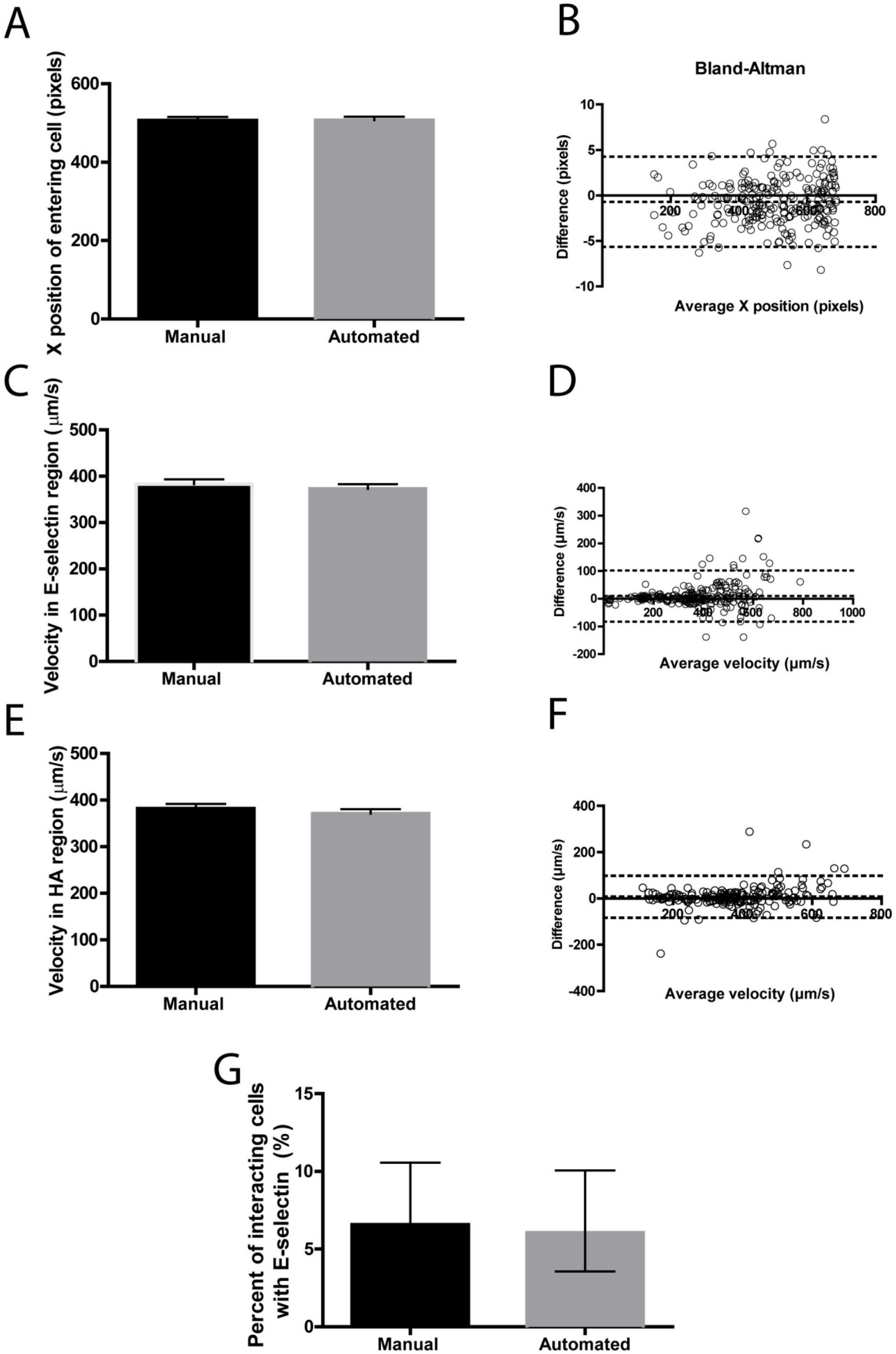
A
X position of entering cell (pixels)
600
400
200
0
Manual
Automated
B
Bland-Altman
Difference (pixels)
10
5
0
-5
-10
200
400
600
800
Average X position (pixels)
C
Velocity in E-selectin region (μm/s)
500
400
300
200
100
0
Manual
Automated
D
Difference (μm/s)
400
300
200
100
0
-100
-200
200
400
600
800
1000
Average velocity (μm/s)
E
Velocity in HA region (μm/s)
500
400
300
200
100
0
Manual
Automated
F
Difference (μm/s)
400
200
0
-200
-400
200
400
600
800
Average velocity (μm/s)
G
Percent of interacting cells with E-selectin (%)
15
10
5
0
Manual
Automated

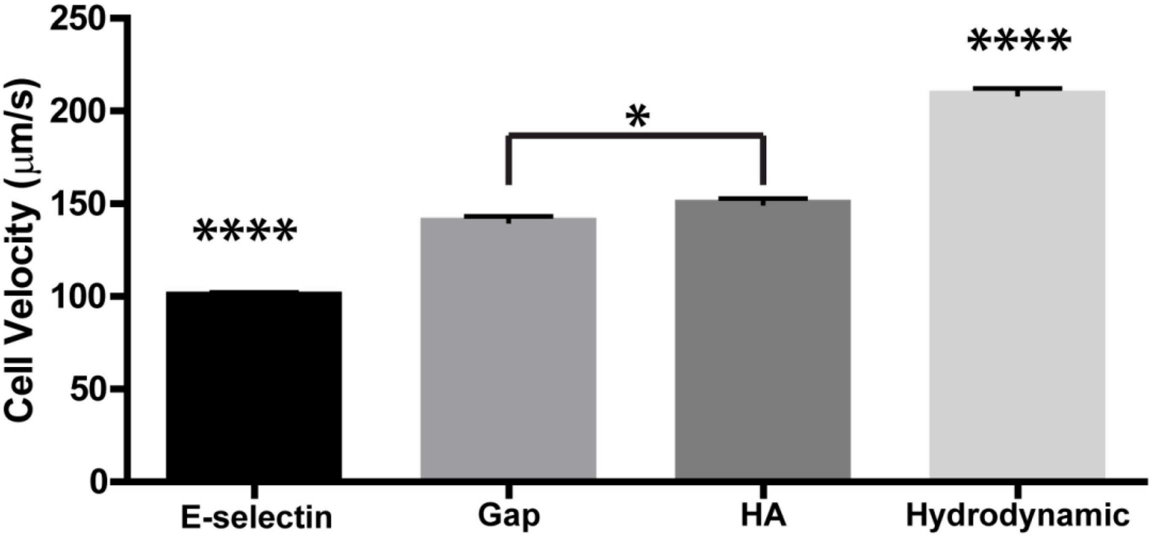

Figure 4. 9 Cell velocities of rolling cells as they pass through the different regions of the device.

Once cells leave the E-selectin region they increase their speed as they begin to reach the hydrodynamic velocity. Data represents mean ± S.E.M., p**** < .0001 with respect to all regions, p* < .05.

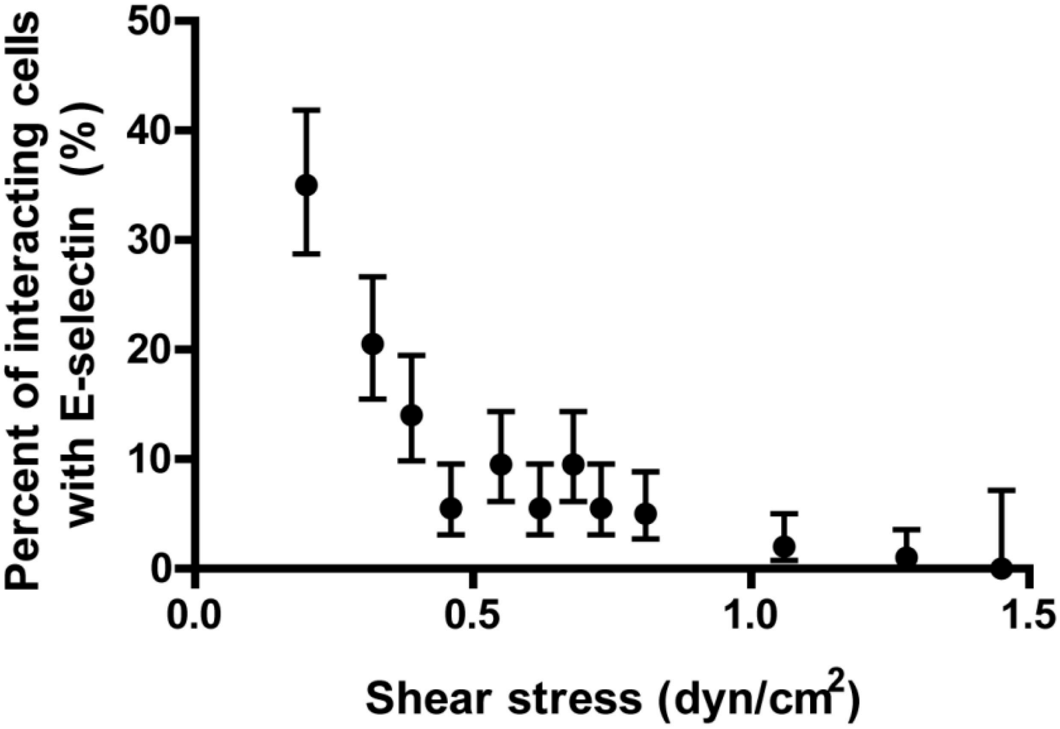

Figure 4. 10 Percent of interacting cells with E-selectin as a function of shear stress. Cells were binned by increasing shear stress at a set E-selectin patch length (70 μm). Data represents mean ± 95% confidence intervals.

Chapter 5

LOSS OF OBSCURIN IN HUMAN PANCREATIC DUCTAL EPITHELIAL CELLS INCREASES CELL MOTILITY AND DYNAMICS

Obscurins are giant cytoskeletal proteins with structural and regulatory roles that are encoded by the *OBSCN* gene. Mutations to the OBSCN gene have been associated with pancreatic ductal carcinoma (PDAC) and the loss of giant obscurin from other cancers has lead to increased tumorigenicity and cell migration. Here we establish that obscurin expression is depleted in PDAC tissue and metastatic cell lines, but remains unaltered in normal pancreatic tissue and non-tumorigenic human pancreatic ductal epithelial cells (HPDE). Stable clones of HPDE cells lacking giant obscurins result in the modification of two major pathways, RhoA and PI3K/AKT which in turn leads to major cytoskeletal alterations including faster actin dynamics at cell-cell junctions, increased microtubule dynamics and decreased focal adhesion density. Further, the loss of obscurin in HPDE cells leads to increased cell migration speeds through trifurcating channels and increased cellular dynamics. Treating these cells with a PI3K inhibitor decreases migration speeds in both confined and unconfined microchannels. Identifying biomarkers such as giant obscurins that increase cell migration and cytoskeletal dynamics is critically important to the prevention and treatment of pancreatic cancer metastasis.

5.1 Introduction

Obscurins are giant cytoskeletal proteins with structural and regulatory roles that are encoded by the gene *OBSCN* that spans 150 kb on chromosome 1q42 in humans (84, 85). The gene undergoes alternate splicing which results in at least 4 isoforms (84, 85). Obscurin A is ~720 kDa and contains various signaling and adhesion domains, including repetitive immunoglobulin (Ig) and fibronectin-III (Fn-III) domains on the amino-terminus and IQ motif, src-homology 3 and Rho-guanine nucleotide exchange factor (Rho-GEF) and pleckstrin homology (PH) motif interspersed by nonmodular sequences on the carboxyl-terminus (86, 87). Obscurin B, with a mass of ~870 kDa contains two serine/threonine kinase domains in place of the nonmodular sequences (84, 85) (Figure 5.1A). Smaller obscurin isoforms contain the serine/threonine kinase domains may also be expressed independently (~55 kDa) or in tandem (~145 kDa) (88).

Analysis of 13,023 genes in colorectal and breast cancer found 189 highly mutated genes and only TP53 and OBSCN were commonly mutated genes in both tumor types (80). In normal breast epithelial cells, obscurins were highly expressed and present at cell-cell junctions (89), however obscurin expression is markedly decreased in breast cancer cells as well as late stage breast cancer biopsies (89, 91). The depletion of giant obscurins from breast epithelial cells has been correlated with increased apoptotic resistance (89), the disruption of adherence junctions leading to epithelial-to-mesenchymal transition (EMT), as well as increased tumorigenicity, microtentacle formation and metastasis (91, 92). However, to this day the role of giant obscurins in pancreatic cancer has gone unexplored.

Recently, mutations in the *OBSCN* gene have been associated with pancreatic ductal adenocarcinoma (81, 82). Given that obscurin has numerous binding domains, the effect of obscurin depletion in other cancers and its implications in pancreatic cancer, we looked to comprehensively evaluate how loss of obscurin in pancreatic epithelial cells affects cell biophysics, migration and tumor formation. Our studies indicate that when giant obscurins depleted from pancreatic cancer tissue biopsies but present in normal pancreatic tissue. Further, the loss of obscurin from normal pancreatic cells induces a migratory phenotype with alterations to cytoskeletal dynamics through decreases in RhoA and increases PI3K/AKT activity. Thus, leading to increased tumor formation and metastasis in vivo.

5.2 Materials and Methods

5.2.1 Reagents and monoclonal antibodies

The antibodies used were as follows; rabbit polyclonal: phospho-PI3K p85 (Tyr458)/p55 (Tyr199) (4228, Cell Signaling Technology Inc), PI3K total (C33D4, Cell Signaling Technology Inc), rabbit monoclonal Phospho-Akt (Ser473) (D9E) XP (4060, Cell Signaling Technology Inc), AKT (pan) (4691, Cell Signaling Technology Inc), mouse monoclonal RhoA (ARH04, Cytoskeleton), rabbit monoclonal Actin(AB-5 BD) rabbit Hsp 90 (C45G5, Cell Signaling Technology Inc), Obscurin-COOH terminal antibody, Obscurin Ig 58/59 antibody and NH2-terminal obscurin [11].

5.2.2 Cell culture

SW1990 and CFPAC-1 were obtained from the American Type Culture Collection (Manassas, VA). The human pancreatic ductal epithelial (HPDE) as well as the Pa03C and Pa07C cells have been previously described (168). HPDE cells were cultured in keratinocyte SFM supplemented with 30 g/ml bovine pituitary extract and 0.1 ng/ml epidermal growth factor (Invitrogen, Carlsbad, CA). CFPAC-1, SW1990, Pa03C, and Pa07C cells were cultured in DMEM supplemented with 10% FBS and 50 mg/ml gentamicin. Panc5.04 were provided by Denis Wirtz and were cultured in DMEM supplemented with 10% FBS (99).

5.2.3 Generation of stable cell lines

A set of 2 short hairpin RNA (shRNA) which target human gene OBSCN and one control (scrambled) shRNA were obtained (Origene). Transfections of the HPDE cell line were performed using Lipofectamine 3000 (Invitrogen). 500ug/ml puromycin (HPDE) was added to the media three days after transfection to select for stably transfected cells. Stable clones expressing obsc shRNA-1, shRNA-2 or shRNA-ctrl were prorogated in the same resistance media. For the transduction of Panc5.04 cells, obsc shRNA-1, shRNA-2 or shRNA-ctrl was incorporated in a viral vector, which contained a GFP domain for sorting, grown in 293T cells. The virus was harvested and purified. Panc5.04 cells were transduced at a 1:10 virus to media ratio. Cells expressing GFP were sorted and the stable clones were propagated. Experiments were performed with pooled clones of each stable line.

5.2.4 Immunofluorescence and confocal microscopy

Cells were fixed with 3.7% paraformaldehyde and permeabilized with .25% Triton X-100 in PBS. Cells were then blocked in 10% normal goat serum (NGS) in PBS containing 1% bovine serum albumin (BSA) and then were incubated overnight with the primary antibodies specified in text. Before being stained for secondary Alexa-fluor-488 or 568 (LifeTechnologies) at a 1:200 dilution unless specified otherwise. Slides were mounted with prolong gold antifade reagent and imaged using either a LSM510 or LSM700 confocal microscope under either 40x or 63x magnification.

5.2.5 Immunohistochemistry

Human pancreatic cancer tumor array slides containing pancreatic ductal carcinoma and matched normal adjacent tissue were examined (US Biomax Inc, Rockville MD, USA). We analyzed 3 biopsies of IDC grade-1, 2 biopsies of IDC grade 1/2, 51 biopsies of IDC grade 2, 12 biopsies of IDC grade 2/3, and 7 biopsies of IDC grade 3 tumors. The tissue microarray was deparaffinized in xylene and rehydrated using ethanol washes. The samples were then subject to antigen revival using 10mM sodium citrate buffer at 90C and washing with cold water. Tissue sections were then washed with TBS (Tris buffered saline) with .025% Triton X-100 (TBST). Slides were blocked with 10% NGS in TBS with 1% BSA for at least 4 h prior to incubation with rabbit polyclonal Ig58/59 antibody in TBS with 1% BSA overnight at 4C. Slides were washed with TBST and incubated with Alexaflour-488 secondary. Following 5 washes with TBST the samples were mounted with prolong gold antifade reagent and imaged using a LSM700 confocal microscope under 40x magnification.

5.2.6 Western blot analysis

Cell lysates were prepared using radio immunoprecipitation assay (RIPA) buffer with protease inhibitor (Roache, Mannheim, Germany). Protein lysates were were separated using a 3-8% Tris-acetate SDS-PAGE gel or a 4-12% Bis-Tris gel (Bio-Rad, Hercules, CA) and transferred to an nitrocellulose membrane. For obscruin western blots the membrane was blocked for 8 h in 10% milk in PTA (PBS, tween-20, sodium azide) buffer before staining with primary antibody. Alkaline phosphatase-conjugated antimouse IgG (1:3000, Jackson ImmunoResearch, West Grove PA, USA) was used and the membrane was developed. For RhoA, PI3K and AKT westerns membrane was blocked for 1 h in 1% BSA in TBST (Tris buffered saline, tween-20) buffer before staining with primary antibody. The gels were washed before being incubated with the appropriate horseradish peroxidase (HRP)-conjugated secondary antibody and the membrane was developed.

5.2.7 Microchannel device fabrication

The microchannel device was fabricated using standard lithography, as previously described. (99, 165, 169). In brief, SU-8 photoresist was spin coated onto a silicon wafer to a thickness of 10 μm and exposed to ultraviolet light through a photomask to cross-link the pattern. The photomask contained the variable "cross" shaped patterns or straight microchannels. The "cross" design features a base channel (10μm) trifurcating to three-branch channels with varying widths of 3, 6 and 10μm. The straight channels design features channels with varying widths (3, 6, 10, 20, 50μm) and a length of 200 μm. The wafer was then treated as previously describe to complete the design (99, 165, 169). In brief the PDMS device was prepared by mixing 10:1 PDMS with curing agent and pouring the PDMS over the silicon wafer. After degassing the PDMS was baked, pealed off the master and the appropriate inlet and out ports were punched into the device. The device and glass cover slips were cleaned and plasma treated before being irreversibly sealed together forming the microchannels. The device surface was functionalized using type-1 collagen (20 µg/ml in PBS) which was added to the inlet ports and incubated for 1 h at 37 °C (99, 165, 169).

5.2.8 Microchannel seeding and cell migration

Microchannels were seeded and data was analyzed according to standard practices as previously described (99, 165, 169) with images taken every 20 mins. For cells treated with LY294002 or BKM120, the inhibitor was dissolved in DMSO and the inhibitor or equivalent volume of DMSO was added to culture media prior to the start of the migration experiment.

5.2.9 Fluorescence recovery after photobleaching (FRAP)

Cells were transfected with LifeAct-RFP using Lipofectamine 3000 (Invitrogen) using conventional methods. 48 h later after transfection, they were re-plated on a glass slide coated in collagen in PDMS wells and allowed to adhere for 24 h and allowed to form a confluent monolayer. Samples were imaged with Zeiss LSM 700 laser scanning confocal microscope (Carl Zeiss). Circular regions with a 4 um diameters were selected at the cell-cells borders and were photobleached with 555-nm laser at 100% power. Images were captured every 1.04 seconds before and after photobleacing using x63X/1.4

N.A. oil immersion objective and the LSM software. Analysis of the images was previously described (91) At least 20 images of the cell-cell borders were analyzed per cell set.

5.2.10 EB1 assay for measuring microtubule dynamics

Cells were transfected with EB1-GFP or EB1-RFP using Lipofectamine 3000 (Invitrogen) using conventional methods. 48 h later after transfection, they were re-plated on a glass slide coated in collagen in PDMS wells and allowed to adhere for 24 h at ~50% confluencey. Samples were imaged with Zeiss LSM 700 laser scanning confocal microscope. Cells were imaged a 3.08 second intervals for 6.16 minutes. Life history plots and kymographs of microtubules in each cell were generated. MT growth rates were then determined from the kymographs. Approximately 20 MT in each cell were analyzed and at least 11 cells per condition were imaged.

5.2.11 Total internal reflectance fluorescence (TIRF) microscopy

Cells (50,000 per slide) were seeded on a collagen coated glass cover slip or glass bottom dish and allowed to adhere for 24 hr. Cells were fixed and stained as described previously (99, 170) using anti phospho-paxillin primary (1:50) and Invitrogen Alexa 568 secondary antibody (1:2000). Stained cells were imaged by total internal reflection fluorescence (TIRF) microscopy using a 3i Mariana inverted microscope (Intelligent Imaging Innovation, Inc) using a 100x/1.45 N.A. oil immersion objective and Slidebook 8.0 software (Intelligent Imaging Innovation, Inc). Images were processed and quantified as previously described (99, 170) After normalizing for background staining, images were made binary, and the particle analyzer tool was used in ImageJ to measure pY-paxillin– positive punctate areas >0.1 μm^2. The total focal adhesion area, number of focal adhesions per area and the area of focal adhesions were then determined. TIRF experiments were repeated three times, for a total of at least 40 cells per condition.

5.2.12 RhoGTPase Pulldown

Cells with either *OBSCN* or ctrl-shRNA were grown and harvested for Rho GTPase pulldowns as per the manufacturer's protocols (Cytoskeleton, Inc). The pulldown assay was performed as per the manufacturer's protocols (Cytoskeleton, Inc). Densitometry was performed using ImageJ software.

5.2.13 Statistical analysis

Statistical analysis was performed using the students T-test or two proportion Z test unless otherwise noted.

5.3 Results

5.3.1 Obscurin is highly expressed in human pancreatic epithelial cells and down regulated in PANC tissue

Obscurin was indicated as a frequently mutated gene in PDAC and therefore we investigated the expression of giant obscurin in several pancreatic cell lines (81, 82). A panel of pancreatic cancer and normal cell lines were evaluated for giant obscurin A and

B through immunoblotting using an antibody against the COOH terminus of giant obscurin proteins. We tested one human epithelial pancreatic cell line, HPDE (human pancreatic ductal epithelial) and four metastatic cell lines including CFPAC-1 and Pa03c (isolated from liver metastases of pancreatic tumors), Pa07c (a peritoneal pancreatic metastasis), and SW1990 (isolated from the splenic metastasis of a pancreatic tumor). HPDE cells express the highest levels of giant obscurin A and B while SW1990 express intermediate levels of obscurin and CFPAC-1 and Pa03c cells express low levels of giant obscurin (Figure 5.1B). This is consistent with a serial analysis of gene expression which indicate the same trends in mRNA levels for the all cells lines tested (HPDE, Pa03c and Pa07c) (168). Interestingly giant obscurin was present in normal HPDE, while it was expressed in lower levels in the tumor forming SW1990 cells but was virtually absent from other cancer cell lines tested. We believe this correlates with the epithelial nature of HPDE and SW1990 (52) and the slower migration velocity of SW1990 cells in confinement (65).

The staining of obscurin using antibodies targeting COOH terminus of the obscrurin (89) confirmed the expression of obscurin in HPDE (Figure 5.1C). Here obscurin is localized at the cell interior, in the nucleus and at the perinuclear/cytoplasmic puncta. It is notably absence of obscurin from cell-cell junctions. When HPDE cells are treated with 10% FBS for 24 hrs obscurins are localized at the cell membrane and the localization profile resembles that of SW1990 cells (Figure 5.7A and B and 5.10). Nuclear and cell-cell junction localization of obscurin is consistent with observations of obscurin localization in breast epithelial cells (89).

To explore if obscurin expression correlates with pancreatic tumor progression, we investigated the expression profile of obscurins in human biopsies of pancreatic tissue using fluorescent immunohistochemistry. Biopsies of 75 PDAC or adenosquamous carcinoma biopsies and matched normal adjacent tissue stained using an antibody specific to Ig58/59 of giant obscurin A and B (Figure 5.1A) and imaged using confocal microscopy. Obscurin is highly expressed in acinar cells and the ductal and lobular epithelium of normal pancreatic tissue (Figure 5.2A). It was found to be localized both membraneously (ductal) and in the cell interior, especially in acinar cells, and at times in the nucleus. However, obscurins are markedly reduced in the highly differentiated PDAC tissue (Figure 5.2A and B). Normal pancreatic tissue expressed high levels of obscurin in ~70% of patients while matched tumor samples highly express obscurin in under 20% of patient samples (Figure 5.2C) and obscurin expression was found to decrease with increasing tumor grade (Figure 5.2D). In tumor tissue samples, obscurin was localized primarily to the membranes of ductal cells and to puncta throughout the tumor.

5.3.2 The downregulation of giant obscurins increases cell dynamics and migration through trifurcating microchannels

Considering the decreased levels of giant obscurins A and B in metastatic pancreatic cancer lines and in high-grade pancreatic tumor tissue we examined the role of obscurin in cell migration. In this regard we generated stable HPDE cell lines expressing shRNA plasmids targeting obscurin A and B (shRNA-1 targeting Ig9 and shRNA-2 targeting Ig45), which reduced obscurin expression and a control shRNA (shRNA-ctrl) (Fig 1C).

To examine the impact of the obscurin downregulation on HPDE cell migration in trifurcating microchannels, we developed “cross”-shaped PDMS microchannels with a base channel (10μm) trifurcating to three-branch channels with varying widths of 3, 6 and 10μm (Fig 3). This device looks to mimic complex and asymmetrical physical microenironments which cells encounter as they migrate from a primary tumor (171, 172). Cells were imaged as the migrated up the base to the trifurcation (intersection) region and eventually to one of the three channel branches (Figure 5.3A). Obscurin-KD HPDE cells spent less time in the intersection regardless of the branch dimensions (3-10-6, 10-10-10, and 3-10-10 μm, channel width in microns for left, center, and right branches respectively)(Figure 5.3E-F). This result was consistent for both the presence and absence of 10% FBS in the media (Figure 5.11).

In symmetrical “cross”-shaped (10-10-10 μm) microchannels (Figure 5.3G-I), cell speeds and shape factors were analyzed in the three regions. Obscurin-KD HPDE cells migrated with a faster velocity in the trifurcation region, thus confirming the lower time observed for KD cells in the intersection. In the trifurcation region, obscurin-KD HPDE cells were also more protrusive (lower solidity) and less circular than control cells indicating these cells were more dynamic.

5.3.3 Cellular dynamics and the role of RhoA

Rho GTPase proteins, including RhoA, are largely involved in regulating the cell cytoskeleton (173). Decreases in RhoA activity have been indicated to decrease FA size and stress fiber formation, increase MT dynamics (94-96) and drive tumor cell migration and invasion (97). Given that the RhoGEF motif of giant obscurin A and B specifically binds and activates RhoA (92), RhoGTPase pull-down was performed to assess RhoA activity in obscurin-KD HPDE cells. We determined that the obscurin-KD decreased levels of active RhoA in HPDE cells (Figure 5.4C). To further explore the effects of obscurin mediated RhoA depletion we assessed effects of obscurin-KD in HPDE cells on microtubule dynamics and focal adhesion expression.

Since RhoA has been indicated to stabilize microtubules (174) and the loss of RhoA has been associated with increased MT dynamics (94) we quantified MT growth using EB1-GFP which binds to the plus end (+TIP) of growing microtubules (175) and imaged cells using live-cell confocal microscopy. Control or obscurin-KD HPDE cells containing the EB1-GFP plasmid were imaged over 6 min, and growing microtubules comets were tracked (Figure 5.4A). The growth rate of microtubules in obscurin-KD HPDE cells significantly was faster when compared to control HPDE cells indicating more dynamic MT assembly (Figure 5.4B and 5.9B).

Because myosin II is a downstream effector of RhoA/ROCK pathway and increased myosin II activity promotes tyrosine-phosphorylation of paxillin (98, 99) we utilized TIRF microscopy to explore pY-paxillin expression in the focal adhesion of obscurin-KD and control HPDE cells (Figure 5.4D). We found the loss of obscurin decreased both focal adhesion density and average focal adhesion size in HPDE cells (Figure 5.4E) indicating a decrease in myosin II activity. This taken together with the MT data indicates that the loss of obscurin and consequential decrease in RhoA activity is likely in part responsible for the faster and more dynamic migration observed through the trifurcating microchannels.

5.3.4 Cellular dynamics and obscurin localization

Given the increase cell dynamics and faster migration through a trifurcating microchannels as well as the decrease in active RhoA we assessed whether the obscurin-KD affected actin dynamics. We quantified actin dynamics as cell-cell junctions using fluorescence recovery after photobleaching (FRAP). LifeAct-RFP was expressed by both control and obscurin-KD HPDE and these cells were grown to a confluent monolayer. Cells with intense fluorescence at cell-cell junctions were selected, and bleached in a 4μm diameter circular region. After ~60 seconds the fluorescence recovers at the cell-cell junction, although not to the extent of the prebleach levels (Figure 5.7C and D). When HPDE cells (both control and obscn-KD) were grown in normal growth media no difference was found in either the mobile fraction or the half-life of actin recovery (Figure 5.7C). However, when cells were grown in media with 10% FBS 24 h prior to imaging, obscn-KD HPDE cells displayed a higher mobile fraction when compared to control HPDE cells, while no significant difference was observed for half-life (Figure 5.7D). Therefore changes in actin dynamics correlate with obscurin localization (Figure 5.7A and B). Only in the presence of FBS, when obscurin is localized to the cell-cell junctions does the loss of giant obscurins increase actin dynamics (Figure 5.7).

5.3.5 Migration of obscurin depleted HPDE cells are decreased after treatment with PI3K inhibitors.

Recently we determined that the PH domain of obscurin binds to the p85 regulatory subunit of phophsoinositide-3 kinase (PI3K) in breast epithelial cells (93).

Given that upregulation of the PI3K pathway has found in 50% of human cancers, including pancreatic cancer and generally correlates increased proliferation and migration in a chemotactic gradient we investigated if the depletion of obscurin affects the PI3K pathway and modulates cell migration (176-179). We sought to examine if the enhanced motility and cell dynamics of obscurin downregulated HPDE cells are due in part to the activation of the PI3K/AKT pathway. In this regard we evaluated protein levels of pPI3K/p85 and pAKT via immunoblotting. We determined that levels of pPI3K/p85 (Tyr458) regulatory subunit and pAKT (Ser473) were upregulated in obscurin depleted HPDE cells while levels of PI3K and AKT remain constant (Figure 5.5A).

We next evaluated the ability of single HPDE cells treated with the PI3K inhibitors LY294002 or BKM120 to migrate through collagen type I-coated microchannels with varying widths (6, 10, 20 and 50 μm) and a constant height of 10 μm imaged with live-cell phase-contrast microscopy. These channels were selected because treated cells could migrate into them more easily than the "cross" design discussed earlier. We found that obsc-shRNA HPDE cells migrated significantly slower when treated with both 25μM LY294002 and 2μM BKM120 compared to cells treated with DMSO (Figure 5.5 C and E). These differences were consistent for both unconfined (50 and 20μm) and confined (10 and 6μm) channel migration. In contrast ctrl-shRNA HPDE cells treated with either LY294002 or BKM120 migrated through both unconfined and confined microchannels at the same speed when compared to DMSO treated cells (Figure 5.5 B and D). Taken together, these data indicate that activation of the PI3K/AKT pathway in obscrurin depleted HPDE cells increases cell migration and that the inhibition of the PI3K/AKT pathway impairs single cell migration of obscurin depleted HPDE cells resulting in decreased cell migration speed.

3.5.6 Downregulation of obscurin Panc5.04 cells shows faster migration and cell dynamics

Too confirm the previous migration and cytoskeletal dynamics results we performed these experiments with obscurin expressing Panc5.04 cells, which are derived from a stage IIB pancreatic tumor. These cells express giant obscurins A and B and therefore we depleted the giant obscurin isoforms using shRNA targeting Ig45 of obscurin (Figure 5.6B). Consistent with HPDE cells, obscurin-KD Panc5.04 cells express increased levels pPI3K/p85 regulatory subunit and downstream effectors pAKT as well as well as decreased levels of active RhoA (Figure 5.6E and I). Furthermore, Panc5.04 OBSCN-KD cells migrate faster through symmetrical and asymmetrical trifurcating microchannels (Figure 5.6C and D), display faster actin dynamics at cell-cell junctions as well as increased microtubule dynamics and decreased focal adhesion area (Figure 5.6F-H, J-M). Given the mechanobiological similarities with HPDE cells, we believe that obscurin-KD Panc5.04 cells act as a suitable cell line for future in vivo work.

5.4 Discussion

In cancer, cells develop genetic alterations, which result in uncontrolled proliferation and the activation of complex signaling pathways that encourage cell survival, migration and invasion. While studies have shown that obscurin depletion from breast epithelial cells increase resistance to apoptosis, EMT protein expression, cell migration and tumorigenicity (89, 91), little is known about how giant obscurins affect normal pancreatic tissue and cells. In this regard, we comprehensively evaluated how loss of obscurin in pancreatic cells affect cell biophysics, migration and tumor formation.

Consistent with the observation for breast tumor tissue, pancreatic tumor biopsies grade >1 showed significantly decreased levels of obscurin (Figure 5.2A). This supports the observation that mutations in the OBSCN gene have been associated with pancreatic ductal adenocarcinoma and adjacent pancreatic intraepithelial neoplasia, which are precursors invasive ductal adenocarcinoma (81, 82). In tumor tissue biopsies, obscurins were absent from invasive adenocarcinoma cells that invaded into the pancreatic parenchyma (Figure 5.2A) indicating obscurin depleted cells are more invasive. This is supported by the increased in cell migration speed and cytoskeletal cell dynamics observed for obscurin depleted epithelial cells (Figure 5.3D-I, 5.4B, E and 5.6). Interesting obscurin localization in the pancreatic ductal epithelium and acinar resembles that of the HPDE cells where obscurin is localized at the cell-cell junctions and cell interior in the presence of FBS (Figure 5.7).

The loss of obscurin from HPDE and Panc5.04 results in increased RhoA activity and the activation of the PI3K/AKT pathway. Rho family GTPases and their downstream effectors are critical to cell migration and motility (179, 180). RhoA inhibition can lead to either decreased levels of migration through inhibition of cell contractility or increased migration through decreasing cellular adhesion in a cell dependent manner (181). The depletion of RhoA in breast and prostate tumor cells is associated with cell elongation, the formation of actin rich protrusions and increased cancer cell invasion (97). The expression the obscurin RhoGEF domain in kidney cells resulted in increased levels of active RhoA while the depletion of obscurin in breast epithelial cells resulted in decreased levels of RhoA (92, 182). Our results show decreased activity of RhoA in obscurin depleted pancreatic epithelial cells. Increased actin dynamics and decreased FA density can result from decreased RhoA activity, which effects contractility and is associated with cell adhesion (96). Further, RhoA depletion is associated with increase MT dynamics and rear retraction in cell migration (94, 179). Therefore, the altered actin and MT dynamics, and FA expression in obscurin-KD pancreatic epithelial cells likely results from decreases in RhoA activity and is at least partially responsible for the faster cell migration decision making in trifurcating microchannels.

We have also show that the activation of PI3K/AKT pathway in obscurin depleted pancreatic epithelial cells. Obscurin is thought to bind and inactivate the PI3k/p85 regulatory subunit making it unable to modulate the PI3K/p110 catalytic subunit, thus leading to aberrant activation of the pathway (93). Increased activation of the PI3K/AKT pathway affects many cellular processes including cell survival, apoptosis, stemness, motility and invasion, factors which ultimately result in increased tumorigenicity and metastasis (183, 184). The activation of this pathway in obscurin depleted HPDE and Panc5.04 cells likely in part leads to the increased in vitro cell migration.

Panc5.04 cells were selected as an alternative to HPDE because they are tumorigenic cells with a similar heteroginity profile to HPDE cells (185-187). A study which differentiated pancreatic tumor and metastatic pancreatic cells into subgroups based on several factors including nuclear size distribution and entropy cells size distribution indicates that Panc5.04 are more like HPDE cells than metastatic pancreatic tumor cell lines (187). Therefore they are an excellent alternative for HPDE for future in vivo experiments.

Here we observed the depletion of giant obscurins from PDAC tissue and metastatic cell lines, but it is abundant in normal pancreatic tissue and human pancreatic ductal epithelial cells. We find that the loss of obscurin from HPDE cells results in the modification of two major pathways, RhoA and PI3K/AKT which results in major cytoskeletal alterations including faster actin dynamics at cell-cell junctions, increased microtubule dynamics and decreased FA density. This leads to increased migration speeds and decision making in trifurcating channels. Identifying markers which promote cell migration and cell dynamics is vital to the prevention and treatment of metastatic pancreatic cancer.

5.4 Figures

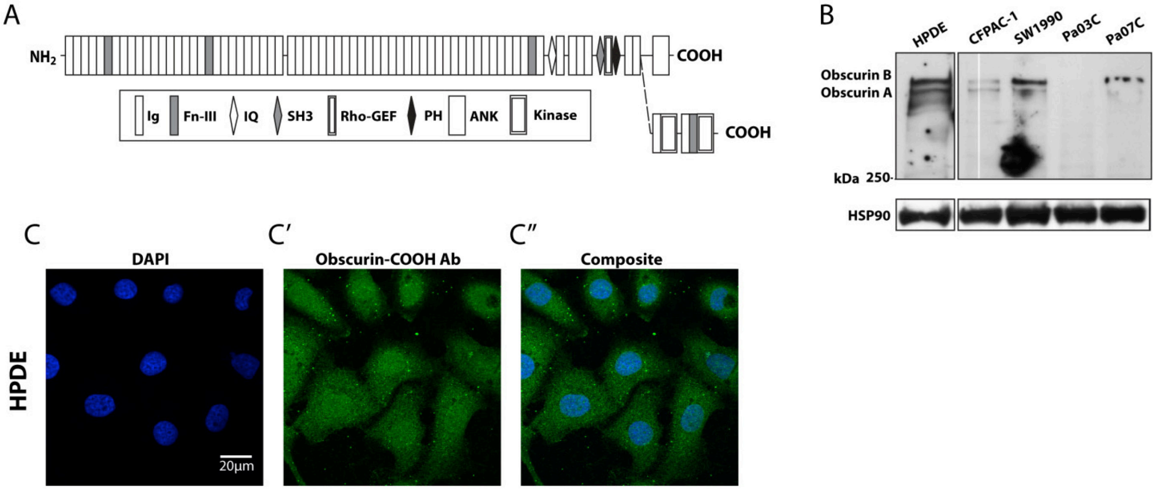

Figure 5. 1 Obscurin expression in pancreatic cell lines and the localization of obscurin in HPDE cells.

(A) Schematic of giant obscurins A and B with the binding domains illustrated. **(B)** Immunoblots showing the expression giant obscurin isoforms for one normal pancreatic cell lines (HPDE) and several cancer cell lines (CFPAC-1, SW1990, Pa03C, and Pa07C). **(C)** Immunostaining used to determine the expression of obscurin in HPDE cells. Obscurin (green) is localized in the cell interior, at perinuclear/cytoplasmic puncta and in the nucleus.

Figure 5. 2 Pancreatic tissue microarray staining for obscurin shows loss of obscurin in pancreatic ductal adenocarcinoma (PDAC) tissue when compared to normal tissue.

(A) Representative images of pancreatic tissue biopsies of grade 1-3 pancreatic adenocarcinoma and matched normal tissue. Hematoxylin and eosin (H&E) stained images display a boxed region (left), which was imaged using confocal (right) after staining with the obscurin Ig 58/59 antibody (green) and dapi (blue). **(B)** Obscurin expression normalized to the levels of obscurin in the normal tissue for the entirety of each matched tissue sample. Data represents mean ± S.E.M, p** < .0001 **(C)** Obscurin levels were graded for tissue sample on a 0-3 scale based on obscurin intensity. Tissue samples were evaluated for elevated levels (grade 2 or greater) of obscurin expression in PDAC and normal tissue. Data represents mean ± 95% confidence intervals, p** < .0001 **(D)** Tissue samples were evaluated for obscurin intensity PDAC and normal tissue and plotted as a function the tumor grade. Data represents mean ± S.E.M, p* < .01, p** < .0001.

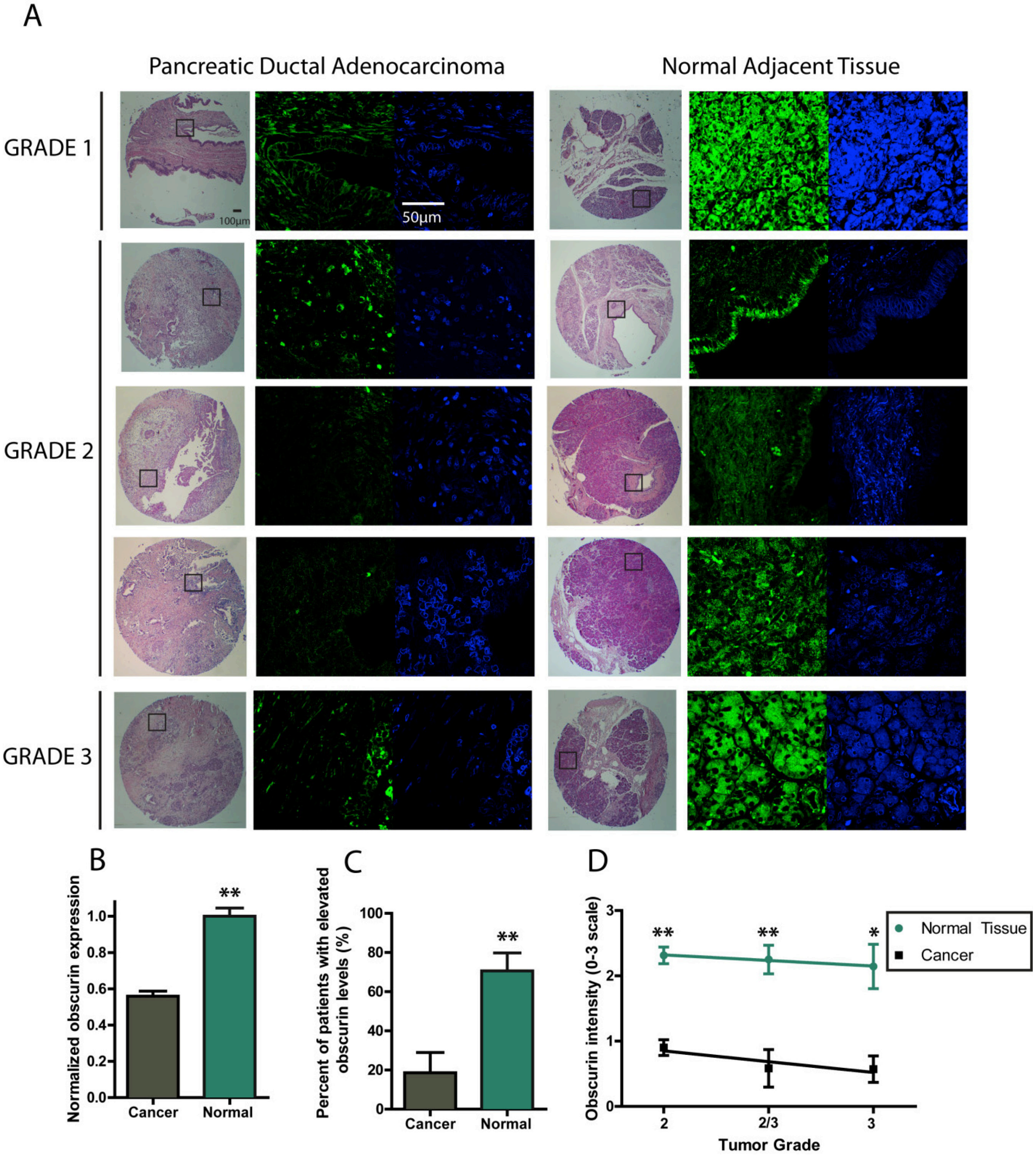
A
Pancreatic Ductal Adenocarcinoma
Normal Adjacent Tissue
GRADE 1
100µm
50µm
GRADE 2
GRADE 3
B
Normalized obscurin expression
1.0
0.8
0.6
0.4
0.2
0.0
**
Cancer
Normal
C
Percent of patients with elevated obscurin levels (%)
100
80
60
40
20
0
**
Cancer
Normal
D
Obscurin intensity (0-3 scale)
3
2
1
0
**
**
*
Normal Tissue
Cancer
2
2/3
3
Tumor Grade

Figure 5. 3 Obscurin-KD HPDE cells spend less time in symmetrical and asymmetrical trifurcations and are more dynamic.

(A) Schematic of the symmetrical “cross” shaped device. Cells migrate into the channel base, and through the trifurcation region to the branch region. Both the base and each branch channel have a width of 10µm. **(B)** Time-lapse images of control and obscurin shRNA-1 HPDE cells migrating through symmetrical “cross” shaped microchannels. Arrowheads point to individual cells as they migrate through the device. **(C)** Giant obscurins A and B are downregulated in HPDE following the stable transduction with obscurin shRNA-1 or -2 compared to control cells. **(D-F)** Time that migrating HPDE cells spent in the intersection of the “cross” shaped devices that trifucate into branches with widths from left to right of either **(D)** of 3, 10 and 6µm, **(E)** of 3, 10 and 10µm, or **(F)** or 10, 10 and 10µm. **(G)** The average speed **(H)** Circularity and **(I)** solidity of HPDE cells in the trifurcation region. Data represents mean ± S.E.M, p* < .05, p** < .01.

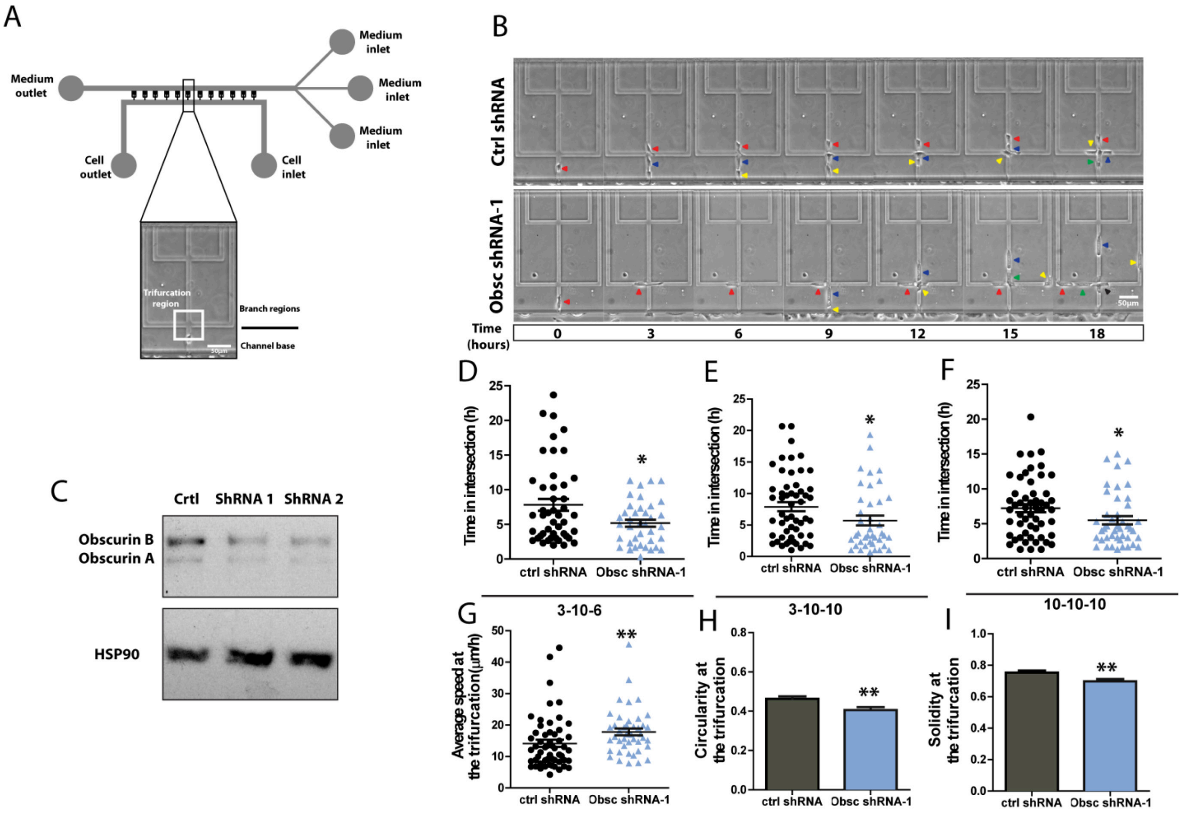
A
Medium outlet
Medium inlet
Medium inlet
Medium inlet
Cell outlet
Cell inlet
Trifurcation region
Branch regions
Channel base
50μm
B
Ctrl shRNA
Obsc shRNA-1
50μm
Time (hours)
0
3
6
9
12
15
18
C
Crtl
ShRNA 1
ShRNA 2
Obscurin B
Obscurin A
HSP90
D
E
F
Time in intersection (h)
ctrl shRNA
Obsc shRNA-1
*
3-10-6
3-10-10
10-10-10
G
Average speed at the trifurcation(μm/h)
**
H
Circularity at the trifurcation
**
I
Solidity at the trifurcation
**

Figure 5. 4 Obscurin-KD HPDE cells display faster microtubule dynamics and decreased FA density and size.

(A) Time lapse images showing the EB1-GFP comets of HPDE ctrl and obscurin-shRNA cells. White dots indicate growing microtubules. **(B)** Microtubule growth rate of HPDE cells. **(C)** Active RhoA is decreased in HPDE cells expressing obscurin shRNA-1. Actin and total RhoA act as loading controls. **(D)** Representative TIRF microscopy images of HPDE cells (ctrl and obsc shRNA-1) stained with pY-paxillin to visualize focal adhesions (FAs). The cell boundary is traced in yellow. **(E)** Average focal adhesion size per cell, the average focal adhesion density per cell and the average focal adhesion area per cell area. Data represents mean ± S.E.M, $p^* < .05$, $p^{**} < .01$, $p^{***} < .001$, $p^{****} < .0001$.

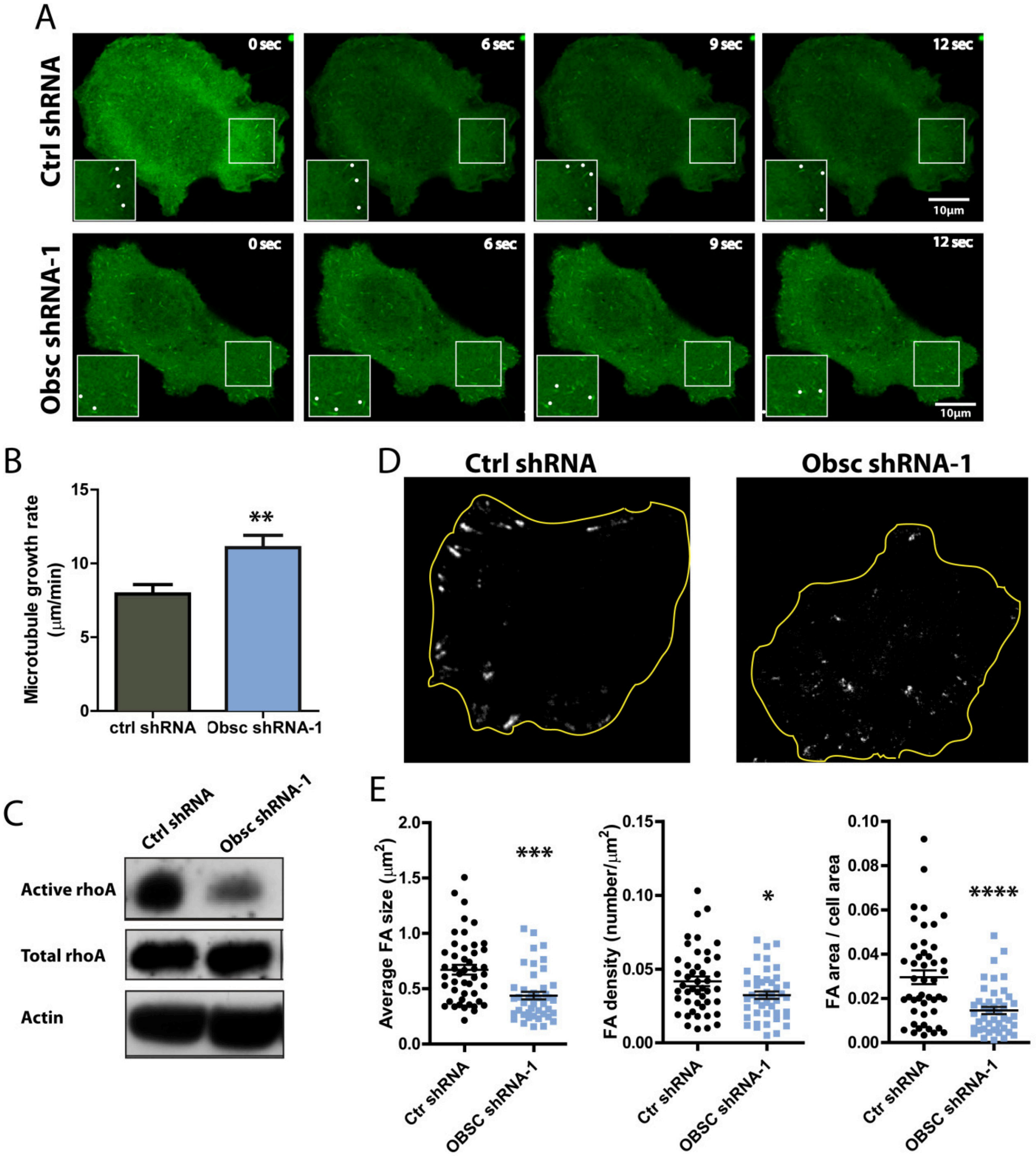
A
Ctrl shRNA
Obsc shRNA-1
0 sec
6 sec
9 sec
12 sec
10μm
B
Microtubule growth rate (μm/min)
15
10
5
0
**
ctrl shRNA
Obsc shRNA-1
C
Ctrl shRNA
Obsc shRNA-1
Active rhoA
Total rhoA
Actin
D
Ctrl shRNA
Obsc shRNA-1
E
Average FA size (μm²)
2.0
1.5
1.0
0.5
0.0
***
FA density (number/μm²)
0.15
0.10
0.05
0.00
*
FA area / cell area
0.10
0.08
0.06
0.04
0.02
0.00
****
Ctr shRNA
OBSC shRNA-1

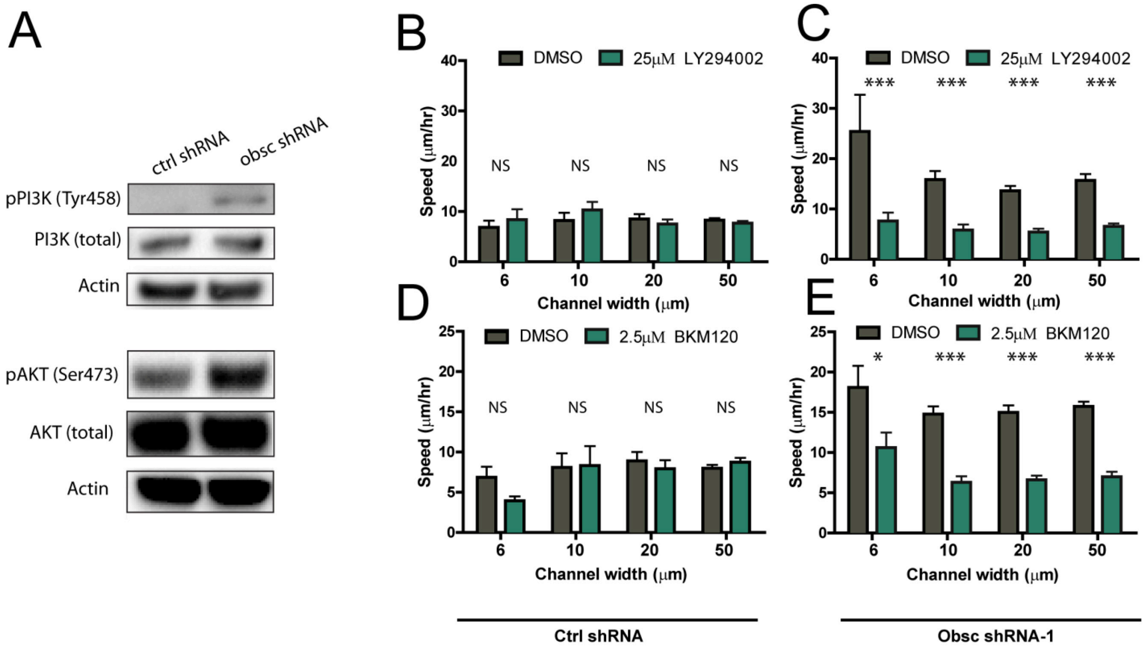

Figure 5. 5 Downregulation of obscurin in HPDE cells increases PI3K activity and treatment with a PI3K inhibitor decreases migration speeds in these cells.

(A) Levels of pPI3K (Tyr458) and the downstream effector pAKT (Ser473) were increased in obscurin knockdown HPDE cells. HPDE control cells when treated with the PI3K inhibitor **(B)** ly294002 or **(D)** BKM120 showed no difference in cell migration speeds through straight microchannels with widths varying from 6 to 50μm. HPDE obscurin shRNA-1 cells when treated with the PI3K inhibitor **(C)** ly294002 or **(E)** BKM120 displayed a decrease in cell migration speeds through straight microchannels with widths varying from 6 to 50μm. Data represents mean ± S.E.M, p* < .05, p*** < .001.

Figure 5. 6 Downregulation of obscurin in Panc5.04 cells display the same mechanobiogical phenotype as HPDE obscurin depleted cells.

(A) Immunostaining shows the expression of obscurin in Panc5.04 cells. Obscurin (green) is localized in the cell interior, in the nucleus, and at cell-cell junctions. White arrows heads indicate obscurin localization of obscurin at cell-cell contacts and at the cell leading edge. **(B)** Giant obscurins A and B are downregulated in Panc5.04 cells following the stable transduction with obscurin shRNA compared to control cells. **(C)** Obscurin shRNA Panc5.04 cells migrate through the intersection of the symmetrical "cross" microchannel device with a faster speed and in less time than control Panc5.04 cells. **(E)** Active RhoA is decreased in Panc5.04 cells expressing obscurin shRNA. **(F)** Lifeact-RFP expressing Panc5.04 cells were bleached at a circular region of 4 μm in diameter at the cell-cell junction and imaged as actin recovered. FRAP curve shows the faction of actin recovery versus time. **(G)** The mobile fraction of actin and the **(H)** half-life of actin recovery are shown. **(I)** Levels of pPI3K (Tyr458) and the downstream effector pAKT (Ser473) were increased in obscurin knockdown Panc5.04 cells. **(J)** Microtubule growth rate of Panc5.04 cells. **(K-M)** Average focal adhesion size per cell, the average focal adhesion density per cell and the average focal adhesion area per cell area for Panc5.04 cells. Data represents mean ± S.E.M, p* < .05, p** < .01, p*** < .001.

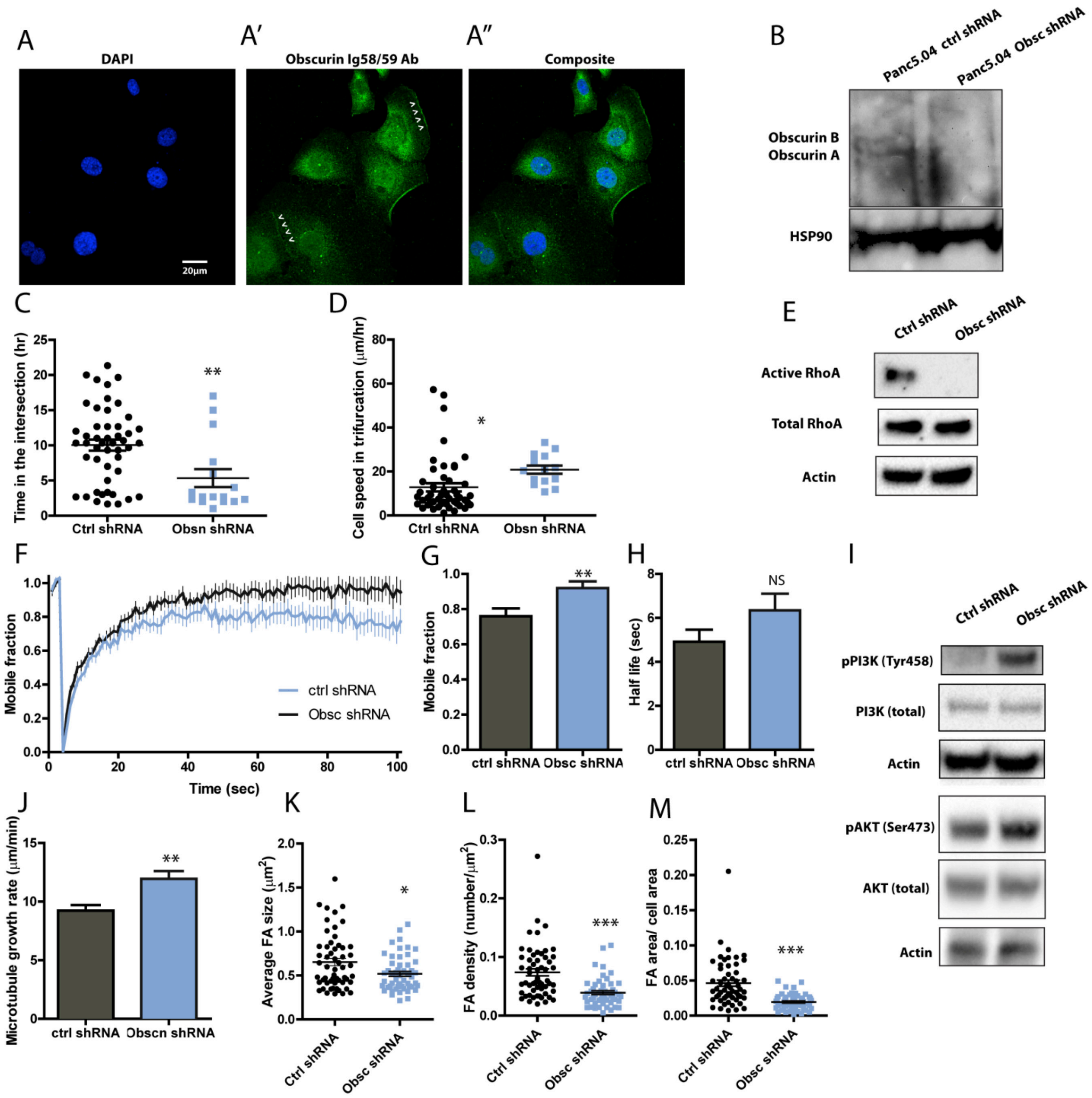

A
DAPI
20µm
A′
Obscurin Ig58/59 Ab
A″
Composite
B
Panc5.04 ctrl shRNA
Panc5.04 Obsc shRNA
Obscurin B
Obscurin A
HSP90
C
Time in the intersection (hr)
0
5
10
15
20
25
**
Ctrl shRNA
Obsn shRNA
D
Cell speed in trifurcation (µm/hr)
0
20
40
60
80
*
Ctrl shRNA
Obsn shRNA
E
Ctrl shRNA
Obsc shRNA
Active RhoA
Total RhoA
Actin
F
Mobile fraction
0.0
0.2
0.4
0.6
0.8
1.0
0
20
40
60
80
100
Time (sec)
ctrl shRNA
Obsc shRNA
G
Mobile fraction
0.0
0.2
0.4
0.6
0.8
1.0
**
ctrl shRNA
Obsc shRNA
H
Half life (sec)
0
2
4
6
8
NS
ctrl shRNA
Obsc shRNA
I
Ctrl shRNA
Obsc shRNA
pPI3K (Tyr458)
PI3K (total)
Actin
pAKT (Ser473)
AKT (total)
Actin
J
Microtubule growth rate (µm/min)
0
5
10
15
**
ctrl shRNA
Obscn shRNA
K
Average FA size (µm²)
0.0
0.5
1.0
1.5
2.0
*
Ctrl shRNA
Obsc shRNA
L
FA density (number/µm²)
0.0
0.1
0.2
0.3
***
Ctrl shRNA
Obsc shRNA
M
FA area/ cell area
0.00
0.05
0.10
0.15
0.20
0.25
***
Ctrl shRNA
Obsc shRNA

Figure 5. 7 HPDE cells with decreased levels of obscurin show faster actin dynamics only in the presence of FBS, when obscurins localize at cell-cell contacts.

Immunostaining used to determine the expression of obscurin in HPDE cells in the **(A)** absence and **(B)** presence of FBS. Arrowheads indicate obscurin the localization of obscurin at cell-cell contacts in the presence of 10% FBS. **(C and D)** FRAP was performed on life-act expressing HPDE in the **(C)** absence and **(D)** presence of FBS. FRAP curve shows the faction of actin recovery versus time. The mobile fraction of actin and the half-life of actin recovery are shown. Actin recovers faster for HPDE obsc shRNA-1 and -2 compared to control HPDE in the presence of FBS.

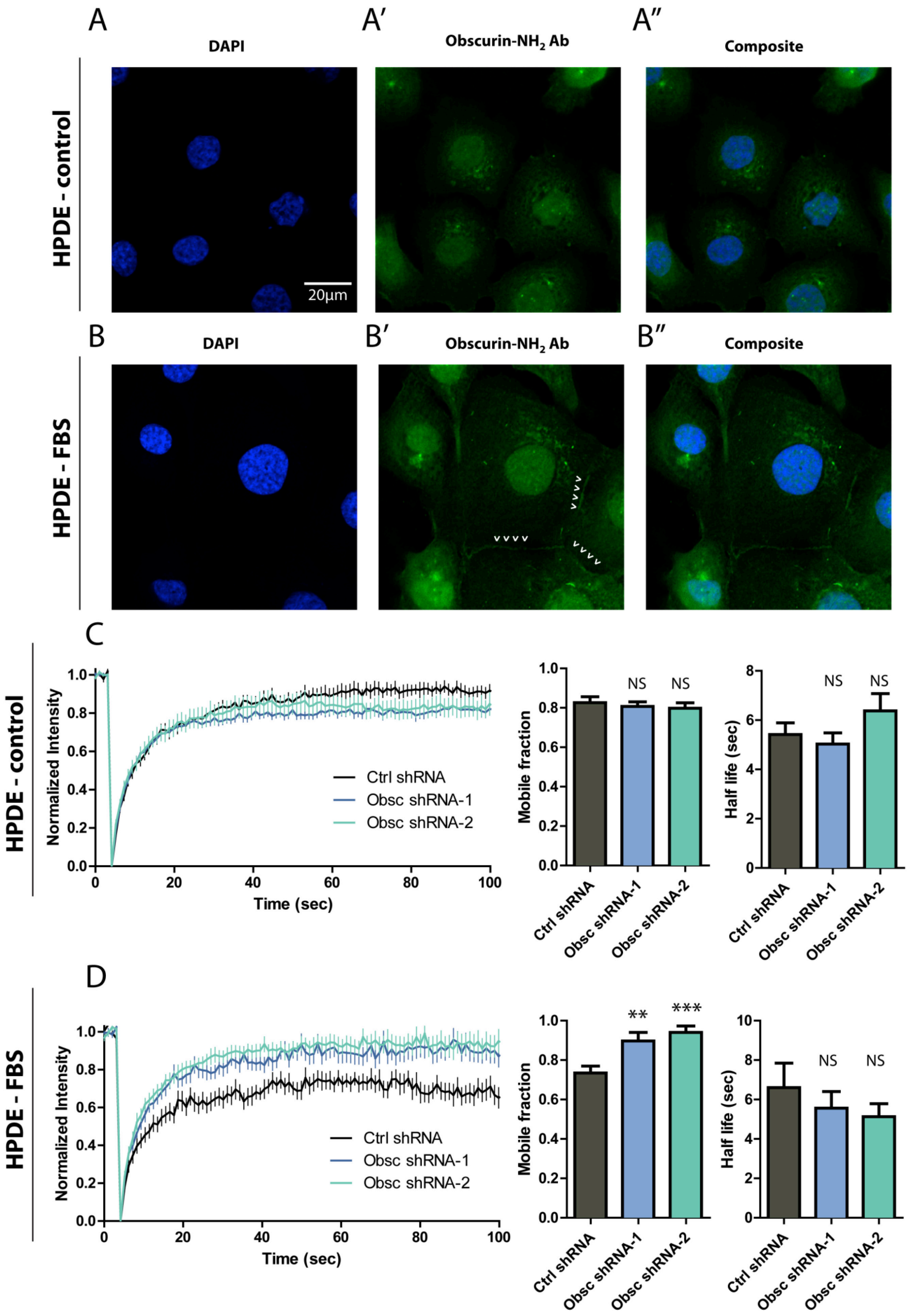
A
DAPI
A′
Obscurin-NH₂ Ab
A″
Composite
HPDE - control
20µm
B
DAPI
B′
Obscurin-NH₂ Ab
B″
Composite
HPDE - FBS
C
HPDE - control
Normalized Intensity
1.0
0.8
0.6
0.4
0.2
0.0
0
20
40
60
80
100
Time (sec)
Ctrl shRNA
Obsc shRNA-1
Obsc shRNA-2
Mobile fraction
NS
NS
Ctrl shRNA
Obsc shRNA-1
Obsc shRNA-2
Half life (sec)
8
6
4
2
0
NS
NS
D
HPDE - FBS
Normalized Intensity
Time (sec)
Ctrl shRNA
Obsc shRNA-1
Obsc shRNA-2
Mobile fraction
**
***
Half life (sec)
10
NS
NS

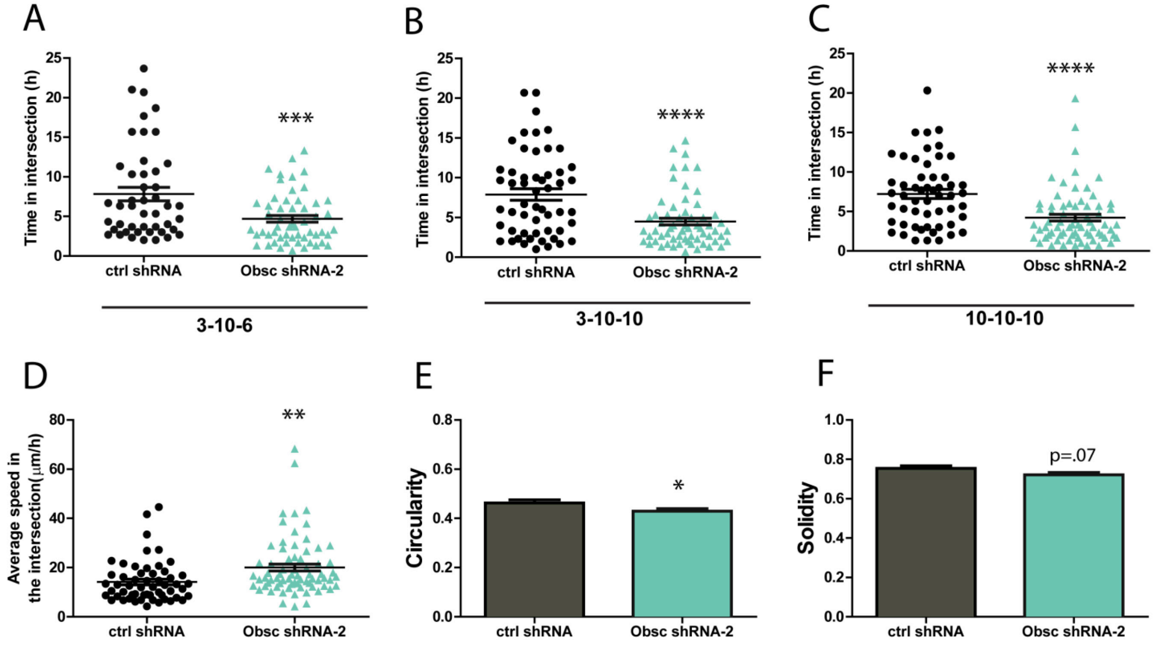

Figure 5. 8 Obscurin-KD HPDE cells spend less time in a symmetrical or asymmetrical trifurcation and are more dynamic, with shRNA-2.

(A-C) Time that migrating shRNA-2 and crtl shRNA HPDE cells spent in the intersection of the "cross" shaped devices that trifucate into branches with widths from left to right of either **(A)** of 3, 10 and 6µm, **(B)** of 3, 10 and 10µm, or **(C)** or 10, 10 and 10µm. **(D)** The average speed **(H)** circularity and **(I)** solidity of HPDE cells in the trifurcation region. Data represents mean ± S.E.M, p* < .05, p** < .01.

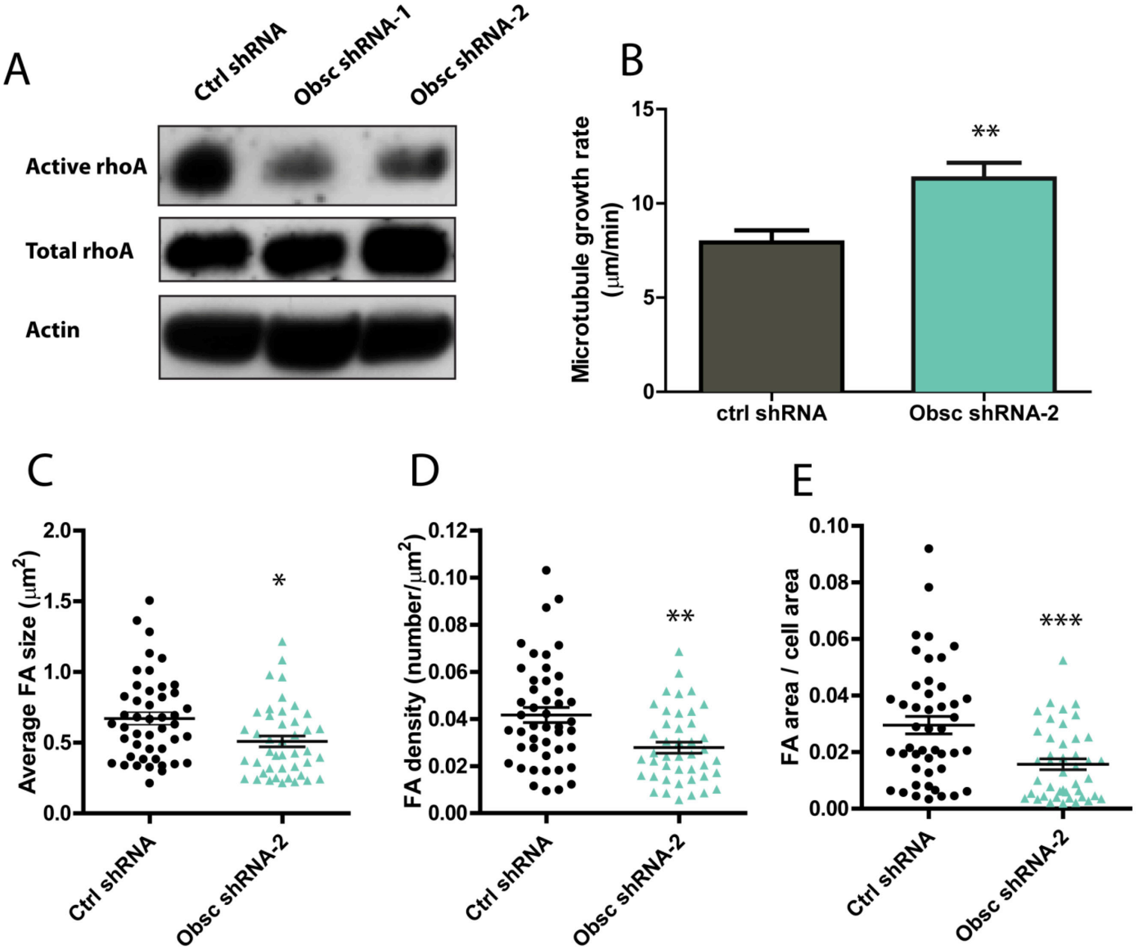

Figure 5. 9 Obscurin-KD HPDE cells display faster microtubule dynamics and decreased FA density and size, with shRNA-2.

(A) Active RhoA is decreased in HPDE cells expressing obscurin shRNA-1 and shRNA-2. Actin and total RhoA act as loading controls. **(B)** Microtubule growth rate of obscurin shRNA-2 and crtl-shRNA HPDE cells. **(C-E)** Average focal adhesion size per cell, the average focal adhesion density per cell and the average focal adhesion area per cell area. Data represents mean ± S.E.M, p* < .05, p** < .01, p*** < .001.

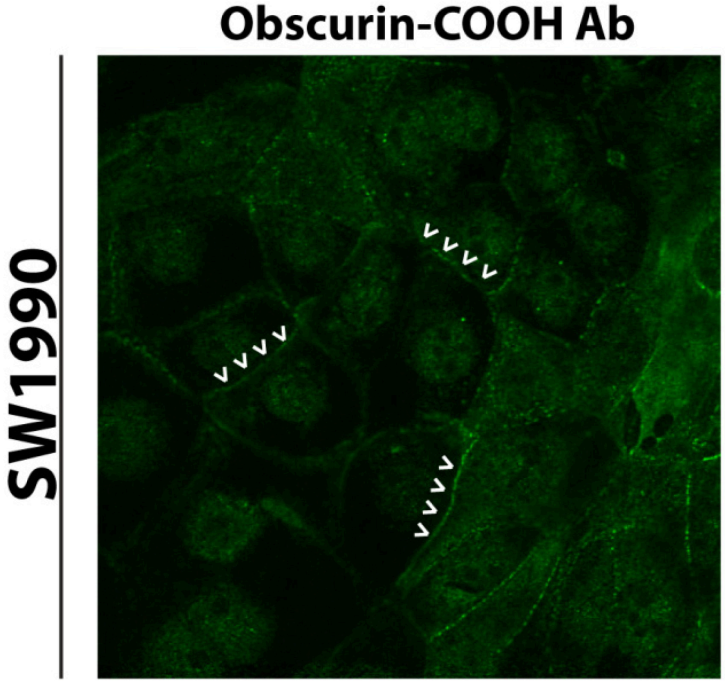

Figure 5. 10 Obscurin staining of SW1990 cells.

Immunostaining used to determine the expression of obscurin in SW1990 cells. Arrowheads indicate the localization of obscurin at cell-cell contacts. Obscurin localization in SW1990 cells are similar to that of HPDE cells treated with 10% FBS, where obscurin is localized at the cell-cell junctions and in the nucleus.

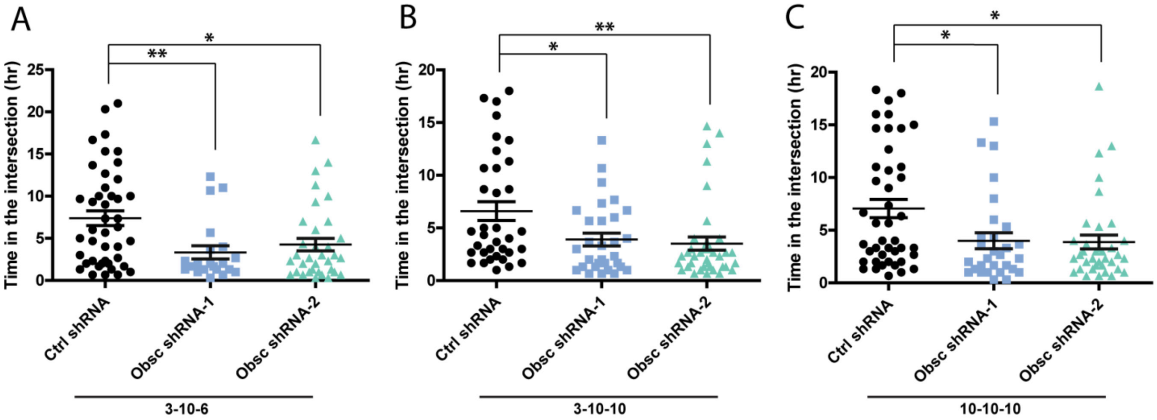

Figure 5. 11 Obscurin-KD HPDE cells spend less time in a symmetrical or asymmetrical trifurcation in the presence of 10% FBS.

(A-C) Time that migrating shRNA and crtl shRNA HPDE cells spent in the intersection of the "cross" shaped devices that trifucate into branches with widths from left to right of either **(A)** of 3, 10 and 6µm, **(B)** of 3, 10 and 10µm, or **(C)** or 10, 10 and 10µm. Cells were treated with FBS for 24 h prior to the start of the experiment. Data represents mean ± S.E.M, p* < .05, p** < .01.

Chapter 6

CHARACTERIZATION OF MONOBODY SCAFFOLD INTERACTIONS WITH LIGAND VIA FORCE SPECTROSCOPY AND STREERED MOLECULAR DYNAMICS

Monobodies are antibody alternatives derived from fibronectin that are thermodynamically stable, small in size, and can be produced in bacterial systems. Monobodies have been engineered to bind a wide variety of target proteins with high affinity and specificity. Using alanine-scanning mutagenesis simulations, we identified two scaffold residues that are critical to the binding interaction between the monobody YS1 and its ligand, maltose-binding protein (MBP). Steered molecular dynamics (SMD) simulations predicted that the E47A and R33A mutations in the YS1 scaffold substantially destabilize the YS1-MBP interface by reducing the bond rupture force and the lifetime of single hydrogen bonds. SMD simulations further indicated that the R33A mutation weakens the hydrogen binding between all scaffold residues and MBP and not just between R33 and MBP. We validated the simulation data and characterized the effects of mutations on YS1-MBP binding by using single-molecule force spectroscopy and surface plasmon resonance. We propose that interfacial stability resulting from R33 of YS1 stacking with R344 of MBP synergistically stabilizes both its own bond and the interacting scaffold residues of YS1. Our integrated approach improves our understanding of the monobody scaffold interactions with a target, thus providing guidance for the improved engineering of monobodies.

6.1 Introduction

High affinity proteins are utilized in a wide spectrum of applications ranging from chemical and biological threat detection (188) to protein-based therapeutics (189). Although monoclonal antibodies have traditionally been favored as therapeutic biomolecules, they are large in size, require eukaryotic expression for production (108), and generally offer poor thermal stability (109). As a result, synthetic antibody mimetic proteins based on molecular scaffolds have gained popularity. Utilizing a conserved protein scaffold as a platform and combinatorial engineering techniques, selections for high affinity binding or conformational stability can be performed (110, 111). Synthetic domains have also been engineered to produce biosensors (190, 191) and achieve binding to a wide array of molecules (116, 192). Engineered protein scaffolds have been explored for use as both therapeutics (112) and diagnostics (113). An increased understanding of how scaffold structure affects interactions with ligands will facilitate the engineering of improved scaffold proteins.

The protein of interest in this study is derived from the tenth fibronectin III domain (FNfn10) scaffold (114, 115). Similar to the immunoglobulin (Ig) complementarity determining region, the ~94 amino acid peptide contains a β-sheet backbone and three relevant loop domains (BC, DE, and FG) (114, 115). The three loops have been diversified using phage or yeast display combinatorial libraries to produce proteins known as monobodies, with low nanomolar (116, 117) to picomolar K_d values

(118) and the capability to bind to targets such as small ubiquitin-related modifiers (SUMO) (119), maltose-binding protein (MBP) (116, 117), lysozyme (118), and fyn kinase (120). Comparable binding affinity to antibodies coupled with the absence of disulfide bonds, ease of production in bacterial systems (114, 121), and high thermal stability (122) are reasons why monobodies have become attractive alternatives to antibodies as therapeutic biomolecules.

A better understanding of monobody interactions with their ligands (paratope/epitope binding) will allow for improved monobody design. Here, we have studied the interaction of monobody YS1 with its ligand, maltose-binding protein (MBP), with a focus on scaffold interactions. YS1 was developed by Koide et al. (116) utilizing a Y/S binary combinatorial library platform to diversify amino acids on the BC, DE, and FG loops of the FNfn10 scaffold. The monobody was originally named MBP-74 but was subsequently renamed YS1 (117). The X-ray crystal structure of YS1 bound to MBP shows the convex paratope of YS1 binding to the sugar binding pocket of MBP (116, 117). Based on the crystal structure, the interacting paratope of YS1 includes both loop and scaffold proteins. Alanine-scanning mutagenesis indicates that the BC loop of the monobody does not significantly contribute to binding, but that alanine mutations at seven of the nine residues of the FG loop result in greater than 10-fold decrease in affinity (117). Although it has been speculated that the contacts with the scaffold residues are a crystallization artifact (116), the effect of mutations on these scaffolds has not been reported. Previous studies on monobodies have mainly focused on altering the BC, DE, and FG loops to achieve high binding affinities and increased protein stability (116, 117, 193). While scaffold modifications have been considered in modifying monobody structural stability (194, 195) and in combination with loop modifications (119), little work has focused solely on how interacting scaffold residues affect binding kinetics. Utilizing computational modeling and biophysical analyses we have explored how scaffold modifications affect YS1-MBP binding kinetics.

Structure-based design of therapeutic molecules is becoming increasingly important with the growth of structural databases and increased computing speeds (125, 126). Whereas the x-ray crystal structure reveals interactions in the context of a static crystal, molecular dynamics simulations can show instantaneous molecular movement and are useful for determining the preferred motion of proteins (196). Through steered molecular dynamics (SMD) an external force is applied to a binding pair and the dissociation interactions are measured with respect to time (197). As a result, the structural mechanics of the unbinding process can be explored. Single molecule force spectroscopy is a biophysical method to experimentally examine such processes, and has been utilized to measure binding kinetics of cell-to-cell interactions protein-protein interactions between single molecules (41-43, 47, 67, 139, 140).

Typically only a small fraction of buried residues contributes to the majority of the binding affinity in binding interactions. These residues are referred to as hot spots (198, 199). Hot spots have been studied in a wide a range of human antibodies and other natural proteins, and modification of these residues has a substantial destabilizing effect on the protein interface (198, 199). We sought to identify the hot spots of the YS1-MBP interface on the previously unstudied scaffold interactions using computational alanine-scanning mutagenesis. By coupling molecular simulations and biophysical tools we have characterized the critical interacting β-sheet residues of YS1 and assessed their influence on binding kinetics. With the increasing interest in the development of scaffold based mimetic proteins, an understanding of scaffold hot spots will lead to the creation of better-targeted therapeutics.

6.2 Materials and methods

6.2.1 Construction, expression, and purification of TMD-MBP

The plasmid encoding the CD44 trans-membrane domain (TMD) fused to MBP utilizes the isopropyl b-D-1-thiogalactopyranoside (IPTG)-inducible T7 promoter to allow for the cytoplasmic expression of TMD-MBP (139). TMD-MBP was expressed and purified using an amylose affinity chromatography column as described except that BL21(DE3) cells were used (139).

6.2.2 Construction, expression, and purification of wild-type and mutated Monobody YS1

The pHFT2 plasmid encoding the YS1 gene with a (His_{10}) tag at the N-terminus (116) was a gift from Shohei Koide (University of Chicago). The R33A and E47A mutations were made by site directed mutagenesis in this plasmid and verified by DNA sequencing. The monobodies were expressed and purified from BL21(DE3) cells. Cells were grown in M9 media with 10 g/L tryptone, with expression induced with IPTG. Expressed monobodies were immobilized and purified using a GE HisTrap HP column via their N-terminal His_{10} tag. The purified monobodies were dialyzed at 4°C against 300 volumes of phosphate-buffered saline (PBS, pH 7.4). Monobody concentrations were determined using their extinction coefficients.

6.2.3 Molecular dynamics simulations

The starting coordinates for the molecular dynamics (MD) simulations were obtained from the crystal structure of YS1 in complex with MBP (Protein Data Bank ID: 2OBG) (116). The R33A and E47A *in silico* mutations were generated by replacing either R33 or E47 with alanine. Both wild-type and mutated YS1 were fully solvated in a rectangular water box of 80×87×80 $Å^3$ by using the Visual Molecular Dynamics program (200). Sodium and chloride ions were added to neutralize the system, which yielded 51,635 atoms in total. The MD simulations were performed by following a protocol similar to our previous study (139). In brief, the NAMD software was used to perform MD simulation by using a CHARMM22 force field and the TIP3P water model (201-203). Periodic boundary conditions were applied to avoid finite size effects, and electrostatic interactions were simulated using the particle-mesh Ewald sum method (204). A 12 Å cutoff distance was applied for calculating van der Waals interactions. The system has gone through energy minimization by a 20,000-steps-of-conjugate gradient with heavy atoms fixed followed by another 20,000 steps with all atoms free. After gradually heating from 0 to 300 K in 60 ps, the system is equilibrated for at least 2.5 ns with temperature at 300 K and pressure at 1 atm by using the Langevin dynamics method (205, 206). The profile of RMSD plots for the backbone atoms of monobody-MBP complex reached a plateau value, which indicated that the systems had reached an equilibrium state.

The steered molecular dynamics (SMD) simulations were performed using six pairs of monobody-MBP complexes randomly selected from the equilibrated systems. A constant pulling speed of 10 Å/ns was applied through a spring with a stiffness of 70 pN/Å on the residue Val72, which is near the center of mass of the monobody. The pulling direction was designed to pull the monobody away from the center of mass of MBP. The C_α atoms of the 322, 325 and 326 residues of the MBP were constrained to their equilibrated positions. These residues were chosen because they are located on the opposite side of the binding pocket of MBP. The generalized born implicit solvent (GBIS) model implemented in the NAMD was used to manipulate the water molecules in SMD simulations. Periodic boundary conditions were considered in all SMD studies. However, Particle mesh Ewald method is not supported in the GBIS. The solvent molecular electrostatics were calculated by the Poisson-Boltzmann equation which models water as a dielectric continuum in NAMD (207). Production runs were performed by using a computer equipped with eight CPUs and 12 GB RAM. Each simulation contains 4 ns data and took approximately five days to finish. Snapshots were saved in every 0.5 ps to analyze the dissociation trajectory. Simulations of mutated monobodies followed the same protocol as mentioned above.

Hydrogen bonds were calculated using the VMD software utilizing the hbonds plugin v1.2, which measures the hydrogen bonds of each interacting YS1 residue throughout the trajectory. Hydrogen bonds were considered to be formed between the hydrogen donor (D) and another atom (the acceptor, A) given that the distance D-A is less than the cut-off distance at 3.5Å and the angle D-H-A is within the cut-off angle at 180±60 degrees (208). Only polar atoms were considered in the calculation.

6.2.4 Alanine-scanning mutagenesis

Following the annealing and equilibrium achieved using MD simulation, the 6-8 randomly selected monobody-MBP complexes were entered into to the computational alanine-scanning program on the Robetta server (209) (http://robetta.bakerlab.org/) and the DrugScorePPI webserver (210) (http://cpclab.uni-duesseldorf.de/dsppi/main.php). Here, all amino acids at the YS1-MBP interface were identified and individually mutated to alanine. The change in binding free energy ($\Delta\Delta G_{bind}$) or the change in the mutated complex partner protein stability in isolation ($\Delta G_{partner}$) was measured. Additionally the degree of buriedness was identified for interfacial residues. The binding free energy function utilized here accounts for solvation interactions, shape complementarity of interacting atoms, and the polar interactions of both ion pairs and hydrogen bonds (Robetta) (209) or was based on adapted knowledge-based distance-dependent pair potentials (DrugscorePPI) (210). The degree of buriedness analysis indicates the number of atoms within a radius of 4Å of an interfacial residue with a higher score indicating a more buried residue.

6.2.5 Lipid bilayer preparation

Lipid solution was prepared by first dissolving 8 mg of DMPC (1,2-dimyristoyl-sn-glycero-3-phosphocholine) into 8 mL of lipid buffer B (20 mM Tris-HCl, 50 mM NaCl, 1 mM CaCl2, 0.1% (w/v) Triton X-100)(42, 43, 139). A total of 130 uL of TMD-MBP (80 µg/mL) was added to 380 µL of lipid solution and incubated for 2 h at 37ºC. The resulting solution was transferred to a 10 kDa MWCO dialysis cassette and dialyzed three times for 12 h each against 1 L of lipid buffer A (20 mM Tris-HCl, 50 mM NaCl, 1 mM CaCl2) (42, 139). Lipid-protein solutions were then stored at 4ºC in a translucent glass vial under nitrogen for up to one month. The TMD-MBP bilayer was prepared by first plasma cleaning a glass slide for 5 min and immediately submerging it in a solution of 100 ppm polyethyleneimine (PEI) in 0.5 mM KNO_3 for 20 min before rinsing with DI water and drying with nitrogen (42, 139). Slides were further dried in a vacuum desiccator prior to use. Under a slightly dampened towel to prevent complete dehydration the PEI-coated glass slide was incubated with a 4 mL droplet of the lipid-protein solution for 2h. Slides were then rinsed three times in Hank's balanced salt solution (HBSS) before being immersed HBSS prior to force spectroscopy experiments. A PEI-coated glass slide was incubated with only the lipid solution (without the TMD-MBP protein) and used as a negative control to determine the binding specificity as before (139).

6.2.6 Cantilever functionalization

To provide a suitable surface for coating with soluble proteins, molecular force probe cantilevers (Veeco, Plainview, NY) were silanized with 2% (v/v) 3-aminopropyltriethoxysilane in acetone (42, 140). The cantilevers were first incubated in a 30 μg/ml solution of anti-histidine antibody for 30 min before being incubated for 1 h in a 3 mg/mL solution of wild-type or mutated monobody YS1 protein in Dulbecco's PBS containing 50-fold molar excess of the crosslinker bis(sulfosuccinimidyl) suberate (BS3; Pierce, Rockford, IL). The reaction was quenched with Tris buffer. To block nonspecific interactions, cantilevers were incubated in 1% bovine-serum albumin in Dulbecco's PBS. Protein solution concentrations were optimized to result in a low proportion of binding events during force-spectroscopy experiments (~20 binding events per 100 contacts).

6.2.7 Single-molecule force spectroscopy

Force spectroscopy experiments were conducted using a Molecular Force Probe (MFP-1D; Asylum Research, Santa Barbara, CA). Using thermal oscillation method, a triangular cantilever (nominal spring constants of 10 pN/nm) was calibrated, with its deflection measured by laser reflection onto a split photodetector (45, 211). The petri dish containing the MBP-incorporated or blank lipid bilayer slides and Hanks' balanced salt solution buffer was placed on the stage and positioned to be directly below the cantilever. The cantilever height was adjusted such that each approach cycle generated a slight force (~1–2 nN) onto the lipid bilayer before reproach. For each run, reproach velocity was varied from 5 to 25 mm/s, and the dwell time was set to 20 ms (45, 211). Rupture forces and loading rates were calculated from force-versus-distance traces using IgorPro 4.09 software (WaveMetrics, Lake Oswego, OR). The Bell model parameters (k_{off}^{o} and x_{β}) were tabulated using a least-squares fit to the rupture force against the logarithm of loading rate (42, 45, 140). At least four individual experiments and >1000 successful events were run for MBP binding to the wild-type YS1 and the R33A and E47A samples with the exception of the control samples, which were tested by three individual experiments. A new cantilever was freshly prepared, calibrated, and tested for each individual experiment.

6.2.8 Surface plasmon resonance

The binding kinetics between wild-type or mutated monobody YS1 and their target protein MBP were measured using a BIAcore 3000. The running buffer used was

HBS-P at pH 7.4 with 10 mM HEPES, 150 mM NaCl, and 0.005% (v/v) Tween 20 (BIAcore, Piscataway, NJ). A low density of ~200 RU of biotinylated MBP (Avidity, Aurora, CO) was immobilized onto a streptavidin SA chip (BIAcore) to avoid mass-transport limited effect. For binding assays, either wild-type or mutated monobody YS1 protein (0-137 nM) was injected for 100 s at a flow rate of 60 mL/min and followed by washing with buffer for 10 min. Reference curves generated from an uncoated flow cell and multiple injections of running buffer provided a double-reference. The binding sensorgrams were analyzed by the global fitting of 1:1 bimolecular interaction model, and the dissociation equilibrium constant (K_d) was calculated by the dividing k_{on} by k_{off} (212). BIAevaluation 3.0 software (BIAcore) was utilized for data analysis and self-consistency examination was performed as described (213).

6.3 Results

6.3.1 Computational simulations predict R33 and E47 as critical scaffold framework residues

To identify the critical YS1 residues involved in YS1-MBP binding, we first executed a computational alanine-scanning mutagenesis analysis utilizing molecular dynamics and Robetta and DrugScorePPI simulations to analyze the binding interface. Specifically, each of the YS1 interacting residues was individually mutated to alanine. The change in binding free energy ($\Delta\Delta G_{bind}$) and the protein stability of the mutated complex partner in isolation ($\Delta G_{partner}$) were calculated (210, 214). $\Delta G_{partner}$ represents the predicted stabilizing or destabilizing effect of the alanine mutation on free YS1 and is a component of $\Delta\Delta G_{bind}$ with large values signifying decreased YS1 stability and the potential of decreased binding. Additionally, the degree of buriedness was calculated for interfacial residues (210) as a high degree of residue burial is necessary albeit not sufficient for hot spot identification (199). The three calculations were taken together to identify pivotal binding residues.

Simulations predict that YS1-MBP binding hot spots are localized to the FG-loop and the scaffold (Figure 6.1). Amino acids mutations in both the BC-loop and DE-loop were predicted to have an insignificant effect on protein complex stability as alanine mutations in both loops caused minimal negative perturbations of $\Delta\Delta G_{bind}$ (less than about 0.25 kcal/mol) and $\Delta G_{partner}$ (< 0 kcal/mol). Six amino acids in the FG-loop (Y75, Y77, Y78 Y79, Y80 and Y81) and two in the scaffold framework (R33 and E47) were predicted to be important binding residues. The FG-loop amino acids were identified based on their high $\Delta\Delta G_{bind}$ (> 1.5 kcal/mol) or their high $\Delta G_{partner}$ value (> 1 kcal/mol). In a previous experimental alanine-scanning mutagenesis study of the FG loop, the Y75A, Y77, Y78, Y79A, Y80A, Y81A and Y82A mutations caused the largest reduction in affinity (≥ 1.5 kcal/mol) (117). The two scaffold residues were identified based on their high $\Delta G_{partner}$ value (> 1 kcal/mol), their high degree of buriedness (greater than 5.5) and because they had the highest $\Delta\Delta G_{bind}$ of any non-FG- loop residues (Figure 6.1). As common in interfacial hot spots, the residues are grouped in close proximity to one another and make contact with the target protein MBP (Figure 6.2A, B) (198, 199).

Since monobodies feature a structure similar to the antibody variable domain, most YS1 studies focus on the modification of three exposed loops corresponding to the three complementarity determining regions in antibodies (116, 117). Here, we explored the impact of modifications to the R33 and E47 residues, which reside in the C and D β-sheets of the scaffold, respectively. Based on the large value of $\Delta G_{partner}$ (3.04 kcal/mol) and a larger $\Delta\Delta G_{bind}$, we anticipated that R33A mutation would have a greater destabilizing effect on the YS1-MBP interaction than E47A mutations ($\Delta G_{partner}$ 1.04 kcal/mol). We analyzed the effect of these mutations using SMD simulation as well as two biophysical tools: surface plasmon resonance (SPR) and single molecule force spectroscopy.

6.3.2 Use of Steered Molecular Dynamics predicts a crucial role of R33 in scaffold stabilization

SMD simulations were performed using six randomly selected pairs of monobody-MBP complexes at equilibrium. Pulling was performed at a constant speed of 10 Å/ns with a spring stiffness of 70 pN/Å on residue V72 of the monobody and was designed to pull the monobody away from the center of mass of MBP. Water molecules were simulated by the generalized born implicit solvent (GBIS) model implemented in NAMD. Each simulation lasted 4 ns with data points saved every 0.5 ps for analysis. SMD enabled the quantification of the contribution of each residue to the YS1-MBP binding interaction (197).

In order to reduce computational time we utilized the generalized born implicit solvent in NAMD for water modeling. The GBIS electrostatics calculation first determines and then utilizes the Born radius of each atom to quantify the atom's exposure to solvent and its dielectric screening from other atoms. GBIS simulations of the repulsive and the attractive components of the nonpolar solvation free energy of small molecules are in agreement with explicit models (215). NAMD's GBIS capability has been utilized for simulating several large protein structures (216, 217) and validated for the simulation of a ribosome undergoing two major conformational changes (207). In this instance, GBIS and TIP3P explicit solvent structures closely agree, with a root-mean-square deviation between models of 1.5 Å (207).

The mechanics of bond rupture can be separated into three distinct regions (Figure 6.3B). First, as the pulling force increases linearly, the number of hydrogen bonds remains relatively constant. As the applied force reaches the rupture force the hydrogen bonds begin to break one by one. When all bonds have broken and YS1 and MBP are completely dissociated, the force reaches background levels. The lifetimes of hydrogen bonds involving specific residues of the YS1 scaffold are comparable to those of the FG loop (Figure 6.3D). Thus, predictions from SMD simulations indicating the importance of scaffold residues in the YS1-MBP interaction are in line with the findings from computational alanine-scanning mutagenesis.

Destabilizing mutations, which decrease bond duration time between the interacting residues in the presence of force, reduce the overall interaction time between YS1 and its ligand, thereby indicating weaker binding. Based on the SMD simulation, the E47A mutation reduces the interaction lifetime between the YS1 and MBP by 30% and causes the hydrogen bonds to break earlier and at a faster rate (Figure 6.4A, B). Coupled with the moderate decrease in binding force, this result suggests that the E47A mutation decreases the overall strength of the interaction. The R33A mutation has a more profound effect than E47A, reducing the overall bond lifetime by 50% and the binding force by ~30% (Figure 6.4D, E). Both E47A and R33A mutations have little effect on the duration of hydrogen bonds involving residues of the monobody loops. Instead, they affect the duration of hydrogen bonds between the monobody scaffold residues and MBP (Fig 4.c, f). The E47A mutation decreases hydrogen bond duration in the E47 residue alone, and has little effect on the other scaffold residues, likely resulting in the modest decrease in the overall YS1-MBP bond duration observed with the E47A mutation. In contrast, the R33A mutation not only reduces the duration of the hydrogen bond at R33 but also at the other interacting residues of the scaffold (Figure 6.4F). Consequently, this mutation substantially destabilizes the bond and results in a more significant loss of intermolecular recognition. This destabilization and subsequent synergistic bond weakening likely contributes to the larger $\Delta\Delta G_{bind}$ and $\Delta G_{partner}$ predicted in the computational alanine-scanning mutagenesis analysis and further supports a major role for R33 in the YS1-MBP interaction.

6.3.3 Single-molecule force spectroscopy supports the role of E47 and R33 in YS1-MBP interaction

Single-molecule force spectroscopy was utilized to characterize the binding kinetics of the R33A and E47A mutant variants of YS1 with MBP. MBP was properly oriented in a lipid bilayer via an attached transmembrane domain from the human CD44 transmembrane protein as in our previous study of the interaction of MBP with a DARPin (139). YS1, YS1(E47A), and YS1(R33A) coated cantilevers were brought in contact with MBP for a constant dwell time and retracted at a predetermined retraction speed. The tensile strength of the bond (bond rupture force) and loading rates of single binding events were recorded over a range of retraction velocities (42, 139). The concentrations of YS1 on the cantilever and MBP in the lipid bilayer were selected to yield a binding event percentage of ~20% (Figure 6.5A) as this frequency will ensure that the majority of binding events (>89%) are caused from the breakage of single bonds (based on the Poisson distribution) (42, 140).

The tensile strength measured for YS1 binding to MBP was in the range of 35-80 pN over a wide range of loading rates (Figure 6.5B). The E47A mutation reduces the rupture force by approximately 10-15 pN over a similar range of loading rates, indicating that the E47 residue plays an auxiliary role in this interaction. Using the Bell model (127), the values for the unstressed off-rate k_{off}^{o} (second^{-1}**)** and reactive compliance x_{β} (nm) for YS1(E47A) were determined by plotting mean rupture force against the logarithm of the loading rate and fitting the data with a least-squares regression line (Figure 6.5B). The E47A mutant increased k_{off}^{o} of the binding interaction 3-fold compared to the YS1 (Table 6.1). Larger values of k_{off}^{o} are indicative of shorter unstressed bond lifetime and weaker binding. Interestingly the reactive compliance, which reflects the susceptibility of the bond to rupture under stress, was similar for both the wild-type and mutant monobodies. In accordance with the Bell Model (127), an applied force (*f*) will alter the bond off rate (k_{off}) by the following equation: k_{off}/k_{off}^{o} = exp($fx_{\beta}/k_{B}T$). Therefore, the similar x_{β} values observed here and in other studies (139) indicate a similar sensitivity to rupture in the presence of force. Collectively, the E47A mutation decreases the strength of the YS1-MBP bond as indicated by its lower tensile stress and shorter unstressed bond lifetime.

In concert with both scanning alanine mutagenesis and SMD simulations, force-spectroscopy also revealed that the R33A mutation had a pronounced destabilizing effect on the monobody-MBP interaction, as evidenced by the dramatic decrease in binding frequency down to basal levels (Figure 6.5A). Of note, the auxiliary role of the E47A mutation is further substantiated by our findings showing that this mutation did not significantly affect binding frequency of monobody-MBP interaction (Figure 6.5A).

6.3.4 Surface Plasmon Resonance confirms that the pivotal role of the scaffold residue R33 in YS1-MBP interaction

SPR experiments were performed to determine the binding kinetic constants (K_d, k_{on}, k_{off}). YS1, YS1(R33A), and YS1(E47A) were flowed over a chip sensor coated with biotinylated MBP (Figure 6.6). In accordance with the single molecule force spectroscopy results, the R33A mutation reduced the binding signal to non-significant levels, further demonstrating the critical role of R33 in the YS1-MBP interaction. Binding of MBP to both YS1 and YS1(E47A) fit a 1:1 binding model and had equivalent K_d values of about 100 nM (Table 6.1). The E47A mutation resulted in no significant change in k_{off} or k_{on}. The similar kinetic constants found here are consistent with the similar binding frequency detected between MBP and YS1 or YS1(E47A) using single-molecule force spectroscopy. The discrepancy in the dissociation rate constants obtained by SPR versus force spectroscopy between YS1-MBP and YS1(E47A)-MBP binding is likely due to differences in binding geometries (3D vs. 2D) (139). Overall, SPR data correlate well with both SMD simulations and single-molecule force spectroscopy data and indicate the R33A mutation substantially destabilizes YS1-MBP binding while the E47A mutation plays a less important role.

6.4 Discussion

A better understanding of how monobodies associate with their ligands will facilitate the development of robust binding pockets for higher affinity recognition and allow for the generation of improved monobodies. We used computational alanine-scanning mutagenesis, SMD, single-molecule force spectroscopy and SPR to identify and characterize the effect of monobody scaffold residues on the binding interaction between monobody YS1 and MBP. Molecular simulations identified E47 and R33 as scaffold residues that contribute to monobody-MBP recognition. Mutation at E47 resulted in a weaker bond and reduced interaction duration, thereby suggesting an auxiliary role for E47 in monobody-MBP recognition. On the other hand, the R33 residue plays a key role in this interaction as R33A mutation abrogated binding in both experimental assays, an effect likely caused by the synergistic destabilization of the interacting scaffold residues (Figure 6.4F).

Our K_d value for YS1-MBP binding obtained by SPR falls between the reported values of 73 nM and 135 nM of prior work, which also used SPR (116, 117). Those studies and ours indicate 1:1 binding kinetics. Previous mutagenesis work combined shotgun scanning mutagenesis with alanine-scanning mutagenesis for an analysis of YS1-MBP binding, but focused only on the BC and FG loops (117). That study concluded that the BC loop of YS1 is robust to mutation whereas the FG is sensitive (117). A similar trend was also observed in our *in situ* scanning alanine analysis (Figure 6.1), where DrugScorePPI predicts the interfacial FG loop residues that were most important for the interaction (116).

Although previous studies have primarily focused on varying loop residues to achieve higher binding affinities, recent work has demonstrated the importance of monobody scaffold residues in binding (119, 218). Interactions between monobodies and small ubiquitin-related modifier (SUMO) proteins were found to rely heavily on both FG loop and scaffold binding, and scaffold modifications were required to generate the desired isoform specificity of the monobody (119). A focus on scaffold residue diversity has generated monobodies capable of binding to the Abl SH2 domain with low nanomolar affinities due primarily to scaffold binding (218). Koide et al. noted that the scaffold interactions found in the YS1-MBP crystal structure were possibly due to the lattice packing because the contacts were polar and charged and the region showed little to no chemical shift perturbation in an NMR study (117). However, R33 has been a point of interest in several monobody studies. R33 was found at multiple binding interfaces, and its mutation has led to either increased or deceased binding strength when coupled with additional scaffold and loop amino acid modifications (119, 218). In our study, molecular dynamics simulations, single-molecule force spectroscopy and SPR studies indicate that R33 is critical for the YS1-MBP interaction.

Hot spots in natural proteins tend to have nonrandom compositions with the second most abundant amino acid being arginine (199, 219). Its presence at hot spots is thought to occur due to its ability to form several favorable interactions including electron delocalization through the guanidinium motif and the ability to form up to five hydrogen bonds (199). As predicted by DrugscorePPI scanning alanine mutagenesis and exemplified in both SPR and force spectroscopy experiments, the R33A mutation was shown to destabilize YS1-MBP binding. Robetta predictions indicated the R33A mutation decreases YS1 stability, a result that likely contributes to the loss of intermolecular recognition in the biophysical assays. R33 is at the center of the scaffold interface (Figure 6.7C, D). The equilibrated molecular representation of the binding interface (Figure 6.7E, F) shows R33 of YS1 stacking with R344 of MBP effectively burying both arginines. Arg-Arg stacking has been observed in numerous protein-protein interfaces although the reason for its occurrence is not yet fully understood (220, 221). Arginine stacking is thought to drive the formation of protein interfaces, primarily through polarization effects resulting in the seclusion of solvent however, both hydrophobic and electrostatic-solvation effects can play secondary roles (220). Arg-Arg stacking has been observed in MD simulations using both explicit and implicit water models and alternate force fields (222, 223). In YS1-MBP binding the two positively charged guanidinium groups stack parallel to one another in a form between the staggered and eclipsed conformations. This interaction appears to be vital for high MBP affinity.

SMD simulations (Figure 6.4F) reveal the R33A mutation reduces the hydrogen bond duration of surrounding interacting residues of the scaffold. Hydrogen bonding between R33 and E47 allows E47 to hydrogen bond effectively with the R344 residue of MBP (Figure 6.7E, F). The stability of this interaction contributes to the lengthy bond duration of E47 and MBP (Figure 6.3D). A similar effect can be found in ySMB-1 binding to ySUMO where polar interactions between arginine and asparagine appear to stabilize glutamic acid to construct a robust scaffold interaction (119). Although additional interacting scaffold residues form hydrogen bonds with durations comparable to R33, alanine mutations here were not predicted to critically destabilize the binding interface. These residues are less buried than either R33 or E47 (Figure 6.1C) and further away from the R33 residue such that alanine mutations here are not likely to critically destabilize the interface. In fact, although the E47A mutation alters the binding interface modestly, the mutation was not predicted to disrupt the stacking effect (Figure 6.8). In our work, the R33 residue exhibits two critical characteristics: it anchors the scaffold to MBP via arginine stacking and establishes hydrogen bonding between the YS1 scaffold and MBP. Without the stabilization of the arginine stacking, the R33A mutation has a noticeable and unfavorable conformational change in both YS1 and MBP upon binding (Figure 6.7B).

In summary, we have elucidated the importance of the scaffold interaction in YS1-MBP binding through a systematic approach involving molecular modeling and biophysical analyses. Our results further illustrate the importance of the R33 scaffold residue in monobody-target binding, thus providing vital knowledge for the improved engineering of monobodies.

6.5 Tables and Figures

	DrugscorePPI	Robetta	Single-molecule force spectroscopy		Suface plamon resonance		
sample	$\Delta\Delta G_{bind}$ (kcal/mol)	$\Delta\Delta G_{partner}$ (kcal/mol)	k^{o}_{off} ($\times$ $10^{-3}s^{-1}$)	x_{β}(nm)	k_{on}($\times$ $10^{5}M^{-1}s^{-1}$)	k^{o}_{off} ($\times$ $10^{-3}s^{-1}$)	K_d (nM)
Wild-type			0.24 ± .06	0.42 ± .03	4.4 ± 0.7	40.6 ± 3.2	100 ± 18
E47A	.53 ± .03	1.01 ± .18	0.76 ± .39	0.46 ± .05	3.6 ± 0.3	38.7 ± 15	101 ± 41
R33A	.67 ± .06	3.04 ± .44	N.B.	—	N.B.	—	—

Table 6. 1 Comparison of experimentally determined kinetic constants for mutations at critical scaffold residues as determined by scanning alanine mutagenesis simulations.

N.B. represents no binding. This No binding is defined as having a binding frequency under 5% for single molecule force spectroscopy or displaying an <5 RU response up to 1 μM concentration in SPR. Data represent the mean ± s.e.m. of at least three independent experiments.

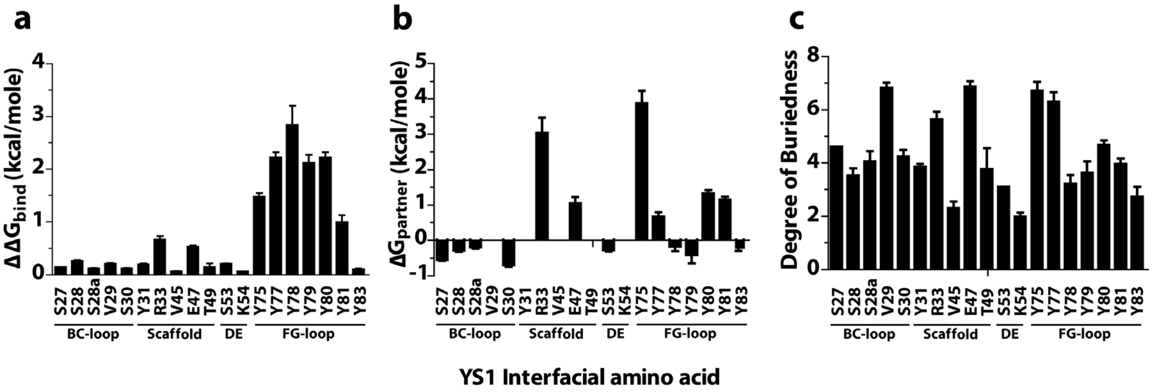

Figure 6. 1 Computational simulations predict the critical residues of YS1 at the YS1-MBP binding interface.

(a) DrugscorePPI webserver prediction of changes in binding free energy ($\Delta\Delta G_{bind}$) upon alanine mutation. (b) Robetta prediction of the effect of alanine mutation on mutated protein complex partner in isolation ($\Delta G_{partner}$). Residues V29, Y31, V45, T49 and K54 were omitted as Robetta predictions failed to identify them as being present in 50% of the predicted binding complexes. (c) DrugscorePPI webserver prediction of the degree of buriedness of the interfacial residues at the YS1-MBP interface. Results are the mean ± s.e.m. of 6-8 pairs of randomly selected monobody-MBP complexes.

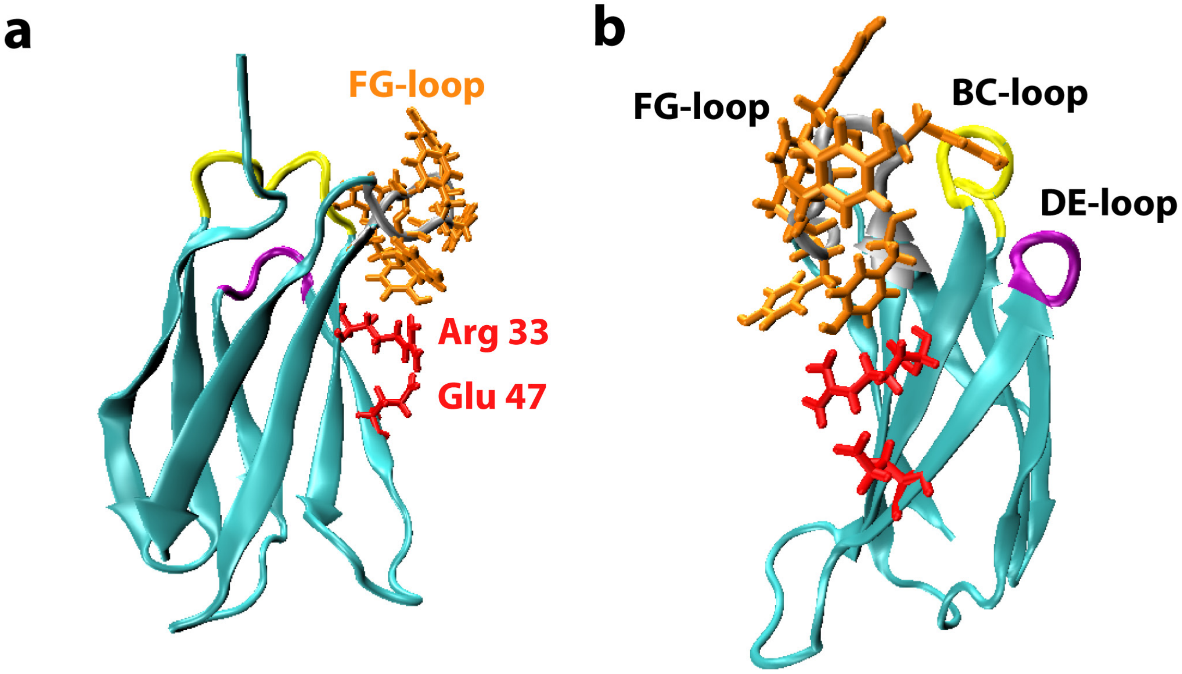

Figure 6. 2 Two perpendicular views of the crystal structure of monobody YS1 (cyan).

DrugscorePPI simulation predicted that binding energy between YS1 and its target MBP is provided by two groups of interfacial residues: Tyr75, Tyr77, Try78, Try79, Tyr80 and Y81 (orange) which are located in the FG-loop; and Arg33 and Glu47 (red) which belong to the framework of the scaffold. The PDB ID is 2OBG. The figure was made with the software VMD (DeLano Scientific, San Francisco, CA).

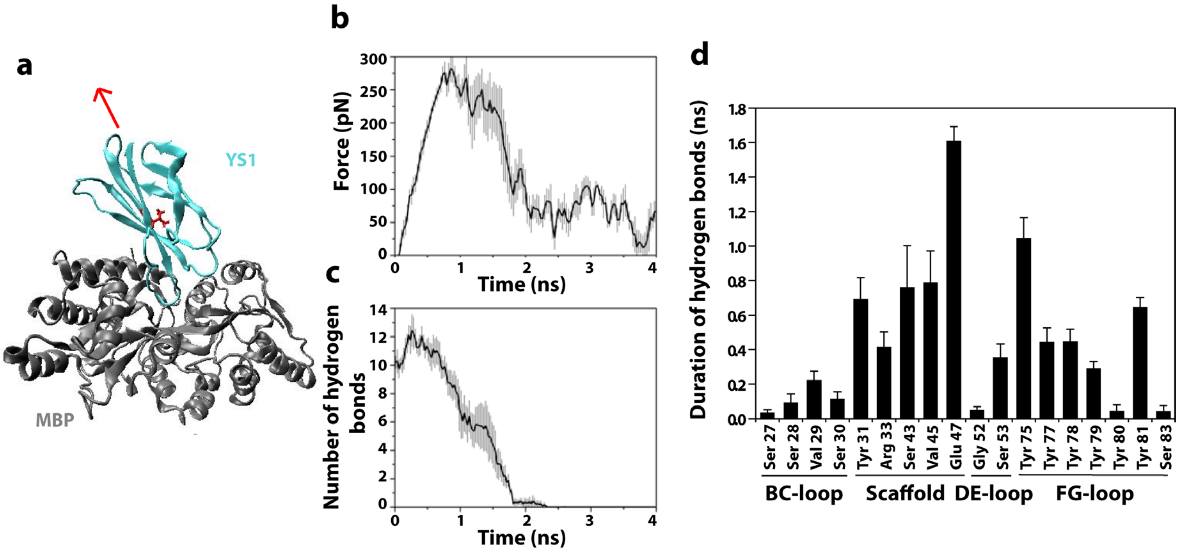

Figure 6. 3 Steered molecular dynamics (SMD) simulates the unbinding of monobody YS1 from its target MBP.

(a) A schematic illustration showing the monobody YS1 (cyan) being pulled away from MBP (grey) under a constant pulling velocity on Val72, which is indicated in red. The retracting direction was selected to pull the center of mass of the monobody away from that of MBP as indicated by the red arrow. (b) Force-time course of SMD simulated unbinding of monobody YS1 from its target MBP. (c) The time evolution of the average number of hydrogen bonds and (d) hydrogen bond duration measured for each interacting residue between monobody YS1 and MBP during unbinding simulations.

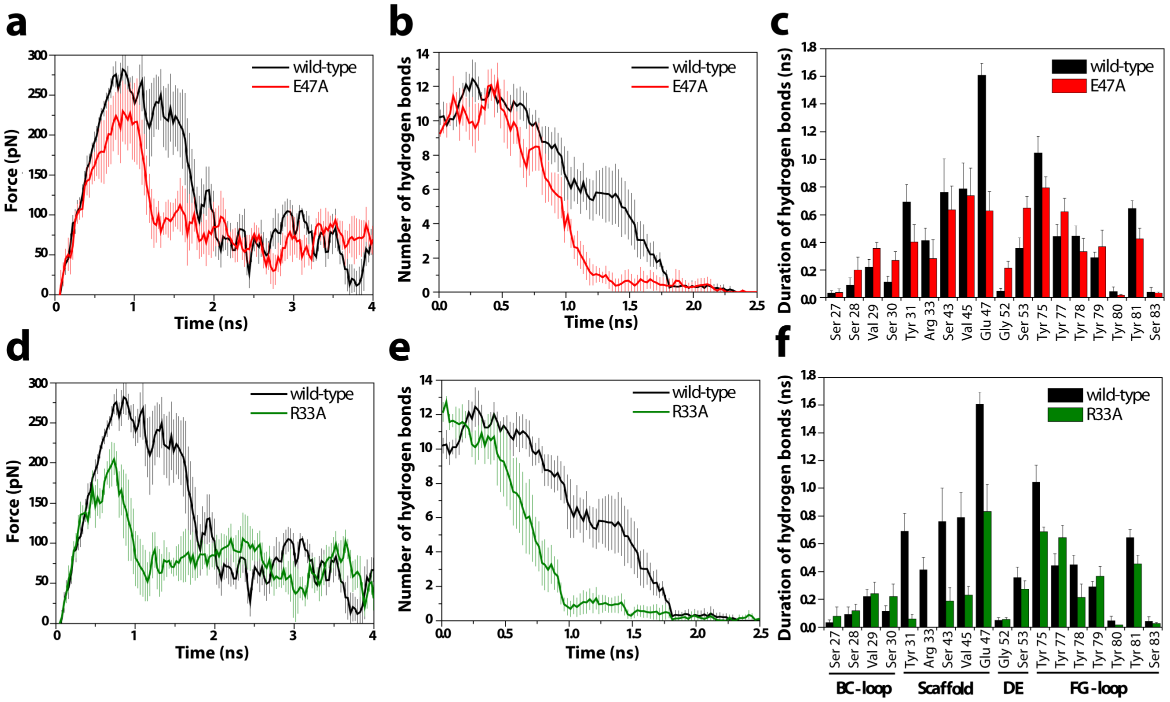

Figure 6. 4 Steered molecular dynamics simulations of unbinding of (a-c) E47A and (d-f) R33A mutants from the target MBP.

Equilibrated mutant YS1-MBP pairs were pulled apart at a constant speed and spring stiffness. During the dissociation event, (a and d) pulling force, (b and e) the number of hydrogen bonds between interacting residues, and (c and f) the duration of hydrogen bonds for each interacting residue were determined for both mutants. Results are the mean ± s.e.m. of six pairs of randomly selected monobody-MBP complexes.

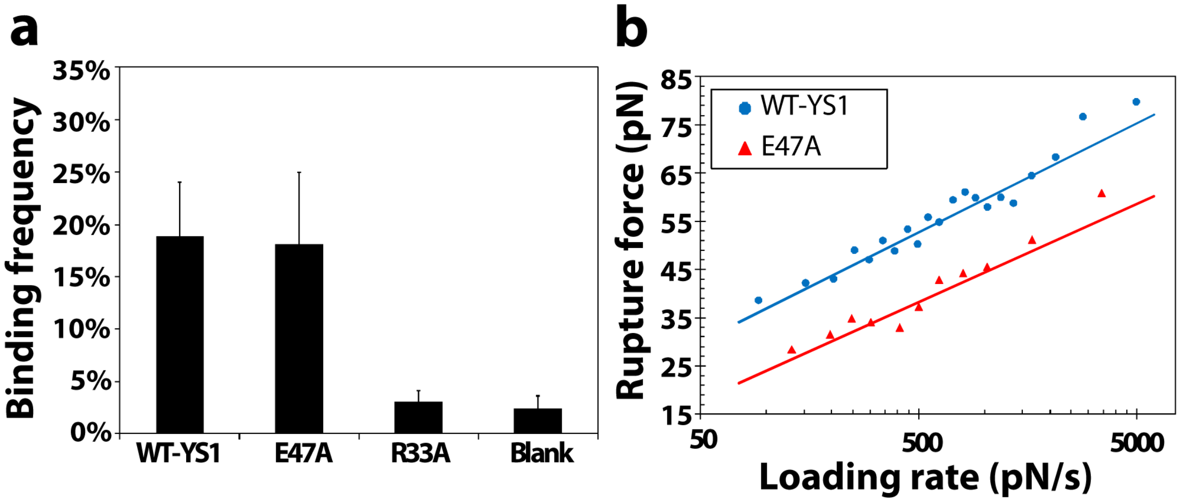

Figure 6. 5 Characterization of the kinetic and micromechanical properties of monobody YS1 binding to MBP using single-molecule force spectroscopy.

(a) Frequency of binding events between MBP and YS1, YS1(E47A) or YS1(E33A). The last column (blank) represents a control experiment using a blank bilayer. Data represent the mean ± s.e.m. of at least three independent experiments. (b) Rupture force as a function of loading rate for the binding of YS1 (black circles) and YS1(E47A) (red triangles) to MBP. The lines are a nonlinear least-squares fitting of the Bell dissociation model for determining the unstressed off-rate (k^0_{off}) and reactive compliance (x_β) of a bond.

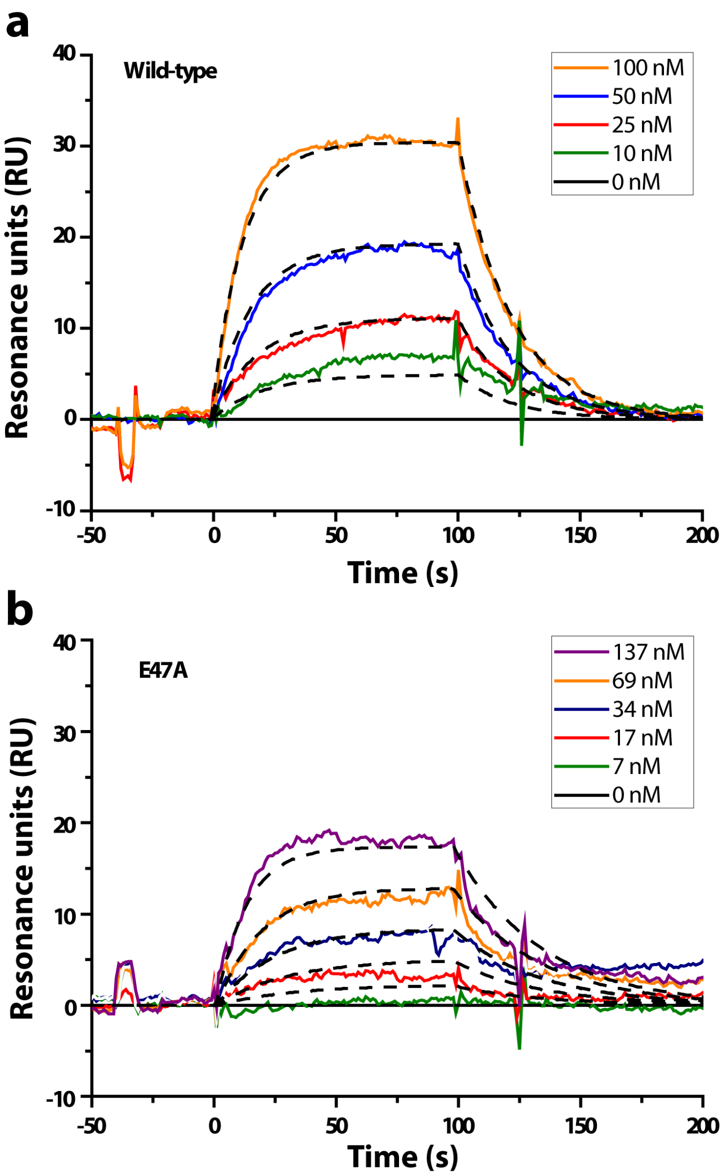

Figure 6. 6 Binding interactions of monobodies and MBP analyzed using SPR.

Representative sensograms were generated by perfusing (a) wild-type YS1 or (b) YS1(E47A) over biotinylated MBP immobilized SA chip at concentrations ranging from 0-137 nM for 100 seconds, followed by washing with buffer for 10 minutes. To generate the k_{on}, k_{off} and K_{d} a 1:1 Langmuir binding model was fit for YS1- and YS1(E47A) -MBP interaction. χ^2 vales were 0.88 and 1.92 for YS1 and YS1(E47A), respectively. Data were analyzed using BIAevaluation 3.0 (BIAcore).

Figure 6. 7 YS1 scaffold residues at the MBP interface.

The interacting scaffold residues of (a) YS1 and (b) YS1(R33A) (both shown in yellow). The BC, DE and FG loops are represented orange, green, and red, respectively (c) Schematic illustration of the YS1-MBP interaction and (d) YS1 in which R33, E47, Y75, Y77, Y78 Y79, Y80 and Y81 are shown in red and the other interfacial residues of YS1 are shown in yellow. The side view (e) of the YS1 (yellow) and MBP (cyan) interface shows R33 of YS1 stacking with R344 of MBP to establish the hydrogen bond network between R33, E47, and R344. The top view (f) displays the arginines stacking. Schematic illustration of YS1-MBP interfacial interaction made using the equilibrated molecular representation based on the crystal structure (PDB ID: 2OBG) (116) and with the software VMD (DeLano Scientific, San Francisco, CA).

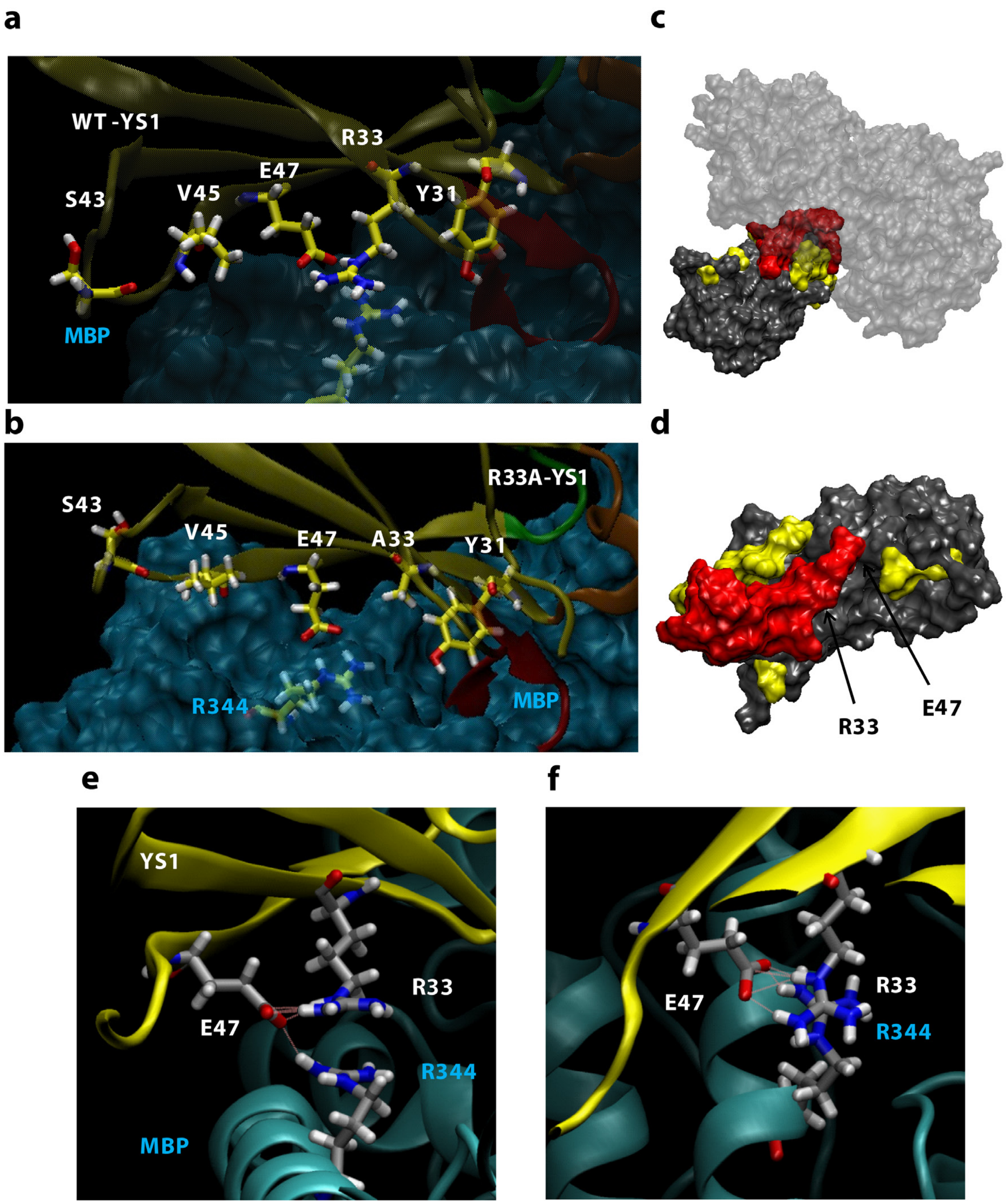
a
WT -YS1
R33
E47
S43
V45
Y31
MBP
c
b
R33A-YS1
S43
V45
E47
A33
Y31
R344
MBP
d
R33
E47
e
YS1
R33
E47
R344
MBP
f
E47
R33
R344

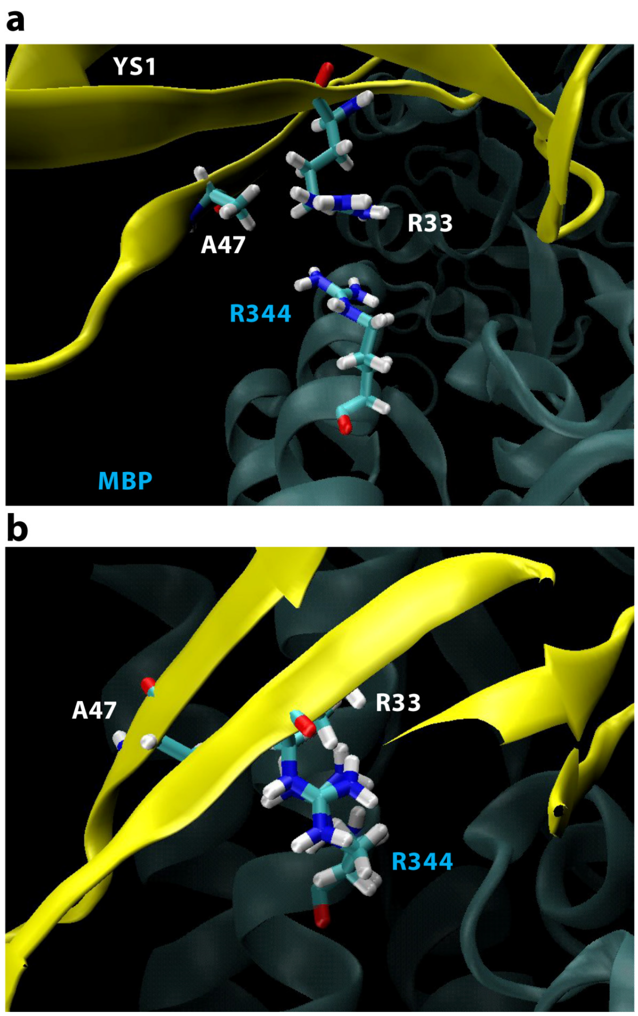

Figure 6. 8 Two perpendicular views of the YS1(E47A)-MBP interface showing Arg-Arg stacking.

The side view (a) of the YS1 (yellow) and MBP (cyan) interface shows R33 of YS1 stacking with R344 of MBP in the presence of the E47A mutation. The top view (a) displays the arginines stacking. Schematic illustration of YS1(E47A)-MBP interfacial interaction made using the equilibrated molecular representation based on the crystal structure (PDB ID: 2OBG) and with the software VMD (DeLano Scientific, San Francisco, CA).

Chapter 7

CONCLUSIONS AND FUTURE DIRECTIONS

7.1 Distinct kinetic and mechanical properties govern mucin 16- and podocalyxin-mediated tumor cell adhesion to E- and L-selectin in shear flow

In Chapter 3 we utilized both single-molecule bond characterization and microfluidic assays along with a mathematical model (discussed in detail in Chapter 2) to characterize ligand-dependent tethering and rolling in physiologically relevant flow conditions. We found that a series of factors including the single-molecule kinetic and micromechanical properties and the number of bonds needed for tethering can predict the binding and rolling interactions of MUC16- and PODXL-coated microspheres on E-/L-selectin coated surfaces. This integrated approach can lead to a better understanding of how MUC16 and PODXL bind to E-/L-selectins in physiologically relevant hydrodynamic shear. This can lead to the production of improved diagnostic assays and to the prevention of pancreatic metastasis.

However, one must note that these results were obtained through ligand-coated microspheres interacting with selectin coated surfaces, which are not as physiologically relevant as cell-ligand or cell-cell interaction. In this study ligand-receptor interactions were studied because it is easier to obtain kinetic and micromechanical properties without the confounding affects associated with cell-cell or cell-receptor interactions. In these interactions, cell deformability, ligand density and orientation can affect cell binding

(27). For this study we wanted to eliminate these confounding affects, and hence used the present system. However, in our second study we expand upon this work and used PODXL and MUC16 expressing Pa03c cells, assessing cell binding to receptor coated glass surfaces.

7.2 E-selectin mediated rolling increases pancreatic tumor cell adhesion to hyaluronic acid

In Chapter 4 we demonstrate that pancreatic tumor cell rolling on E-selectin promotes adhesion to HA. Cells rolling on E-selectin were approximately 40X more likely to bind to HA than non-rolling cells at both low and high shear stresses. The knockdown of PODXL attenuates rolling on E-selectin but does not decrease the rate of adhesion on HA once cells have rolled. This approach uncovers the physical interdependence of the MUC16/PODXL-E-selectin and CD44v-HA bonds and uncovers the critical parameters involved in cell-receptor binding. This knowledge can be utilized to improved diagnostic assays and better understand the metastatic spread of pancreatic tumor cells.

This study explores how pancreatic tumor cells that express PODXL, MUC16 and CD44v bind to E-selectin and subsequently to HA in shear flow. In the future we would like to take this project in several different directions, with one direction being to decouple the binding interactions further. By using cell lines that have been knocked down for MUC16 or CD44 in addition to PODXL, we could further assess how these binding interaction influence cell rolling and firm adhesion. In Chapter 3 we observed differences between PODXL and MUC16 rolling and tethering to E- and L-selectin. It would be prudent to see if these differences persist in a cell-receptor system. A second direction would be to couple the interactions further and observed how pancreatic cancer cells roll and adhere to both E-selectin and HA where the two proteins are patterned together, rather than in distinct regions. E-selectin has been patterned with an anti-EpCAM antibody to capture CTCs while excluding the leukocytes (161). This technique could be modified to pattern multiple proteins on a surface in order to capture pancreatic tumor cells in geometrically defined regions. In this setup we wouldn't be observing how rolling on E-selectin affects binding to HA alone but rather observe binding in a more representative and physiological relevant ECM. This work would translate nicely into studying cell-cell interactions where pancreatic tumor cells can be flowed over activated endothelial cells expressing relevant cell-surface proteins. One proposed method to do this is discussed in the next section.

Next we would like to investigate how PODXL and MUC16 affect metastasis in vivo. While we have yet to extensively explore MUC16 as a metastasis driver in pancreatic cancer there are early indications that the loss of PODXL decreases cell migration in vitro and tumor formation in vivo in a subcutaneous model (Figure 7.1). However, while the subcutaneous tumor model is straightforward and easy to use, it is unable to recapitulate the tumor microenvironment and as a result tumors are unable to progress and metastasize in a manner similar to human cancers (224). Therefore, we have also begun experiments looking at the metastasis of PODXL expressing and PODXL-KD pancreatic cancer cell lines.

These experiments include the orthotopic implantation and hemispleen models. For the orthotopic model, PODXL expressing and PODXL-KD Pa03c and SW1990 cells, which are prepared either in matrigel or as 1mm^3 sections of a subQ tumors are implanted into the pancreas of NOD/SCID mice. The mice are then monitored and their survival can be measured (224). At a set end date the remaining mice can be sacrificed and cell metastasis to the liver and other organs can be measured via H&E staining of organ cross sections or through hline-1 analysis of human DNA in these organs. Further, the growth of the tumor in the pancreas can also be measured.

We have also begun to study metastasis through a preclinical, murine pancreatic tumor model of hepatic metastases, which takes advantage of a tumor cell injection into the hemispleen. In this model the spleen of the NOD/SCID mouse is divided and Pa03c or SW1990 tumor cells are injected slowly and washed with PBS (225). This allows cells to pass through the circulatory system directly to the liver, mimicking the path that metastatic pancreatic tumor cells would travel in the vasculature. The hemispleen model results in liver metastasis 100% of the time (225). However, while the orthotopic implantation can model the entire metastatic cascade the hemispleen model captures just the final steps of the metastatic process, including cell rolling and adhesion, extravasation, and colonization. However, this model remains more accurate than the tail vein injection for pancreatic cells because in the tail vein model, cells metastasize primarily to the lungs rather than the liver.

We would expect that PODXL expressing SW1990 and Pa03c cells metastasize more easily in the orthotopic and hemispleen models, and mice treated with these cells would develop increased liver metastasis compared to PODXL-KD cells. Because control SW1990 and Pa03c have an increased ability to bind to E-selectin and firmly adhere to HA coupled with an increased ability to migrate in vitro and initiate tumors in vivo, they should display increased metastasis in these two models.

7.3 Binding and migration of glial-restricted progenitor (GRP) cells in vitro, validated through in vivo models

The loss of oligodendrocytes after stroke is one of the main causes of secondary neuron injury. GRPs have local re-myelinating potential after transplantation into the brain however, they express low levels of VLA-4 and therefore flow quickly through the brain vasculature and are cleared from the body when implanted through intraarterial methods. Therefore we overexpressed VLA-4 in GRP cells to see if we could improve endothelial binding and migration in vitro and cerebral homing in the middle cerebral artery occlusion (MCAO) stroke model.

In this regard we designed a flowchamber that could either be coated with purified VCAM-1 or brain endothelial cells (Figure 7.2A). We observed that GRPs expressing VLA-4 bound to both a VCAM-1 coated glass and activated brain endothelium with a significantly higher frequency than control GRP cells (Figure 7.2B). GRPs expressing VLA-4 cells also rolled with slower velocities on both surfaces. Further in vitro microchannel migration assays showed that GRPs expressing VLA-4 migrate faster and further through both confined and unconfined channels (Figure 7.2C and D). Taken together GRPs expressing VLA-4 should initiate binding and homing to brain endothelium in vivo.

Using the middle cerebral artery occlusion (MCAO) stroke model and intraarterial infusion imaged with two-photon microscopy we observed that GRPs with VLA-4 adhered to blood vessel walls in three-fold greater numbers than control GRPs. Furthermore migration through the vessel walls was observed for GRPs with VLA4, but not control GRPs (Figure 7.2F and G). Taken together this data demonstrates (1) that in vitro binding assays such as the flowchamber developed for this study can replicate in vivo observations. Here were observed a trend in rolling speed and binding frequency, which was preserved from the cell-receptor to the cell-cell level in vitro and eventually to the cell-cell level in vivo. (2) That observations in cell migration using in vitro microchannels directly translate to an in vivo setting. This further validates these techniques as they translate well to clinically and physiologically relevant applications.

7.4 Loss of obscurin from human pancreatic ductal epithelial cells increases cell migration and dynamics

In Chapter 5 we observed that giant obscurins are depleted from PDAC tissue and metastatic cell lines, but they are abundant in normal pancreatic tissue and non-tumorigenic human pancreatic ductal epithelial (HPDE) cells. Further, the loss of obscurin from HPDE cells results in the modification of two major pathways, RhoA and PI3K/AKT which in turn leads to major alterations of the cytoskeleton including faster actin dynamics at cell-cell junctions, increased microtubule dynamics and decreased focal adhesion density. This in part leads to increased cell migration speeds through trifurcating channels. This is critically important because identifying markers that encourage tumor growth and metastasis is vital to the prevention and treatment of pancreatic cancer.

Similar to our approach with the PODXL expressing cells we plan to see how the losses of giant obscurins affect tumor formation and metastasis in vivo. Because the loss of obscurins in Panc5.04 is correlated with increased PI3K activity as well as increased cell motility and cytoskeletal cell dynamics in vitro, we plan to examine the effects of obscurin depletion on tumorigenicity in vivo, considering upregulated PI3K activity can result in increased pancreatic tumor cell survival and growth in vivo (177). The Panc5.04 cell line was chosen for this work because the HPDE are nontumorigenic in vivo (226). In this regard plan to observed the formation of tumors for Panc5.04 ctrl-shRNA and obscn-shRNA in a subcutaneous model. We expect, that similar to obscurin depleted breast epithelial cells, (91) obscurin-KD pancreatic cells will grow faster and form larger tumors than control cells. If these results match our hypothesis, we will move forward with PI3K inhibitor in vivo studies, where we will observe the effects of treating obscurin depleted pancreatic tumors with the PI3K inhibitor BKM120 in a subQ mouse model.

Furthermore because we observe increased cell migration and dynamics for both HPDE and Panc5.04 depleted for giant obscurins we would like to study if these alterations affect metastasis in vivo. Again we would utilize the orthotopic implantation and hemispleen models to assess cell metastasis. In both instances increases in metastasis would tie more directly to increases in cell migration (intravasation and extravasation), survival and growth rather than cell binding in flow (although the loss of obscurin can increase microtentacle formation (ref 86).

7.5 Characterization of Monobody Scaffold Interactions with Ligand via Force Spectroscopy and Steered Molecular Dynamics

In Chapter 6 we identified two scaffold residues (E47 and R33) that are critical to the binding interaction between the monobody YS1 and its ligand, maltose-binding protein using alanine-scanning mutagenesis. Through steered molecular dynamics simulations we predicted that alanine mutations to these residues in the YS1 scaffold would destabilize the YS1-MBP interface by reducing the bond rupture force and the lifetime of hydrogen bonds. Simulating the unbinding event indicated that the R33A mutation weakens binding between all scaffold residues and MBP and not just between R33 and MBP. We validated these simulations using single-molecule force spectroscopy and surface plasmon resonance. We propose that interfacial stability resulting from arginine-arginine stacking, which synergistically stabilizes both the arginine-arginine bonds and entire interacting scaffold residues of YS1. Our integrated approach improves the understanding of the monobody scaffold interactions with a target, thus providing guidance for the improved engineering of monobodies.

With increased knowledge about the binding interface of conserved scaffold residues of monobodies, it is not unreasonable to believe that this can contribute to their improved design. Interestingly while Arg-Arg stacking has been observed in multiple protein-protein interfaces although it is not yet fully understood (220, 221). What is known is that this interaction appears to be vital for high MBP affinity and may be critical for other monobody binding interfaces. In fact the R33 was found at multiple monobody interfaces for different binding interactions, and mutations here have led to either increased or decreased binding strength when coinciding with additional scaffold and loop modifications (119, 218).

Moving forward it would be interesting to use phage or yeast display combinatorial libraries to develop monobodies that could bind with high specificity and affinity to pancreatic cancer surface proteins like MUC16 and PODXL. Recently, monobodies have been engineered to fight cancer. Monobody NS1 was designed to bind to H- and K-RAS proteins and inactivate the RAF dimer leading to changes in cell cycle progression (123). Additionally monobodies have been designed to bind to the Src homology 2 domain at the phosphotyosine-binding site effectively inhibiting Bcr-Abl kinase activity resulting in the cell death of chronic myelogenous leukemia cell lines in vitro (219). Therefore it is clearly possible to design monobodies to bind to and inhibit the functionality PODXL or MUC16, or bind to obscurin at the Rho-GEF or PH domains to inhibit the activation of the RhoA or PI3K/AKT pathway. Because minor improvements in treating cancer metastasis can have major benefits, targeting these interactions may prove worthwhile.

7.6 Figures

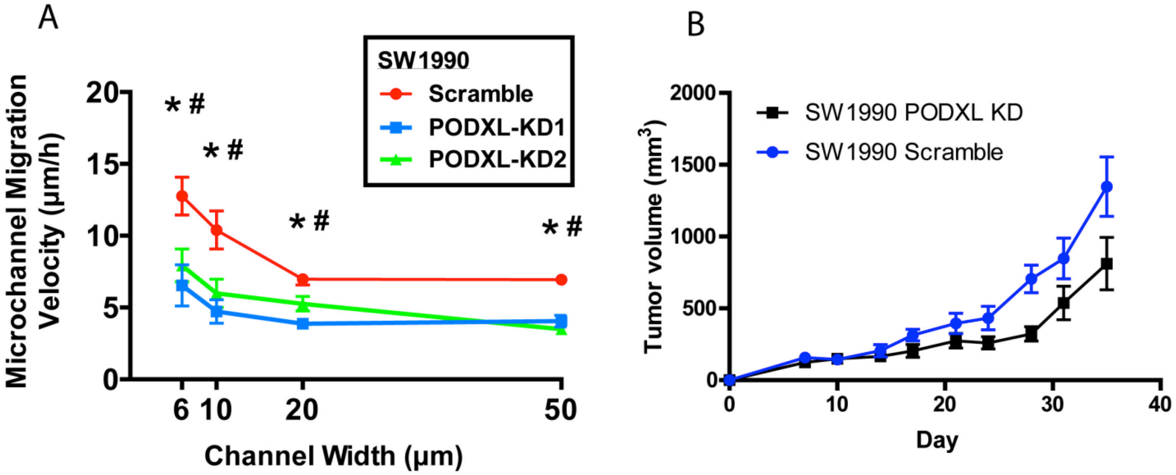

Figure 7. 1 Migration and tumorigenicity is reduced in PODXL-KD SW1990 cells. **(A)** SW1990 cells with either scramble control or PODXL-KD shRNA were allowed to migrated through straight microchannels with widths varying from 6 to 50μm, under a gradient of 10% FBS. Scramble control cells migrated with faster velocity through both confined and unconfined microchannels when compared to PODXL-KD SW1990 cells. **(B)** 1x10^6 SW1990 cell with either control or PODXL shRNA were subcutaneously injected into the flank of NOD/SCID mice. Tumors were measured every 3-4 days and the volume was estimated using the ellipsoid model. Data represents mean ± S.E.M, p* < .05, p*** < .001.

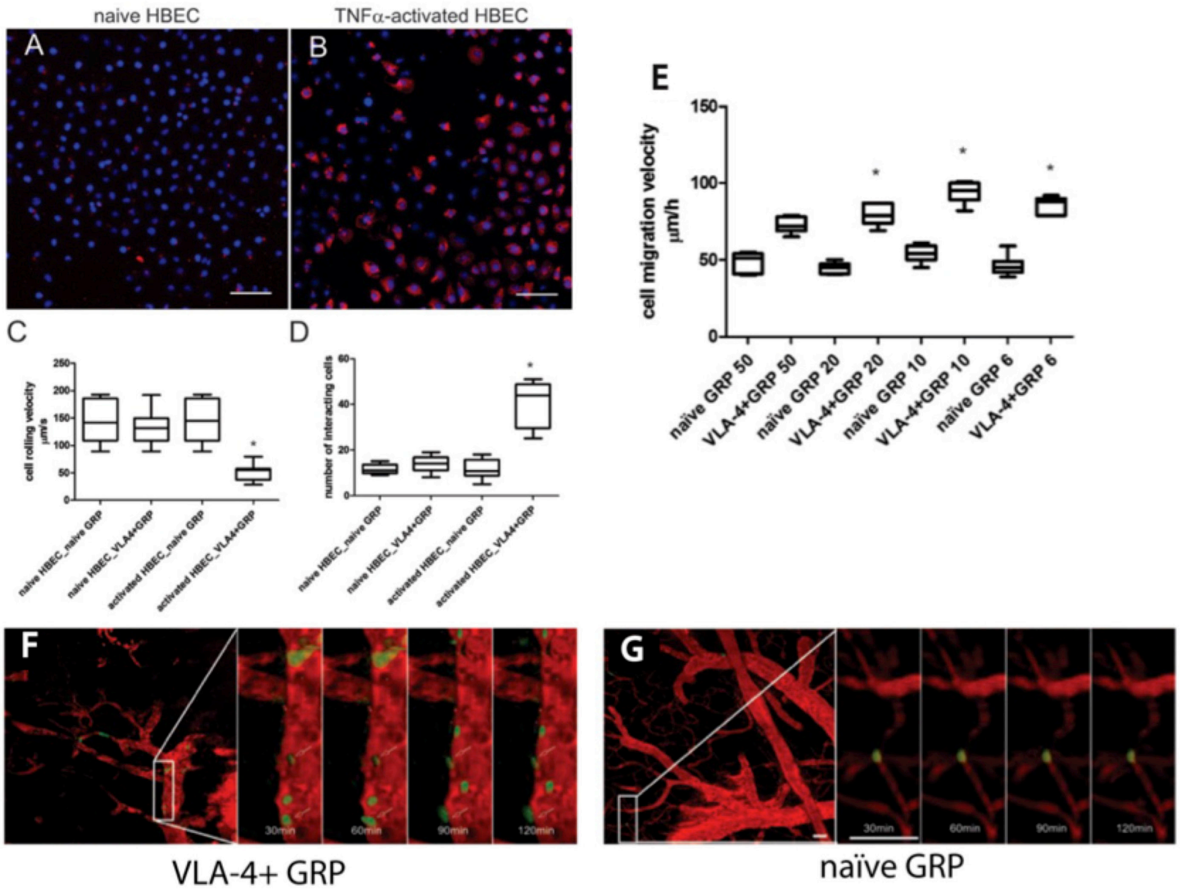

Figure 7. 2 VLA-4 enhances GRP binding and migration both in vitro and in vivo

Expression of VCAM-1 on HBEC cells that were non-activated **(A)** and activated with TNFα **(B)**. Cell rolling velocity **(C)** and number of interacting cells per 3 minute experiment **(D)** of GRP cells in the flowchamber devices coated with activated HBEC (shear stress of 1dyn/cm^2). **(E)** Average migration speed of naïve GRPs and VLA-4$^+$GRPs in straight microchannels with widths varying from 6 to 50µm. Intravital multi-photon imaging of labeled (green) VLA-4$^+$GRPs **(F)** and naïve GRPs **(G)** after intraarterial delivery, 24h after 60min MCAO, show that VLA-4 GRPs bind more frequency and migrate into to brain endothelium in vivo. Data represents mean ± S.E.M, p* < .05.

BIBLIOGRAPHY

1. Siegel, R. L., K. D. Miller, and A. Jemal. 2016. Cancer statistics, 2016. CA: a cancer journal for clinicians 66:7-30.

2. Giovino, G. A. 2002. Epidemiology of tobacco use in the United States. Oncogene 21:7326.

3. Cress, R. D., C. Morris, G. L. Ellison, and M. T. Goodman. 2006. Secular changes in colorectal cancer incidence by subsite, stage at diagnosis, and race/ethnicity, 1992–2001. Cancer 107:1142-1152.

4. Society, A. C. 2013. Cancer facts and figures 2013. American Cancer Society Atlanta.

5. Wirtz, D., K. Konstantopoulos, and P. C. Searson. 2011. The physics of cancer: the role of physical interactions and mechanical forces in metastasis. Nature Reviews Cancer 11:512-522.

6. Chambers, A. F., A. C. Groom, and I. C. MacDonald. 2002. Metastasis: dissemination and growth of cancer cells in metastatic sites. Nature Reviews Cancer 2:563-572.

7. Paget, S. 1889. The distribution of secondary growths in cancer of the breast. The Lancet 133:571-573.

8. Fidler, I. J., and M. L. Kripke. 1977. Metastasis results from preexisting variant cells within a malignant tumor. Science 197:893-895.

9. Langley, R. R., and I. J. Fidler. 2007. Tumor cell-organ microenvironment interactions in the pathogenesis of cancer metastasis. Endocrine reviews 28:297-321.

10. Talmadge, J. E., and I. J. Fidler. 2010. AACR centennial series: the biology of cancer metastasis: historical perspective. Cancer research 70:5649-5669.

11. Naito, S., R. Giavazzi, and I. Fidler. 1986. Correlation between the in vitro interaction of tumor cells with an organ environment and metastatic behavior in vivo. Invasion & metastasis 7:16-29.

12. Fournier, D., E. Weber, W. Hoeffken, M. Bauer, F. Kubli, and V. Barth. 1980. Growth rate of 147 mammary carcinomas. Cancer 45:2198-2207.

13. Weigelt, B., A. M. Glas, L. F. Wessels, A. T. Witteveen, J. L. Peterse, and L. J. van't Veer. 2003. Gene expression profiles of primary breast tumors maintained in

distant metastases. Proceedings of the National Academy of Sciences 100:15901-15905.

14. Kripke, M. L., E. Gruys, and I. J. Fidler. 1978. Metastatic heterogeneity of cells from an ultraviolet light-induced murine fibrosarcoma of recent origin. Cancer research 38:2962-2967.

15. Nicolson, G. L., K. W. Brunson, and I. J. Fidler. 1978. Specificity of arrest, survival, and growth of selected metastatic variant cell lines. Cancer research 38:4105-4111.

16. Folkman, J., and M. Klagsbrun. 1987. Angiogenic factors. Science 235:442-448.

17. Turner, H. E., A. L. Harris, S. Melmed, and J. A. Wass. 2003. Angiogenesis in endocrine tumors. Endocrine reviews 24:600-632.

18. van Zijl, F., G. Krupitza, and W. Mikulits. 2011. Initial steps of metastasis: cell invasion and endothelial transmigration. Mutation Research/Reviews in Mutation Research 728:23-34.

19. Harris, T. J., and U. Tepass. 2010. Adherens junctions: from molecules to morphogenesis. Nature reviews Molecular cell biology 11:502-514.

20. Thiery, J. P., H. Acloque, R. Y. Huang, and M. A. Nieto. 2009. Epithelial-mesenchymal transitions in development and disease. Cell 139:871-890.

21. Hegerfeldt, Y., M. Tusch, E.-B. Bröcker, and P. Friedl. 2002. Collective cell movement in primary melanoma explants. Cancer research 62:2125-2130.

22. Fernando, R. I., M. Litzinger, P. Trono, D. H. Hamilton, J. Schlom, and C. Palena. 2010. The T-box transcription factor Brachyury promotes epithelial-mesenchymal transition in human tumor cells. The Journal of clinical investigation 120:533-544.

23. Egeblad, M., and Z. Werb. 2002. New functions for the matrix metalloproteinases in cancer progression. Nature Reviews Cancer 2:161-174.

24. Fidler, I. J. 1970. Metastasis: quantitative analysis of distribution and fate of tumor emboli labeled with 125I-5-iodo-2′-deoxyuridine. Journal of the National Cancer Institute 45:773-782.

25. Turitto, V. 1981. Blood viscosity, mass transport, and thrombogenesis. Progress in hemostasis and thrombosis 6:139-177.

26. Hanahan, D., and R. A. Weinberg. 2011. Hallmarks of cancer: the next generation. Cell 144:646-674.

27. Cheung, L. S.-L. 2012. Biophysics of selectin-mediated cell adhesion. In Comprehensive Biophysics. elsevier, . 10-32.

28. LongbiaoYao, J. P., H. Setiadi, K. D. Pate, and R. P. McEver. 1996. Interleukin 4 or oncostatin M induces a prolonged increase in P-selectin mRNA and protein in human endothelial cells.

29. Kansas, G. S. 1996. Selectins and their ligands: current concepts and controversies. Blood 88:3259-3287.

30. Varki, A. 1997. Selectin ligands: will the real ones please stand up? Journal of Clinical Investigation 99:158.

31. Konstantopoulos, K., and S. N. Thomas. 2009. Cancer cells in transit: the vascular interactions of tumor cells. Annual review of biomedical engineering 11:177-202.

32. Konstantopoulos, K., S. Kukreti, and L. V. McIntire. 1998. Biomechanics of cell interactions in shear fields. Advanced drug delivery reviews 33:141-164.

33. McEver, R. P. 1997. Selectin-carbohydrate interactions during inflammation and metastasis. Glycoconjugate journal 14:585-591.

34. Park, H.-U., J.-W. Kim, G. E. Kim, H.-I. Bae, S. C. Crawley, S. C. Yang, J. R. Gum, S. K. Batra, K. Rousseau, and D. M. Swallow. 2003. Aberrant expression of MUC3 and MUC4 membrane-associated mucins and sialyl lex antigen in pancreatic intraepithelial neoplasia. Pancreas 26:e48-e54.

35. Satomura, Y., N. Sawabu, Y. Takemori, H. Ohta, H. Watanabe, T. Okai, K. Watanabe, H. Matsuno, and F. Konishi. 1991. Expression of various sialylated carbohydrate antigens in malignant and nonmalignant pancreatic tissues. Pancreas 6:448-458.

36. Borsig, L., R. Wong, R. O. Hynes, N. M. Varki, and A. Varki. 2002. Synergistic effects of L-and P-selectin in facilitating tumor metastasis can involve non-mucin ligands and implicate leukocytes as enhancers of metastasis. Proceedings of the National Academy of Sciences 99:2193-2198.

37. Piper, J. W., R. A. Swerlick, and C. Zhu. 1998. Determining force dependence of two-dimensional receptor-ligand binding affinity by centrifugation. Biophysical journal 74:492-513.

38. Evans, E., D. Berk, and A. Leung. 1991. Detachment of agglutinin-bonded red blood cells. I. Forces to rupture molecular-point attachments. Biophysical journal 59:838-848.

39. Chesla, S. E., P. Selvaraj, and C. Zhu. 1998. Measuring two-dimensional receptor-ligand binding kinetics by micropipette. Biophysical journal 75:1553-1572.

40. Cheung, L. S.-L., D. J. Shea, N. Nicholes, A. Date, M. Ostermeier, and K. Konstantopoulos. 2015. Characterization of Monobody Scaffold Interactions with Ligand via Force Spectroscopy and Steered Molecular Dynamics. Scientific reports 5.

41. Panorchan, P., M. S. Thompson, K. J. Davis, Y. Tseng, K. Konstantopoulos, and D. Wirtz. 2006. Single-molecule analysis of cadherin-mediated cell-cell adhesion. Journal of Cell Science 119:66-74.

42. Raman, P. S., C. S. Alves, D. Wirtz, and K. Konstantopoulos. 2011. Single-molecule binding of CD44 to fibrin versus P-selectin predicts their distinct shear-dependent interactions in cancer. Journal of Cell Science 124:1903-1910.

43. Marshall, B. T., M. Long, J. W. Piper, T. Yago, R. P. McEver, and C. Zhu. 2003. Direct observation of catch bonds involving cell-adhesion molecules. Nature 423:190-193.

44. Alon, R., T. Feizi, C.-T. Yuen, R. C. Fuhlbrigge, and T. A. Springer. 1995. Glycolipid ligands for selectins support leukocyte tethering and rolling under physiologic flow conditions. The Journal of Immunology 154:5356-5366.

45. Hanley, W., O. McCarty, S. Jadhav, Y. Tseng, D. Wirtz, and K. Konstantopoulos. 2003. Single molecule characterization of P-selectin/ligand binding. Journal of Biological Chemistry 278:10556-10561.

46. Alon, R., S. Chen, R. Fuhlbrigge, K. D. Puri, and T. A. Springer. 1998. The kinetics and shear threshold of transient and rolling interactions of L-selectin with its ligand on leukocytes. Proceedings of the National Academy of Sciences 95:11631-11636.

47. Liu, B., W. Chen, B. D. Evavold, and C. Zhu. 2014. Accumulation of dynamic catch bonds between TCR and agonist peptide-MHC triggers T cell signaling. Cell 157:357-368.

48. Caputo, K. E., D. Lee, M. R. King, and D. A. Hammer. 2007. Adhesive dynamics simulations of the shear threshold effect for leukocytes. Biophysical journal 92:787-797.

49. McCarty, O. J., S. A. Mousa, P. F. Bray, and K. Konstantopoulos. 2000. Immobilized platelets support human colon carcinoma cell tethering, rolling, and firm adhesion under dynamic flow conditions. Blood 96:1789-1797.

50. Cheung, L. S.-L., and K. Konstantopoulos. 2011. An analytical model for determining two-dimensional receptor-ligand kinetics. Biophysical journal 100:2338-2346.

51. Tong, Z., L. S.-L. Cheung, K. J. Stebe, and K. Konstantopoulos. 2012. Selectin-mediated adhesion in shear flow using micropatterned substrates: multiple-bond interactions govern the critical length for cell binding. Integrative Biology 4:847-856.

52. Dallas, M. R., S.-H. Chen, M. M. Streppel, S. Sharma, A. Maitra, and K. Konstantopoulos. 2012. Sialofucosylated podocalyxin is a functional E-and L-selectin ligand expressed by metastatic pancreatic cancer cells. American Journal of Physiology-Cell Physiology 303:C616-C624.

53. Chen, S.-H., M. R. Dallas, E. M. Balzer, and K. Konstantopoulos. 2012. Mucin 16 is a functional selectin ligand on pancreatic cancer cells. The FASEB Journal 26:1349-1359.

54. Kerjaschki, D., D. J. Sharkey, and M. G. Farquhar. 1984. Identification and characterization of podocalyxin—the major sialoprotein of the renal glomerular epithelial cell. J Cell Biol 98:1591-1596.

55. Kershaw, D. B., P. E. Thomas, B. L. Wharram, M. Goyal, J. E. Wiggins, C. I. Whiteside, and R. C. Wiggins. 1995. Molecular cloning, expression, and characterization of podocalyxin-like protein 1 from rabbit as a transmembrane protein of glomerular podocytes and vascular endothelium. Journal of Biological Chemistry 270:29439-29446.

56. Yasuoka, H., M. Tsujimoto, M. Inagaki, R. Kodama, H. Tsuji, Y. Iwahashi, Y. Mabuchi, K. Ino, T. Sanke, and Y. Nakamura. 2012. Clinicopathological significance of podocalyxin and phosphorylated ezrin in uterine endometrioid adenocarcinoma. Journal of clinical pathology 65:399-402.

57. Larsson, A., M. Johansson, S. Wangefjord, A. Gaber, B. Nodin, P. Kucharzewska, C. Welinder, M. Belting, J. Eberhard, and A. Johnsson. 2011. Overexpression of podocalyxin-like protein is an independent factor of poor prognosis in colorectal cancer. British journal of cancer 105:666-672.

58. Ney, J. T., H. Zhou, B. Sipos, R. Büttner, X. Chen, G. Klöppel, and I. Gütgemann. 2007. Podocalyxin-like protein 1 expression is useful to differentiate pancreatic ductal adenocarcinomas from adenocarcinomas of the biliary and gastrointestinal tracts. Human pathology 38:359-364.

59. Schmieder, S., M. Nagai, R. A. Orlando, T. Takeda, and M. G. Farquhar. 2004. Podocalyxin activates RhoA and induces actin reorganization through NHERF1 and Ezrin in MDCK cells. Journal of the American Society of Nephrology 15:2289-2298.

60. Perez, B. H., and I. K. Gipson. 2008. Focus on molecules: human mucin MUC16. Experimental eye research 87:400.

61. Bast Jr, R., F. Xu, Y. Yu, S. Barnhill, Z. Zhang, and G. Mills. 1997. CA 125: the past and the future. The International journal of biological markers 13:179-187.

62. Felder, M., A. Kapur, J. Gonzalez-Bosquet, S. Horibata, J. Heintz, R. Albrecht, L. Fass, J. Kaur, K. Hu, and H. Shojaei. 2014. MUC16 (CA125): tumor biomarker to cancer therapy, a work in progress. Molecular cancer 13:129.

63. Bast Jr, R. C., T. L. Klug, E. S. John, E. Jenison, J. M. Niloff, H. Lazarus, R. S. Berkowitz, T. Leavitt, C. T. Griffiths, and L. Parker. 1983. A radioimmunoassay using a monoclonal antibody to monitor the course of epithelial ovarian cancer. New England Journal of Medicine 309:883-887.

64. Haridas, D., S. Chakraborty, M. P. Ponnusamy, I. Lakshmanan, S. Rachagani, E. Cruz, S. Kumar, S. Das, S. M. Lele, and J. M. Anderson. 2011. Pathobiological implications of MUC16 expression in pancreatic cancer. PloS one 6:e26839.

65. Chen, S.-H., W.-C. Hung, P. Wang, C. Paul, and K. Konstantopoulos. 2013. Mesothelin binding to CA125/MUC16 promotes pancreatic cancer cell motility and invasion via MMP-7 activation. Scientific reports 3:1870.

66. Markman, M., M. Federico, P. Liu, E. Hannigan, and D. Alberts. 2006. Significance of early changes in the serum CA-125 antigen level on overall survival in advanced ovarian cancer. Gynecologic oncology 103:195-198.

67. Raman, P. S., C. S. Alves, D. Wirtz, and K. Konstantopoulos. 2012. Distinct kinetic and molecular requirements govern CD44 binding to hyaluronan versus fibrin (ogen). Biophysical journal 103:415-423.

68. Ponta, H., L. Sherman, and P. A. Herrlich. 2003. CD44: from adhesion molecules to signalling regulators. Nature reviews Molecular cell biology 4:33-45.

69. Aruffo, A., I. Stamenkovic, M. Melnick, C. B. Underhill, and B. Seed. 1990. CD44 is the principal cell surface receptor for hyaluronate. Cell 61:1303-1313.

70. Martin, T. A., G. Harrison, R. E. Mansel, and W. G. Jiang. 2003. The role of the CD44/ezrin complex in cancer metastasis. Critical reviews in oncology/hematology 46:165-186.

71. Louderbough, J. M., and J. A. Schroeder. 2011. Understanding the dual nature of CD44 in breast cancer progression. Molecular Cancer Research 9:1573-1586.

72. Jothy, S. 2003. CD44 and its partners in metastasis. Clinical & experimental metastasis 20:195-201.

73. Marhaba, R., and M. Zöller. 2004. CD44 in cancer progression: adhesion, migration and growth regulation. Journal of molecular histology 35:211-231.

74. Mohamadzadeh, M., H. DeGrendele, H. Arizpe, P. Estess, and M. Siegelman. 1998. Proinflammatory stimuli regulate endothelial hyaluronan expression and CD44/HA-dependent primary adhesion. Journal of Clinical Investigation 101:97.

75. Nandi, A., P. Estess, and M. H. Siegelman. 2000. Hyaluronan anchoring and regulation on the surface of vascular endothelial cells is mediated through the functionally active form of CD44. Journal of Biological Chemistry 275:14939-14948.

76. Yu, Q., B. P. Toole, and I. Stamenkovic. 1997. Induction of apoptosis of metastatic mammary carcinoma cells in vivo by disruption of tumor cell surface CD44 function. The Journal of experimental medicine 186:1985-1996.

77. Kim, H.-R., M. A. Wheeler, C. M. Wilson, J. Iida, D. Eng, M. A. Simpson, J. B. McCarthy, and K. M. Bullard. 2004. Hyaluronan facilitates invasion of colon carcinoma cells in vitro via interaction with CD44. Cancer research 64:4569-4576.

78. Clark, R. A., R. Alon, and T. A. Springer. 1996. CD44 and hyaluronan-dependent rolling interactions of lymphocytes on tonsillar stroma. The Journal of cell biology 134:1075-1087.

79. Ogino, S., N. Nishida, R. Umemoto, M. Suzuki, M. Takeda, H. Terasawa, J. Kitayama, M. Matsumoto, H. Hayasaka, and M. Miyasaka. 2010. Two-state conformations in the hyaluronan-binding domain regulate CD44 adhesiveness under flow condition. Structure 18:649-656.

80. Sjöblom, T., S. Jones, L. D. Wood, D. W. Parsons, J. Lin, T. D. Barber, D. Mandelker, R. J. Leary, J. Ptak, and N. Silliman. 2006. The consensus coding sequences of human breast and colorectal cancers. Science 314:268-274.

81. Hocker, J. R., R. G. Postier, M. Li, M. R. Lerner, S. A. Lightfoot, M. D. Peyton, S. J. Deb, C. M. Baker, T. L. Williams, and R. J. Hanas. 2015. Discriminating patients with early-stage pancreatic cancer or chronic pancreatitis using serum electrospray mass profiling. Cancer letters 359:314-324.

82. Murphy, S. J., S. N. Hart, J. F. Lima, B. R. Kipp, M. Klebig, J. L. Winters, C. Szabo, L. Zhang, B. W. Eckloff, and G. M. Petersen. 2013. Genetic alterations associated with progression from pancreatic intraepithelial neoplasia to invasive pancreatic tumor. Gastroenterology 145:1098-1109. e1091.

83. Perry, N. A., M. A. Ackermann, M. Shriver, L. Y. R. Hu, and A. Kontrogianni‐Konstantopoulos. 2013. Obscurins: unassuming giants enter the spotlight. IUBMB life 65:479-486.

84. Russell, M. W., M. O. Raeker, K. A. Korytkowski, and K. J. Sonneman. 2002. Identification, tissue expression and chromosomal localization of human Obscurin-MLCK, a member of the titin and Dbl families of myosin light chain kinases. Gene 282:237-246.

85. Fukuzawa, A., S. Idowu, and M. Gautel. 2005. Complete human gene structure of obscurin: implications for isoform generation by differential splicing. Journal of Muscle Research & Cell Motility 26:427-434.

86. Kontrogianni-Konstantopoulos, A., M. A. Ackermann, A. L. Bowman, S. V. Yap, and R. J. Bloch. 2009. Muscle giants: molecular scaffolds in sarcomerogenesis. Physiological reviews 89:1217-1267.

87. Kontrogianni-Konstantopoulos, A., and R. J. Bloch. 2005. Obscurin: a multitasking muscle giant. Journal of Muscle Research & Cell Motility 26:419-426.

88. Borisov, A. B., M. Ö. Raeker, and M. W. Russell. 2008. Developmental expression and differential cellular localization of obscurin and obscurin‐associated kinase in cardiac muscle cells. Journal of cellular biochemistry 103:1621-1635.

89. Perry, N. A., M. Shriver, M. G. Mameza, B. Grabias, E. Balzer, and A. Kontrogianni-Konstantopoulos. 2012. Loss of giant obscurins promotes breast epithelial cell survival through apoptotic resistance. The FASEB Journal 26:2764-2775.

90. Balakrishnan, A., F. E. Bleeker, S. Lamba, M. Rodolfo, M. Daniotti, A. Scarpa, A. A. van Tilborg, S. Leenstra, C. Zanon, and A. Bardelli. 2007. Novel somatic and germline mutations in cancer candidate genes in glioblastoma, melanoma, and pancreatic carcinoma. Cancer research 67:3545-3550.

91. Shriver, M., K. Stroka, M. Vitolo, S. Martin, D. L. Huso, K. Konstantopoulos, and A. Kontrogianni-Konstantopoulos. 2015. Loss of giant obscurins from breast epithelium promotes epithelial-to-mesenchymal transition, tumorigenicity and metastasis. Oncogene 34:4248-4259.

92. Perry, N. A., M. I. Vitolo, S. S. Martin, and A. Kontrogianni-Konstantopoulos. 2014. Loss of the obscurin-RhoGEF downregulates RhoA signaling and increases microtentacle formation and attachment of breast epithelial cells. Oncotarget 5:8558.

93. Shriver, M., S. Marimuthu, C. Paul, J. Geist, T. Seale, K. Konstantopoulos, and A. Kontrogianni-Konstantopoulos. 2016. Giant obscurins regulate the PI3K cascade in breast epithelial cells via direct binding to the PI3K/p85 regulatory subunit. Oncotarget 7:45414-45428.

94. Salaycik, K. J., C. J. Fagerstrom, K. Murthy, U. S. Tulu, and P. Wadsworth. 2005. Quantification of microtubule nucleation, growth and dynamics in wound-edge cells. Journal of Cell Science 118:4113-4122.

95. Aifuwa, I., A. Giri, N. Longe, S. H. Lee, S. S. An, and D. Wirtz. 2015. Senescent stromal cells induce cancer cell migration via inhibition of RhoA/ROCK/myosin-based cell contractility. Oncotarget 6:30516.

96. Chrzanowska-Wodnicka, M., and K. Burridge. 1996. Rho-stimulated contractility drives the formation of stress fibers and focal adhesions. The Journal of cell biology 133:1403-1415.

97. Ridley, A. 2013. RhoA, RhoB and RhoC have different roles in cancer cell migration. Journal of microscopy 251:242-249.

98. Pasapera, A. M., I. C. Schneider, E. Rericha, D. D. Schlaepfer, and C. M. Waterman. 2010. Myosin II activity regulates vinculin recruitment to focal adhesions through FAK-mediated paxillin phosphorylation. The Journal of cell biology 188:877-890.

99. Hung, W.-C., S.-H. Chen, C. D. Paul, K. M. Stroka, Y.-C. Lo, J. T. Yang, and K. Konstantopoulos. 2013. Distinct signaling mechanisms regulate migration in unconfined versus confined spaces. J Cell Biol 202:807-824.

100. Lu, D.-Y., T.-R. Lu, H.-Y. Wu, and S. Cao. 2013. Cancer Metastasis treatments. Current Drug Therapy 8:24-29.

101. Lu, D.-Y., and T.-R. Lu. 2010. Antimetastatic activities and mechanisms of bisdioxopiperazine compounds. Anti-Cancer Agents in Medicinal Chemistry (Formerly Current Medicinal Chemistry-Anti-Cancer Agents) 10:564-570.

102. Sava, G., and A. Bergamo. 1998. Drug control of solid tumour metastases: a critical view. Anticancer research 19:1117-1124.

103. Kessenbrock, K., V. Plaks, and Z. Werb. 2010. Matrix metalloproteinases: regulators of the tumor microenvironment. Cell 141:52-67.

104. Taraboletti, G., and B. Margosio. 2001. Antiangiogenic and antivascular therapy for cancer. Current opinion in pharmacology 1:378-384.

105. Iiizumi, M., W. Liu, S. K. Pai, E. Furuta, and K. Watabe. 2008. Drug development against metastasis-related genes and their pathways: a rationale for cancer therapy. Biochimica et Biophysica Acta (BBA)-Reviews on Cancer 1786:87-104.

106. Lu, D.-Y., D.-R. Lu, and J. Ding. 2010. Cell biological manifestations of Bisdioxopiperazines: treatment of human tumor cell lines in culture. Anti-Cancer Agents in Medicinal Chemistry (Formerly Current Medicinal Chemistry-Anti-Cancer Agents) 10:657-660.

107. Pardali, K., and A. Moustakas. 2007. Actions of TGF-β as tumor suppressor and pro-metastatic factor in human cancer. Biochimica et Biophysica Acta (BBA)-Reviews on Cancer 1775:21-62.

108. Steinmeyer, D. E., and E. L. McCormick. 2008. The art of antibody process development. Drug discovery today 13:613-618.

109. Vermeer, A. W., and W. Norde. 2000. The thermal stability of immunoglobulin: unfolding and aggregation of a multi-domain protein. Biophysical journal 78:394-404.

110. Skerra, A. 2000. Engineered protein scaffolds for molecular recognition. Journal of Molecular Recognition 13:167-187.

111. Nygren, P.-Å., and M. Uhlén. 1997. Scaffolds for engineering novel binding sites in proteins. Current opinion in structural biology 7:463-469.

112. Wurch, T., P. Lowe, V. Caussanel, C. Bes, A. Beck, and N. Corvaia. 2008. Development of novel protein scaffolds as alternatives to whole antibodies for imaging and therapy: status on discovery research and clinical validation. Current pharmaceutical biotechnology 9:502-509.

113. Frejd, F. Y. 2008. Novel alternative scaffolds and their potential use for tumor targeted radionuclide therapy. In Targeted Radionuclide Tumor Therapy. Springer. 89-116.

114. Koide, A., C. W. Bailey, X. Huang, and S. Koide. 1998. The fibronectin type III domain as a scaffold for novel binding proteins. Journal of molecular biology 284:1141-1151.

115. Koide, A., S. Abbatiello, L. Rothgery, and S. Koide. 2002. Probing protein conformational changes in living cells by using designer binding proteins: application to the estrogen receptor. Proceedings of the National Academy of Sciences 99:1253-1258.

116. Koide, A., R. N. Gilbreth, K. Esaki, V. Tereshko, and S. Koide. 2007. High-affinity single-domain binding proteins with a binary-code interface. Proceedings of the National Academy of Sciences 104:6632-6637.

117. Gilbreth, R. N., K. Esaki, A. Koide, S. S. Sidhu, and S. Koide. 2008. A dominant conformational role for amino acid diversity in minimalist protein–protein interfaces. Journal of molecular biology 381:407-418.

118. Hackel, B. J., A. Kapila, and K. Dane Wittrup. 2008. Picomolar affinity fibronectin domains engineered utilizing loop length diversity, recursive mutagenesis, and loop shuffling. Journal of molecular biology 381:1238-1252.

119. Gilbreth, R. N., K. Truong, I. Madu, A. Koide, J. B. Wojcik, N.-S. Li, J. A. Piccirilli, Y. Chen, and S. Koide. 2011. Isoform-specific monobody inhibitors of small ubiquitin-related modifiers engineered using structure-guided library design. Proceedings of the National Academy of Sciences 108:7751-7756.

120. Huang, R., P. Fang, and B. K. Kay. 2012. Isolation of monobodies that bind specifically to the SH3 domain of the Fyn tyrosine protein kinase. New biotechnology 29:526-533.

121. Xu, L., P. Aha, K. Gu, R. G. Kuimelis, M. Kurz, T. Lam, A. C. Lim, H. Liu, P. A. Lohse, and L. Sun. 2002. Directed evolution of high-affinity antibody mimics using mRNA display. Chemistry & biology 9:933-942.

122. Parker, M., Y. Chen, F. Danehy, K. Dufu, J. Ekstrom, E. Getmanova, J. Gokemeijer, L. Xu, and D. Lipovsek. 2005. Antibody mimics based on human fibronectin type three domain engineered for thermostability and high-affinity binding to vascular endothelial growth factor receptor two. Protein Engineering Design and Selection 18:435-444.

123. Holderfield, M., and D. K. Morrison. 2017. RAS signaling: Divide and conquer. Nature chemical biology 13:7-8.

124. Wojcik, J., A. J. Lamontanara, G. Grabe, A. Koide, L. Akin, B. Gerig, O. Hantschel, and S. Koide. 2016. Allosteric Inhibition of Bcr-Abl Kinase by High Affinity Monobody Inhibitors Directed to the Src Homology 2 (SH2)-Kinase Interface. Journal of Biological Chemistry 291:8836-8847.

125. Colman, P. M. 1994. Structure-based drug design. Current opinion in structural biology 4:868-874.

126. Marrone, T. J., a. Briggs, James M, and J. A. McCammon. 1997. Structure-based drug design: computational advances. Annual review of pharmacology and toxicology 37:71-90.

127. Bell, G. I. 1978. Models for the specific adhesion of cells to cells. Science 200:618-627.

128. Tees, D. F., R. E. Waugh, and D. A. Hammer. 2001. A microcantilever device to assess the effect of force on the lifetime of selectin-carbohydrate bonds. Biophysical journal 80:668-682.

129. Evans, E., and K. Ritchie. 1997. Dynamic strength of molecular adhesion bonds. Biophysical journal 72:1541-1555.

130. Zhu, C., and T. E. Williams. 2000. Modeling concurrent binding of multiple molecular species in cell adhesion. Biophysical journal 79:1850-1857.

131. Yago, T., J. Wu, C. D. Wey, A. G. Klopocki, C. Zhu, and R. P. McEver. 2004. Catch bonds govern adhesion through L-selectin at threshold shear. The Journal of cell biology 166:913-923.

132. Burdick, M. M., J. M. McCaffery, Y. S. Kim, B. S. Bochner, and K. Konstantopoulos. 2003. Colon carcinoma cell glycolipids, integrins, and other glycoproteins mediate adhesion to HUVECs under flow. American Journal of Physiology-Cell Physiology 284:C977-C987.

133. Burdick, M. M., and K. Konstantopoulos. 2004. Platelet-induced enhancement of LS174T colon carcinoma and THP-1 monocytoid cell adhesion to vascular endothelium under flow. American Journal of Physiology-Cell Physiology 287:C539-C547.

134. Läubli, H., J. L. Stevenson, A. Varki, N. M. Varki, and L. Borsig. 2006. L-selectin facilitation of metastasis involves temporal induction of Fut7-dependent ligands at sites of tumor cell arrest. Cancer research 66:1536-1542.

135. Napier, S. L., Z. R. Healy, R. L. Schnaar, and K. Konstantopoulos. 2007. Selectin Ligand Expression Regulates the Initial Vascular Interactions of Colon Carcinoma Cells THE ROLES OF CD44V AND ALTERNATIVE SIALOFUCOSYLATED SELECTIN LIGANDS. Journal of Biological Chemistry 282:3433-3441.

136. Thomas, S. N., F. Zhu, R. L. Schnaar, C. S. Alves, and K. Konstantopoulos. 2008. Carcinoembryonic antigen and CD44 variant isoforms cooperate to mediate colon carcinoma cell adhesion to E-and L-selectin in shear flow. Journal of Biological Chemistry 283:15647-15655.

137. Thomas, S. N., R. L. Schnaar, and K. Konstantopoulos. 2009. Podocalyxin-like protein is an E-/L-selectin ligand on colon carcinoma cells: comparative biochemical properties of selectin ligands in host and tumor cells. American Journal of Physiology-Cell Physiology 296:C505-C513.

138. Hanley, W. D., S. L. Napier, M. M. Burdick, R. L. Schnaar, R. Sackstein, and K. Konstantopoulos. 2006. Variant isoforms of CD44 are P-and L-selectin ligands on colon carcinoma cells. The FASEB Journal 20:337-339.

139. Cheung, L. S.-L., M. Kanwar, M. Ostermeier, and K. Konstantopoulos. 2012. A hot-spot motif characterizes the interface between a designed ankyrin-repeat protein and its target ligand. Biophysical journal 102:407-416.

140. Hanley, W. D., D. Wirtz, and K. Konstantopoulos. 2004. Distinct kinetic and mechanical properties govern selectin-leukocyte interactions. Journal of Cell Science 117:2503-2511.

141. Brunk, D. K., and D. A. Hammer. 1997. Quantifying rolling adhesion with a cell-free assay: E-selectin and its carbohydrate ligands. Biophysical journal 72:2820-2833.

142. Wu, L., B. Xiao, X. Jia, Y. Zhang, S. Lü, J. Chen, and M. Long. 2007. Impact of carrier stiffness and microtopology on two-dimensional kinetics of P-selectin and P-selectin glycoprotein ligand-1 (PSGL-1) interactions. Journal of Biological Chemistry 282:9846-9854.

143. Rinko, L. J., M. B. Lawrence, and W. H. Guilford. 2004. The molecular mechanics of P-and L-selectin lectin domains binding to PSGL-1. Biophysical journal 86:544-554.

144. Finger, E. B., K. D. Puri, R. Alón, M. B. Lawrence, U. H. von Andrian, and T. A. Springer. 1996. requires a threshold hydrodynamic shear. Nature 379:18.

145. Herman, C. T., G. K. Potts, M. C. Michael, N. V. Tolan, and R. C. Bailey. 2011. Probing dynamic cell–substrate interactions using photochemically generated surface-immobilized gradients: application to selectin-mediated leukocyte rolling. Integrative Biology 3:779-791.

146. Chang, K.-C., and D. A. Hammer. 2000. Adhesive dynamics simulations of sialyl-Lewis x/E-selectin-mediated rolling in a cell-free system. Biophysical journal 79:1891-1902.

147. Alón, R., D. A. Hammer, and T. A. Springer. 1995. Lifetime of the P-selectin-carbohydrate bond and its response to tensile force in hydrodynamic flow. Nature 374:539-542.

148. Cheung, L. S.-L., P. S. Raman, E. M. Balzer, D. Wirtz, and K. Konstantopoulos. 2011. Biophysics of selectin–ligand interactions in inflammation and cancer. Physical biology 8:015013.

149. Sarangapani, K. K., T. Yago, A. G. Klopocki, M. B. Lawrence, C. B. Fieger, S. D. Rosen, R. P. McEver, and C. Zhu. 2004. Low force decelerates L-selectin dissociation from P-selectin glycoprotein ligand-1 and endoglycan. Journal of Biological Chemistry 279:2291-2298.

150. Alon, R., S. Chen, K. D. Puri, E. B. Finger, and T. A. Springer. 1997. The kinetics of L-selectin tethers and the mechanics of selectin-mediated rolling. The Journal of cell biology 138:1169-1180.

151. Evans, E., A. Leung, D. Hammer, and S. Simon. 2001. Chemically distinct transition states govern rapid dissociation of single L-selectin bonds under force. Proceedings of the National Academy of Sciences 98:3784-3789.

152. Smith, M. J., E. L. Berg, and M. B. Lawrence. 1999. A direct comparison of selectin-mediated transient, adhesive events using high temporal resolution. Biophysical journal 77:3371-3383.

153. Zhang, X., D. F. Bogorin, and V. T. Moy. 2004. Molecular basis of the dynamic strength of the sialyl Lewis X—selectin interaction. ChemPhysChem 5:175-182.

154. Puri, K. D., E. B. Finger, and T. A. Springer. 1997. The faster kinetics of L-selectin than of E-selectin and P-selectin rolling at comparable binding strength. The Journal of Immunology 158:405-413.

155. Ramachandran, V., T. Yago, T. K. Epperson, M. M. Kobzdej, M. U. Nollert, R. D. Cummings, C. Zhu, and R. P. McEver. 2001. Dimerization of a selectin and its ligand stabilizes cell rolling and enhances tether strength in shear flow. Proceedings of the National Academy of Sciences 98:10166-10171.

156. Chen, S., and T. A. Springer. 1999. An automatic braking system that stabilizes leukocyte rolling by an increase in selectin bond number with shear. The Journal of cell biology 144:185-200.

157. Jadhav, S., C. D. Eggleton, and K. Konstantopoulos. 2005. A 3-D computational model predicts that cell deformation affects selectin-mediated leukocyte rolling. Biophysical journal 88:96-104.

158. Shea, D. J., D. Wirtz, K. J. Stebe, and K. Konstantopoulos. 2015. Distinct kinetic and mechanical properties govern mucin 16-and podocalyxin-mediated tumor cell adhesion to E-and L-selectin in shear flow. Oncotarget 6:24842.

159. Günthert, U., M. Hofmann, W. Rudy, S. Reber, M. Zöller, I. Hauβmann, S. Matzku, A. Wenzel, H. Ponta, and P. Herrlich. 1991. A new variant of glycoprotein CD44 confers metastatic potential to rat carcinoma cells. Cell 65:13-24.

160. Ghosh, M., C. Alves, Z. Tong, K. Tettey, K. Konstantopoulos, and K. J. Stebe. 2008. Multifunctional surfaces with discrete functionalized regions for biological applications. Langmuir 24:8134-8142.

161. Launiere, C., M. Gaskill, G. Czaplewski, J. H. Myung, S. Hong, and D. T. Eddington. 2012. Channel surface patterning of alternating biomimetic protein combinations for enhanced microfluidic tumor cell isolation. Analytical chemistry 84:4022-4028.

162. Myung, J. H., K. A. Gajjar, J. Chen, R. E. Molokie, and S. Hong. 2014. Differential detection of tumor cells using a combination of cell rolling, multivalent binding, and multiple antibodies. Analytical chemistry 86:6088-6094.

163. Nalayanda, D. D., M. Kalukanimuttam, and D. W. Schmidtke. 2007. Micropatterned surfaces for controlling cell adhesion and rolling under flow. Biomedical microdevices 9:207-214.

164. Hung, W.-C., S.-H. Chen, C. D. Paul, K. M. Stroka, Y.-C. Lo, J. T. Yang, and K. Konstantopoulos. 2013. Distinct signaling mechanisms regulate migration in unconfined versus confined spaces. The Journal of cell biology 202:807-824.

165. Stroka, K. M., H. Jiang, S.-H. Chen, Z. Tong, D. Wirtz, S. X. Sun, and K. Konstantopoulos. 2014. Water permeation drives tumor cell migration in confined microenvironments. Cell 157:611-623.

166. Schmidt, B. J., P. Huang, K. S. Breuer, and M. B. Lawrence. 2008. Catch strip assay for the relative assessment of two-dimensional protein association kinetics. Analytical chemistry 80:944-950.

167. Stott, S. L., C.-H. Hsu, D. I. Tsukrov, M. Yu, D. T. Miyamoto, B. A. Waltman, S. M. Rothenberg, A. M. Shah, M. E. Smas, and G. K. Korir. 2010. Isolation of circulating tumor cells using a microvortex-generating herringbone-chip. Proceedings of the National Academy of Sciences 107:18392-18397.

168. Jones, S., X. Zhang, D. W. Parsons, J. C.-H. Lin, R. J. Leary, P. Angenendt, P. Mankoo, H. Carter, H. Kamiyama, and A. Jimeno. 2008. Core signaling pathways in human pancreatic cancers revealed by global genomic analyses. Science 321:1801-1806.

169. Paul, C. D., D. J. Shea, M. R. Mahoney, A. Chai, V. Laney, W.-C. Hung, and K. Konstantopoulos. 2016. Interplay of the physical microenvironment, contact guidance, and intracellular signaling in cell decision making. The FASEB Journal 30:2161-2170.

170. Stroka, K. M., B. S. Wong, M. Shriver, J. M. Phillip, D. Wirtz, A. Kontrogianni-Konstantopoulos, and K. Konstantopoulos. 2016. Loss of giant obscurins alters breast epithelial cell mechanosensing of matrix stiffness. Oncotarget 5.

171. Weigelin, B., G.-J. Bakker, and P. Friedl. 2012. Intravital third harmonic generation microscopy of collective melanoma cell invasion: principles of interface guidance and microvesicle dynamics. IntraVital 1:32-43.

172. Friedl, P., and S. Alexander. 2011. Cancer invasion and the microenvironment: plasticity and reciprocity. Cell 147:992-1009.

173. Vega, F. M., and A. J. Ridley. 2008. Rho GTPases in cancer cell biology. FEBS letters 582:2093-2101.

174. Watanabe, T., J. Noritake, and K. Kaibuchi. 2005. Regulation of microtubules in cell migration. Trends in cell biology 15:76-83.

175. Matov, A., K. Applegate, P. Kumar, C. Thoma, W. Krek, G. Danuser, and T. Wittmann. 2010. Analysis of microtubule dynamic instability using a plus-end growth marker. Nature methods 7:761-768.

176. Mao, Y., L. Xi, Q. Li, Z. Cai, Y. Lai, X. Zhang, and C. Yu. 2016. Regulation of cell apoptosis and proliferation in pancreatic cancer through PI3K/Akt pathway via Polo-like kinase 1. Oncology reports 36:49-56.

177. Yuan, T., and L. Cantley. 2008. PI3K pathway alterations in cancer: variations on a theme. Oncogene 27:5497-5510.

178. Falasca, M., F. Selvaggi, R. Buus, S. Sulpizio, and C. E Edling. 2011. Targeting phosphoinositide 3-kinase pathways in pancreatic cancer-from molecular signalling to clinical trials. Anti-Cancer Agents in Medicinal Chemistry (Formerly Current Medicinal Chemistry-Anti-Cancer Agents) 11:455-463.

179. Ridley, A. J., M. A. Schwartz, K. Burridge, R. A. Firtel, M. H. Ginsberg, G. Borisy, J. T. Parsons, and A. R. Horwitz. 2003. Cell migration: integrating signals from front to back. Science 302:1704-1709.

180. Hall, A. 2012. Rho family gtpases. Portland Press Limited.

181. Ridley, A. J. 2001. Rho GTPases and cell migration. Journal of Cell Science 114:2713-2722.

182. Ford-Speelman, D. L., J. A. Roche, A. L. Bowman, and R. J. Bloch. 2009. The rho-guanine nucleotide exchange factor domain of obscurin activates RhoA signaling in skeletal muscle. Molecular biology of the cell 20:3905-3917.

183. Osaki, M., M. a. Oshimura, and H. Ito. 2004. PI3K-Akt pathway: its functions and alterations in human cancer. Apoptosis 9:667-676.

184. Vadas, O., J. E. Burke, X. Zhang, A. Berndt, and R. L. Williams. 2011. Structural Basis for Activation and Inhibition of Class I Phosphoinositide.

185. Pan, Y., L. Wang, S.-g. Kang, Y. Lu, Z. Yang, T. Huynh, C. Chen, R. Zhou, M. Guo, and Y. Zhao. 2015. Gd–metallofullerenol nanomaterial suppresses pancreatic cancer metastasis by inhibiting the interaction of histone deacetylase 1 and metastasis-associated protein 1. ACS nano 9:6826-6836.

186. Zhong, Y., Y. Naito, L. Cope, S. Naranjo-Suarez, T. Saunders, S.-M. Hong, M. G. Goggins, J. M. Herman, C. L. Wolfgang, and C. A. Iacobuzio-Donahue. 2014. Functional p38 MAPK identified by biomarker profiling of pancreatic cancer restrains growth through JNK inhibition and correlates with improved survival. Clinical cancer research 20:6200-6211.

187. Wu, P.-H., J. M. Phillip, S. B. Khatau, W.-C. Chen, J. Stirman, S. Rosseel, K. Tschudi, J. Van Patten, M. Wong, and S. Gupta. 2015. Evolution of cellular morpho-phenotypes in cancer metastasis. Scientific reports 5:18437.

188. Yu, H., J. Raymonda, T. McMahon, and A. Campagnari. 2000. Detection of biological threat agents by immunomagnetic microsphere-based solid phase fluorogenic-and electro-chemiluminescence. Biosensors and Bioelectronics 14:829-840.

189. Leader, B., Q. J. Baca, and D. E. Golan. 2008. Protein therapeutics: a summary and pharmacological classification. Nature Reviews Drug Discovery 7:21-39.

190. Cotton, G. J., B. Ayers, R. Xu, and T. W. Muir. 1999. Insertion of a synthetic peptide into a recombinant protein framework: a protein biosensor. Journal of the American Chemical Society 121:1100-1101.

191. Gulyani, A., E. Vitriol, R. Allen, J. Wu, D. Gremyachinskiy, S. Lewis, B. Dewar, L. M. Graves, B. K. Kay, and B. Kuhlman. 2011. A biosensor generated via high-throughput screening quantifies cell edge Src dynamics. Nature chemical biology 7:437-444.

192. Binz, H. K., P. Amstutz, A. Kohl, M. T. Stumpp, C. Briand, P. Forrer, M. G. Grütter, and A. Plückthun. 2004. High-affinity binders selected from designed ankyrin repeat protein libraries. Nature biotechnology 22:575-582.

193. Batori, V., A. Koide, and S. Koide. 2002. Exploring the potential of the monobody scaffold: effects of loop elongation on the stability of a fibronectin type III domain. Protein engineering 15:1015-1020.

194. Cota, E., A. Steward, S. B. Fowler, and J. Clarke. 2001. The folding nucleus of a fibronectin type III domain is composed of core residues of the immunoglobulin-like fold. Journal of molecular biology 305:1185-1194.

195. Cota, E., S. J. Hamill, S. B. Fowler, and J. Clarke. 2000. Two proteins with the same structure respond very differently to mutation: the role of plasticity in protein stability. Journal of molecular biology 302:713-725.

196. Cohen, N. C., J. M. Blaney, C. Humblet, P. Gund, and D. C. Barry. 1990. Molecular modeling software and methods for medicinal chemistry. Journal of medicinal chemistry 33:883-894.

197. Izrailev, S., S. Stepaniants, B. Isralewitz, D. Kosztin, H. Lu, F. Molnar, W. Wriggers, and K. Schulten. 1999. Steered molecular dynamics. In Computational molecular dynamics: challenges, methods, ideas. Springer. 39-65.

198. Moreira, I. S., P. A. Fernandes, and M. J. Ramos. 2007. Hot spots—A review of the protein–protein interface determinant amino‐acid residues. Proteins: Structure, Function, and Bioinformatics 68:803-812.

199. Bogan, A. A., and K. S. Thorn. 1998. Anatomy of hot spots in protein interfaces. Journal of molecular biology 280:1-9.

200. Humphrey, W., A. Dalke, and K. Schulten. 1996. VMD: visual molecular dynamics. Journal of molecular graphics 14:33-38.

201. Phillips, J. C., R. Braun, W. Wang, J. Gumbart, E. Tajkhorshid, E. Villa, C. Chipot, R. D. Skeel, L. Kale, and K. Schulten. 2005. Scalable molecular dynamics with NAMD. Journal of computational chemistry 26:1781-1802.

202. MacKerell, A. D., D. Bashford, M. Bellott, R. Dunbrack, J. Evanseck, M. J. Field, S. Fischer, J. Gao, H. Guo, and S. a. Ha. 1998. All-atom empirical potential for molecular modeling and dynamics studies of proteins. The Journal of Physical Chemistry B 102:3586-3616.

203. Jorgensen, W. L., J. Chandrasekhar, J. D. Madura, R. W. Impey, and M. L. Klein. 1983. Comparison of simple potential functions for simulating liquid water. The Journal of chemical physics 79:926.

204. Darden, T., D. York, and L. Pedersen. 1993. Particle mesh Ewald: An N · log (N) method for Ewald sums in large systems. The Journal of chemical physics 98:10089.

205. Schneider, T., and E. Stoll. 1978. Molecular-dynamics study of a three-dimensional one-component model for distortive phase transitions. Physical Review B 17:1302.

206. Feller, S. E., Y. Zhang, R. W. Pastor, and B. R. Brooks. 1995. Constant pressure molecular dynamics simulation: the Langevin piston method. The Journal of chemical physics 103:4613.

207. Tanner, D. E., K.-Y. Chan, J. C. Phillips, and K. Schulten. 2011. Parallel generalized Born implicit solvent calculations with NAMD. Journal of Chemical Theory and Computation 7:3635-3642.

208. Baker, E., and R. Hubbard. 1984. Hydrogen bonding in globular proteins. Progress in biophysics and molecular biology 44:97-179.

209. Kim, D. E., D. Chivian, and D. Baker. 2004. Protein structure prediction and analysis using the Robetta server. Nucleic acids research 32:W526-W531.

210. Krüger, D. M., and H. Gohlke. 2010. DrugScorePPI webserver: fast and accurate in silico alanine scanning for scoring protein–protein interactions. Nucleic acids research 38:W480-W486.

211. Dobrowsky, T. M., P. Panorchan, K. Konstantopoulos, and D. Wirtz. 2008. Live-Cell Single-Molecule Force Spectroscopy. Methods in cell biology 89:411-432.

212. Alves, C. S., and K. Konstantopoulos. 2012. PDGF Suppresses the Sulfation of CD44v and Potentiates CD44v-Mediated Binding of Colon Carcinoma Cells to Fibrin under Flow. PloS one 7:e41472.

213. Schuck, P., and A. P. Minton. 1996. Kinetic analysis of biosensor data: elementary tests for self-consistency. Trends in biochemical sciences 21:458-460.

214. Kortemme, T., and D. Baker. 2002. A simple physical model for binding energy hot spots in protein–protein complexes. Proceedings of the National Academy of Sciences 99:14116-14121.

215. Shivakumar, D., Y. Deng, and B. t. Roux. 2009. Computations of absolute solvation free energies of small molecules using explicit and implicit solvent model. Journal of Chemical Theory and Computation 5:919-930.

216. Beeby, M., J. C. Gumbart, B. Roux, and G. J. Jensen. 2013. Architecture and assembly of the Gram-positive cell wall. Molecular microbiology 88:664-672.

217. Felix, J., J. Elegheert, I. Gutsche, A. V. Shkumatov, Y. Wen, N. Bracke, E. Pannecoucke, I. Vandenberghe, B. Devreese, and D. I. Svergun. 2013. Human IL-34 and CSF-1 establish structurally similar extracellular assemblies with their common hematopoietic receptor. Structure 21:528-539.

218. Koide, A., J. Wojcik, R. N. Gilbreth, R. J. Hoey, and S. Koide. 2012. Teaching an old scaffold new tricks: monobodies constructed using alternative surfaces of the FN3 scaffold. Journal of molecular biology 415:393-405.

219. Bahadur, R. P., P. Chakrabarti, F. Rodier, and J. Janin. 2003. Dissecting subunit interfaces in homodimeric proteins. Proteins: Structure, Function, and Bioinformatics 53:708-719.

220. Pednekar, D., A. Tendulkar, and S. Durani. 2009. Electrostatics-defying interaction between arginine termini as a thermodynamic driving force in protein–protein interaction. Proteins: Structure, Function, and Bioinformatics 74:155-163.

221. Magalhaes, A., B. Maigret, J. Hoflack, J. Gomes, and H. Scheraga. 1994. Contribution of unusual arginine-arginine short-range interactions to stabilization and recognition in proteins. Journal of protein chemistry 13:195-215.

222. Soetens, J.-C., C. Millot, C. Chipot, G. Jansen, J. G. Ángyán, and B. Maigret. 1997. Effect of polarizability on the potential of mean force of two cations. The guanidinium-guanidinium ion pair in water. The Journal of Physical Chemistry B 101:10910-10917.

223. Maksimiak, K., S. Rodziewicz-Motowidlo, C. Czaplewski, A. Liwo, and H. A. Scheraga. 2003. Molecular simulation study of the potentials of mean force for the interactions between models of like-charged and between charged and nonpolar amino acid side chains in water. The Journal of Physical Chemistry B 107:13496-13504.

224. Bruns, C. J., M. T. Harbison, H. Kuniyasu, I. Eue, and I. J. Fidler. 1999. In vivo selection and characterization of metastatic variants from human pancreatic adenocarcinoma by using orthotopic implantation in nude mice. Neoplasia 1:50-62.

225. Soares, K. C., K. Foley, K. Olino, A. Leubner, S. C. Mayo, A. Jain, E. Jaffee, R. D. Schulick, K. Yoshimura, and B. Edil. 2014. A preclinical murine model of hepatic metastases. JoVE (Journal of Visualized Experiments):e51677-e51677.

226. Ouyang, H., L.-j. Mou, C. Luk, N. Liu, J. Karaskova, J. Squire, and M.-S. Tsao. 2000. Immortal human pancreatic duct epithelial cell lines with near normal genotype and phenotype. The American journal of pathology 157:1623-1631.

CURRICULUM VITAE

Daniel Shea

E-Mail: Daniel.Shea.J@gmail.com
Born January 2nd, 1989 • Durham, North Carolina

QUALIFICATIONS PROFILE

- A self-motivated PhD in Chemical and Biomolecular Engineering with **six** years of research experience in chemical and biological engineering
- Strong project management skills with demonstrated success in independently managing multiple projects and communicating results to individuals of varied backgrounds and expertise
- Excellent design of experiment skills, with experience in working in a productive and fast-paced environment

EDUCATION

The Johns Hopkins University (Advisor: Konstantinos Konstantopoulos, PhD)
Sept 2012 – Spring 2017
Doctor of Philosophy, Chemical and Biomolecular Engineering
Northeastern University *Sept 2007 - May 2012*
Bachelor of Science, Chemical Engineering, GPA: 3.98/4.0 **(Summa Cum Laude)**

RESEACH SKILLS

- **Broad knowledge of engineering and biology** - Worked in a collaborative multidisciplinary environment. Performed research that encompasses cell biology, cell biophysics, microfabrication and engineering.
- **Cell culture** – Primary cell culture, breast and pancreatic cell culture, plant cell culture, CHO cell culture, cell selection technology, media development and optimization, shaker flask culture, spinner flask culture, bioreactor operations and cell culture, scale-up and scale-down principles, preparation of cell banks, cGMP cell culture, bacterial (*E coli*) culture, drug treatment.

  Molecular Biology – Selection for stable cell lines, DNA/RNA extraction/purification, DNA gel electrophoresis, transformation, real-time PCR, ELISA, lentiviral transduction, transient transfection, protein knock downs, single cell cloning.
- **Cell/Protein-based assays** - Flow cytometry, recombinant protein expression, protein purification: affinity columns, HPCL, SDS-page, and Western Blot, cell viability and apoptosis assays, proliferation assays, drug response studies, immunoprecipitation (IP), co-immunoprecipitation (co-IP), immunohistochemistry (IHC), immunocytochemistry (ICC*),* cellular signaling, phosphorylation, plate reader assays, microfluidic cell binding assays, single molecule force spectroscopy.
- **Microscopy** – Fluorescence microscopy, confocal microscopy, image analysis, atomic

force microscopy, TIRF, FRAP assay.

- **In vivo**- SubQ tumor injections of mice, mouse tissue biopsy.
- **Software**- Image J ,Matlab, GraphPad Prism, Adobe illustrator, AutoCAD, Microsoft office suite
- **Mentoring** - Mentored 3 undergraduates on their research.

ACADEMIC RESEARCH EXPERIENCE

The Johns Hopkins University, *September 2012 – March 2017*

Ph.D. Student, *Advisor: Konstantinos Konstantopoulos, PhD*

Thesis Title: Multi-scale examination of pancreatic cancer cell biophysics

- Determined how the kinetic properties pancreatic tumor cell ligands affect adhesion to E- and L-selectins in shear flow.
- Designed *in vitro* model to measure how pancreatic tumor cell rolling on E-selectin influences binding to hyaluronic acid in shear flow.
- Identified giant obscurins and PODXL as key players in pancreatic cancer cell migration and cytoskeletal dynamics.
- Characterized the monobody YS1 scaffold interactions with ligand maltose binding protein.

Northeastern University

Undergraduate Researcher, *Advisor: Carolyn Lee Parsons, PhD*

January 2011 – July 2012

- Optimized alkaloid production for the California poppy cell culture system.
- Extracted alkaloids from cell suspension and media and ran HPLC to examine alkaloid production.
- Explored the effects of increased SAM production found in elicited cultures with high alkaloid production.

Undergraduate Research Co-op, *Advisor: Ronald Willey, PhD*

June 2009 – December 2009

- Characterized the surface properties of metal organic frameworks and aerogels.
- Evaluated the gas adsorption and surface morphologies of metal organic frameworks and aerogels.

INDUSTRY EXPERIENCE

Acceleron Pharma, Cambridge, MA

Cell Culture and Process Development Co-op/intern July-Dec 2010, May-Aug 2012

- Characterized protein therapeutic production produced using CHO cells grown in both 2L-5L bioreactors and shaker flasks.
- Utilized HPLC to determine protein production of CHO cell culture batches.

- Performed studies to evaluate cell culture run conditions to optimize protein production working with the manufacturing team.
- Assisted in technical transfer of cell culture process to Shire Pharmaceuticals.
- Worked in cGMP environment for large scale (250L) cell culture manufacturing of Dalantercept.
- Prepared technical reports.

Bind Therapeutics, Cambridge, MA
Formulations Co-op, July 2011 – December 2011

- Developed nanoemulsion formulations for multiple drugs achieving slow release *in vivo* and increased efficacy.
- Performed *in vitro* drug release studies
- Lead project quantifying the PEG coverage of the nanoparticles using NMR and ELISA techniques.
- Prepared technical reports and presentations.

PUBLICATIONS

B.S. Wong, **D.J. Shea**, R. Law, J. Bieber, X. Che, L. Zheng, K. Konstantopoulos "Podocalyxin Promotes Migration of Pancreatic Cancer Cells by Altering Cytoskeletal and Adhesion Dynamics" (*in preparation*)

D.J. Shea, K. Konstantopoulos, A. Kontrogianni-Konstantopoulos "Loss of Giant Obscurins Enhance Migration and Cell Dynamics in Pancreatic Ductal Epithelial Cells." **(***in preparation***)**

D.J. Shea, Y.W. Li, K. Konstantopoulos, "E-selectin mediated rolling increases pancreatic tumor cell adhesion to Hyaluronic Acid." **(***in preparation***)**

A. Jablonska, **D.J. Shea**, S. Cao, J.W.M. Bulte, M. Janowski, MD, K. Konstantopoulos, P. Walczak,"Overexpression of VLA-4 in glial-restricted precursors enhances their endothelial docking and induces diapedesis in a mouse stroke model." (*accepted JCBFM*)

C.D. Paul, **D.J. Shea**, M. R. Mahoney, A. Chai, V. Laney, W.C. Hung, K. Konstantopoulos, "Interplay of the physical microenvironment, contact guidance, and intracellular signaling in cell decision making." *The FASEB Journal* **2016**

D.J. Shea, D. Wirtz, K.J. Stebe, K. Konstantopoulos, "Distinct kinetic and mechanical properties govern mucin 16-and podocalyxin-mediated tumor cell adhesion to E-and L-selectin in shear flow." *Oncotarget* **2015**

L.S.-L Cheung‡, **D.J. Shea‡**, N. Nicholes, A. Date, M. Ostermeier, K. Konstantopoulos. "Characterization of Monobody Scaffold Interactions with Ligand via Force Spectroscopy and Steered Molecular Dynamics." *Scientific Reports* **2015 (‡ equal contribution)**

SELECTED PRESENTATIONS

D.J. Shea, K. Konstantopoulos, A. Kontrogianni-Konstantopoulos “Loss of Giant Obscurins Enhance Migration and Cell Dynamics in Pancreatic Ductal Epithelial Cells.” AICHE, San Francisco, CA 2016

D.J. Shea, K. Konstantopoulos, A. Kontrogianni-Konstantopoulos “Loss of Giant Obscurins Enhance Migration and Cell Dynamics in Pancreatic Ductal Epithelial Cells.” BMES, Minneapolis, MN 2016

D.J. Shea, Y.W. Li, K. Konstantopoulos, “E-selectin mediated rolling increases pancreatic tumor cell adhesion to Hyaluronic Acid.” BMES, Minneapolis, MN 2016

D.J. Shea, D. Wirtz, K.J. Stebe, K. Konstantopoulos, “Distinct kinetic and mechanical properties govern mucin 16-and podocalyxin-mediated tumor cell adhesion to E-and L-selectin in shear flow.” BMES, San Antonio, TX 2014

D.J. Shea, C. Lee-Parsons, “Increased alkaloid production from cell cultures of the California poppy through elicitation and in situ product extraction,” ISPE national conference, San Francisco, CA 2012

HONORS AND AWARDS

ChemBE graduate research award, Johns Hopkins University	2015
Centennial Scholar, Johns Hopkins University	2013
Graduated summa cum laude, Northeastern University	2012
Sears B. Condit Award, Northeastern University	2012
Undergraduate Research Award, Northeastern University	2012
Undergraduate Research Grant, Northeastern University	2011
Dean’s Scholarship, Northeastern University	2007-2012
Dean’s List, Northeastern University,	2007-2012

ACTIVITIES AND VOLUNTEERING

ChemBE graduate student liaison committee Co-chair, Johns Hopkins University	2014-2016
Organized ChemBE professional development day, Johns Hopkins University	2014-2015
STEM mentoring and outreach program, ChemBE, Johns Hopkins University	2012-2016